



5-2023

## Space-Angle Discontinuous Galerkin Finite Element Method for Radiative Transfer Equation

Hang Wang

*University of Tennessee, Knoxville*, [hwang94@vols.utk.edu](mailto:hwang94@vols.utk.edu)

Follow this and additional works at: [https://trace.tennessee.edu/utk\\_graddiss](https://trace.tennessee.edu/utk_graddiss)



Part of the [Applied Mechanics Commons](#), and the [Numerical Analysis and Computation Commons](#)

---

### Recommended Citation

Wang, Hang, "Space-Angle Discontinuous Galerkin Finite Element Method for Radiative Transfer Equation." PhD diss., University of Tennessee, 2023.  
[https://trace.tennessee.edu/utk\\_graddiss/8096](https://trace.tennessee.edu/utk_graddiss/8096)

This Dissertation is brought to you for free and open access by the Graduate School at TRACE: Tennessee Research and Creative Exchange. It has been accepted for inclusion in Doctoral Dissertations by an authorized administrator of TRACE: Tennessee Research and Creative Exchange. For more information, please contact [trace@utk.edu](mailto:trace@utk.edu).

To the Graduate Council:

I am submitting herewith a dissertation written by Hang Wang entitled "Space-Angle Discontinuous Galerkin Finite Element Method for Radiative Transfer Equation." I have examined the final electronic copy of this dissertation for form and content and recommend that it be accepted in partial fulfillment of the requirements for the degree of Doctor of Philosophy, with a major in Mechanical Engineering.

Reza Abedi, Major Professor

We have read this dissertation and recommend its acceptance:

Trevor Moeller, Devina Sanjaya, Vasilios Alexiades

Accepted for the Council:

Dixie L. Thompson

Vice Provost and Dean of the Graduate School

(Original signatures are on file with official student records.)

# Space-Angle Discontinuous Galerkin Finite Element Method for Radiative Transfer Equation

A Dissertation Presented for the  
Doctor of Philosophy  
Degree  
The University of Tennessee, Knoxville

Hang Wang

May 2023

© by Hang Wang, 2023  
All Rights Reserved.

*To my mom, whose “Lao Pi Er” loves you forever.*

# Acknowledgements

First and foremost, I would like to acknowledge my advisor, Dr. Reza Abedi for his invaluable advice, support, and tutelage. It's amazing how hard he works and how much he cares about his students. Dr. Abedi supported me through numerous career and personal changes with love and patience. His encouragement to continue working and complete my degree was the primary reason I was able to finish my degree, especially during the rock bottom in my life. Dr. Abedi devotes his entire life to his students and studies, and I will be eternally thankful for the time he spent assisting me. I regard him as both a professional and a close friend.

I want to acknowledge my committee members: Dr. Trevor Moeller (UT Space Institute), Dr. Devina Sanjaya (UT Knoxville), and Dr. Vasilios Alexiades (UT Knoxville). Without the time, advice, and dedication of each member during my study efforts, I could not have achieved this goal.

Next, I was lucky to work with a great research group under Dr. Abedi and want to acknowledge both current and former members who I collaborated with: Dr. Philip Clarke, Dr. Justin Garrard, and Bahador Bahmani, Huynh Dong Giang, Erdem Caliskan, Ali Heidari, Md Ershadul Haque, Alexander Horton, Ryan Connor. Each one assisted with writing and debugging code, data analysis, and whatever other support I required for my research.

I want to thank my parents and sister for their support throughout this research. I also want to thank my mother, who has been taking perpetual rest since the COVID-19 pandemic, and tell her, “Ma, Ni De Lao Pi Er Bi Ye Le!”

Finally, I would be remiss if I did not acknowledge my wife Ling, and son, Yitang. I love you so much - without your sacrifices, I would not have finished. You two are my entire world and daily source of inspiration. Thank you for everything you do for me.

# Abstract

Radiative transfer theory describes the interaction of radiation with scattering and absorbing media. It has applications in neutron transport, atmospheric physics, heat transfer, molecular imaging, and others. In steady state, the radiative transfer equation is an integro-differential equation of five independent variables, which are 3 dimensions in space and 2 dimensions in the angular direction. This high dimensionality and the presence of the integral term present serious challenges when solving the equation numerically. Over the past 50 years, several techniques for solving the radiative transfer equation (RTE) have been introduced. These include, but are certainly not limited to, Monte Carlo methods, discrete-ordinate methods, spherical harmonics methods, spectral methods, finite difference methods, and finite element methods. Methods involving discrete ordinates and spherical harmonics have received particular attention in the literature.

This work introduces a parallel space-angle discontinuous Galerkin (saDG) method to solve the steady-state RTEs. The objective-oriented design of the software allowed us to apply the saDG approach to a variety of RTEs with considerable ease, including 1x1s, 1x2s, and 2x2s. The direct solver can achieve high-order accuracy solutions for low-dimensional problems. However, for high-dimensional problems, the direct solver is time-consuming and requires significant memory usage that may exceed the computer's RAM capacity. To address this issue, we employed the Angular Decomposition (AD) method in the iterative solver, which improves runtime efficiency and reduces memory usage. To handle large-scale problems, we developed a parallel

solver based on AD and Domain Decomposition (DD) methods. Finally, we applied Reflective Boundary Conditions to 2-D Cartesian radiative transfer problems.

# Table of Contents

<b>1</b>	<b>Introduction</b>	<b>1</b>
1.1	Radiative transfer equation . . . . .	2
1.2	Motivations . . . . .	3
1.2.1	Different forms of the RTE . . . . .	4
1.2.2	Efficiency & scalability . . . . .	5
1.2.3	Problems of interests of RTE . . . . .	7
1.3	Dissertation Format . . . . .	8
<b>2</b>	<b>Space-Angle Discontinuous Galerkin Method for Plane-Parallel Radiative Transfer Equation</b>	<b>9</b>
2.1	Abstract . . . . .	10
2.2	Introduction . . . . .	10
2.3	Mathematical Description . . . . .	13
2.3.1	RTE equation and boundary conditions . . . . .	13
2.3.2	Discontinuous Galerkin formulation . . . . .	14
2.4	Numerical Examples . . . . .	16
2.4.1	Method of Manufactured Solutions (MMS) . . . . .	16
2.4.2	Benchmark problems . . . . .	20
2.4.3	Point source . . . . .	23
2.4.4	Properties of the space-angle DG formulation . . . . .	25
2.5	Discussion and conclusions . . . . .	28

<b>3</b>	<b>Space-Angle Discontinuous Galerkin Method for Radiative Transfer between Concentric Cylinders</b>	<b>31</b>
3.1	Abstract . . . . .	32
3.2	Introduction . . . . .	32
3.3	Mathematical description . . . . .	36
3.3.1	Radiation transfer equation and boundary conditions . . . . .	36
3.3.2	Characteristic directions for the RTE . . . . .	38
3.3.3	Discontinuous Galerkin formulation . . . . .	39
3.4	Implementation . . . . .	44
3.4.1	Discontinuous Galerkin implementation . . . . .	44
3.4.2	Method of characteristic . . . . .	45
3.5	Numerical examples . . . . .	48
3.5.1	Method of manufactured solution . . . . .	48
3.5.2	Verification of the DG method with the method of characteristics	51
3.5.3	Benchmark problems between two concentric cylinders . . . . .	52
3.6	Discussion and conclusions . . . . .	55
<b>4</b>	<b>Iterative Space-Angle Discontinuous Galerkin Method for Radiative Transfer Equation</b>	<b>58</b>
4.1	Abstract . . . . .	59
4.2	Introduction . . . . .	59
4.3	Discontinuous Galerkin formulation of RTE . . . . .	62
4.4	iterative methods and angular decomposition . . . . .	65
4.4.1	Angular decomposition . . . . .	65
4.4.2	iterative methods . . . . .	67
4.5	Numerical examples . . . . .	69
4.5.1	Convergence study . . . . .	70
4.5.2	Numerical investigation of the stability of the iterative methods	70
4.5.3	Acceleration of iterative methods . . . . .	72

4.5.4	Internal Gaussian source in small scattering albedo media . . .	74
4.6	Discussion and conclusions . . . . .	75
<b>5</b>	<b>Combined Angular and Domain Decomposition Parallel Methods to Solve 2D Radiative Transfer Problems Using Space-Angle Discontinuous Galerkin Method</b>	<b>77</b>
5.1	Abstract . . . . .	78
5.2	Introduction . . . . .	78
5.3	Formulation . . . . .	81
5.3.1	Space-angle discontinuous Galerkin method . . . . .	82
5.4	Implementation . . . . .	85
5.4.1	Angular Decomposition . . . . .	85
5.4.2	Domain decomposition . . . . .	88
5.5	Numerical examples . . . . .	89
5.5.1	Validation . . . . .	90
5.5.2	Scaling performance . . . . .	91
5.5.3	Square geometry with obstacles . . . . .	95
5.6	Conclusion . . . . .	96
<b>6</b>	<b>Space-Angle Discontinuous Galerkin method for 2D Radiative Transfer Equation with Diffusively and Specularly Reflective Boundary Conditions</b>	<b>99</b>
6.1	Abstract . . . . .	100
6.2	Introduction . . . . .	100
6.3	Formulation . . . . .	103
6.3.1	2D RTE & its boundary conditions . . . . .	103
6.3.2	Space-angle DG discretization . . . . .	105
6.4	Implementation . . . . .	107
6.4.1	Decoupling of scattering integral terms . . . . .	108
6.4.2	Reflective boundary conditions . . . . .	109

6.4.3	Summary of parallel process . . . . .	110
6.5	Numerical examples . . . . .	111
6.5.1	Square box . . . . .	111
6.5.2	Parabolic reflector . . . . .	116
6.6	Conclusions . . . . .	117
<b>7</b>	<b>Summary and Conclusions</b>	<b>119</b>
	<b>Bibliography</b>	<b>122</b>
	<b>Appendix</b>	<b>141</b>
	<b>Vita</b>	<b>187</b>

# List of Tables

1	Hemispherical reflectivity and transmissivity of a slab with unit thickness, transparent boundaries, and isotropic incidence. . . . .	142
2	Hemispherical reflectivity and transmissivity of a slab with unit thickness, transparent boundaries, and isotropic incidence. . . . .	142
3	Number of iteration for the GS method and different relaxation factors for the SOR method under different mesh resolutions. The optimum values are shown in boldface. . . . .	142
4	Weak scaling performance for AD. . . . .	143
5	Strong scaling performance for AD. . . . .	143
6	Weak scaling performance for DD. The matrix solving time is denoted by $t_p^K$ . . . . .	143
7	Strong scaling performance for DD. . . . .	143
8	Performance test for hybrid AD-DD. . . . .	144
9	The number of iterations for the specular reflection problems. . . . .	144
10	The number of iterations (second row) and convergence rate (third row) for the point source problem for $\kappa = 1$ . . . . .	144

# List of Figures

1	The applications of radiation transfer equation [42]. . . . .	145
2	This figure shows the variables needed in different versions of RTE in the three coordinate systems, respectively. . . . .	145
3	A schematic of a space-angle domain. The horizontal axis $x$ and the vertical axis $\hat{s}$ represent the space and angle, respectively. The sample element $\mathcal{Q}$ is coupled with the elements in red, yellow, and blue, due to the integral operator. The element boundary in cyan is coupled with the element boundary in blue, since the incidence angle and the reflection angle are located on these element boundaries, respectively. The dark green line separates the domain into two. . . . .	146
4	Two domain decomposition methods. (a) The spatial domain is partitioned into two non-overlapping subdomains in orange and green. (b) The spatial domain is divided into two subdomains. Each subdomain contains extra elements on the subdomain interface, which are duplicated from its neighbor subdomain. . . . .	146
5	Specular, diffuse, and directional diffuse reflection from a surface. . .	147
6	Refraction in the media of constant and variable refractive indices. . .	147
7	Format of the dissertation. . . . .	148
8	Demonstration of region of applicability of residuals in $(z, \mu)$ domain. .	148
9	The use of wave inflow values for $I^*$ . . . . .	149

10	The formation of space-angle basis functions by tensor product of space and angle monomial basis functions. . . . .	149
11	SDG Mesh for code verification . . . . .	150
12	Visualization of solution for code verification case of zero phase . . .	150
13	Visualization of solution for code verification case of non-zero phase function . . . . .	151
14	Convergence study of the DG RTE solution for a problem with exact harmonic solution. Convergence rate of $p + 1$ is achieved for the space-angle order of $p = 0$ to 3. . . . .	151
15	Finite element mesh for the DG method in the spatial-angular domain.	152
16	Contour plot of radiative intensity, $I(z, \mu)$ , in space-angle domain. . .	153
17	Radiative intensity distribution at outflow boundaries. . . . .	153
18	Radiation heat flux distribution. . . . .	154
19	Contour plot of radiative intensity, $I(z, \mu)$ , in space-angle domain. . .	154
20	Radiative intensity distribution at outflow boundaries. . . . .	155
21	Radiation heat flux distribution. . . . .	155
22	The effect of type of application of point source, element size $h$ , and order $p$ on discrete DG solution. In all cases, except f) a zero phase function is used. . . . .	156
22	(continued) The effect of type of application of point source, element size $h$ , and order $p$ on discrete DG solution. In all cases, except f) a zero phase function is used. . . . .	157
23	Contour plot of radiative intensity for the problem with the line source term. The zoomed view shows the line source by a thick white line and its neighboring elements, where $M_z$ are the spatial upstream elements of the line source and $M_\mu^+$ and $M_\mu^-$ are the upward and downward angular neighboring elements. . . . .	158
24	Convergence study for the problem in §2.4.1, but with changing only $p_z$ and fixing $p_\mu = 0$ . . . . .	159

25	Cylindrical coordinates for the one-dimensional RTE. . . . .	159
26	Coordinate along a characteristic line. . . . .	159
27	The illustration of the extrusion of the spatial domain in angle directions $\mu$ and $\tilde{\varphi}$ . The left figure shows the one-dimensional spatial elements and the right shows their extrusion to form the three-dimensional domain $\Omega$ . . . . .	160
28	The illustration of normal vectors of the element $\mathcal{Q}$ and its neighboring elements on the shared boundaries in $r$ - $\tilde{\varphi}$ plane. The subscript and superscript of normal vectors correspond to the element with normal vector and its direction, respectively. . . . .	160
29	Schematic of the discrete set of $r - \tilde{\varphi}$ planes, characteristic lines, and points for numerical solution of the method of characteristics. . . . .	161
30	Validation of the DG RTE method by the MMS for second order polynomial in space and angle for $I^M$ . The contour plots in $r - \tilde{\varphi}$ plane are sliced in $\mu$ direction at $\mu = -0.5, 0, 0.5$ . . . . .	161
31	Convergence study of the DG RTE solution for the harmonic manufactured solution. The asymptotic convergence rate $\beta_p = p+1$ is achieved as $h \rightarrow 0$ for $p = 0$ to $p = 3$ . . . . .	162
32	The results of the method of characteristic in a $r - \tilde{\varphi}$ plane, where $\tilde{\varphi} < 0$ shows the characteristics in black and $\tilde{\varphi} \geq 0$ shows the characteristics with the intensity field. The red arrows point to regions where characteristic lines are sparse. . . . .	162
33	Contour plots of radiation intensity for the problem in §3.5.2 for two different solution methods. . . . .	163
34	Convergence study of the DG RTE solution with respect to a high resolution reference solution obtained by the method of characteristics. . . . .	163

35 Nondimensional radiative heat transfer,  $\Psi$ , between concentric cylinders at radiative equilibrium against the optical thickness,  $\tau_2 - \tau_1$ , at different radius ratio,  $R_2/R_1$ . The solid lines are the numerical solution presented by Loyalka [86]; the hollow shapes (squares, circles and triangles) are the solutions by the DG method. . . . . 164

36 Contour plot of radiation intensity of the benchmark problem for  $R_1/R_2 = 0.5$  and  $\tau_2 - \tau_1 = 10$ . . . . . 164

37 Contour plots of radiation intensity for the problem in §3.5.3 for  $\mu = 0$  for two different methods. The left and right figures correspond to the solutions by the DG method and the method of characteristics (MoC), respectively. . . . . 165

38 The illustration of the extrusion of the spatial domain in angle directions  $\mu$  and  $\tilde{\varphi}$ : a) the one-dimensional spatial elements, b) extrusion of the spatial mesh to form the three-dimensional domain  $\Omega$ . . . . . 165

39 Illustrations of normal vectors of the element  $\mathcal{Q}$  and its neighboring elements on the shared boundaries in  $r$ - $\tilde{\varphi}$  plane. The blue and lines represent the element boundary in the  $r$  and  $\tilde{\varphi}$  directions, respectively. 166

40 The stiffness matrix pattern in a  $4 \times 4 \times 4$  domain: (a) the  $4 \times 4 \times 4$  space-angle mesh; (b) the stiffness matrix pattern of all couplings. The dots represent the matrix block per element. The gray square  $\mathcal{C}_{13,\tilde{\varphi}}$  depicts the coupling in  $\mu$  direction between elements  $\mathcal{C}_{1,\tilde{\varphi}}$  and  $\mathcal{C}_{3,\tilde{\varphi}}$ . The dots in the four larger squares represent in-slab couplings. . . . . 166

41 Contour plots of the common ratios of the SOR scheme changing with the eigenvalues,  $\lambda$ , and the relaxation factors. The common ratio greater than 1 is not considered (white area). The white curve highlights the optimal relaxation factors for the corresponding eigenvalues. . . . . 167

42	Convergence study of the DG RTE solution for the harmonic manufactured solution. The asymptotic convergence rate $\beta_p = p + 1$ is achieved as $h \rightarrow 0$ for $p = 0$ to $p = 3$ . . . . .	167
43	The maximum and minimum of $\lambda$ against (a) the scattering coefficients $\sigma_s$ of different mesh resolutions (b) $R_1/R_2$ for the problem described in §4.5. . . . .	168
44	The optimal $\alpha$ (black) and common ratio $q$ (red) against (a) the scattering coefficients $\sigma_s$ of different mesh resolutions and (b) the ratio of $R_1$ and $R_2$ . . . . .	168
45	Evolution of the error $e^n(\mathbf{J})$ along iterations. Circle and square markers correspond to the results by the coarse and fine meshes, respectively. . . . .	169
46	Efficiency between direct solver and AD iterative solver. . . . .	169
47	(a)The refined angular mesh. (b)The number of iterations for different scattering coefficients. (c) The contour plot of the intensity in the $r - \tilde{\varphi}$ plane, where $\mu = 0$ . . . . .	170
48	Space-angle mesh generated by element extrusion from spatial mesh. . . . .	170
49	An example of jump condition for $I^*$ in the direction of $\hat{\mathbf{s}}$ . . . . .	171
50	An example of angular decomposition for the scattering term. 16 angular elements are divided evenly into four subdomains. . . . .	171
51	The spatial domain is divided into two subdomains. Each subdomain contains extra elements on the subdomain interface, which are duplicated from its neighbor subdomain. . . . .	171
52	Trapezoidal enclosure with boundary conditions and spatial mesh. . . . .	172
53	Non-dimensional radiative heat flux for $\kappa = 0.1 \text{ m}^{-1}$ , $\kappa = 1.0 \text{ m}^{-1}$ , and $\kappa = 10 \text{ m}^{-1}$ alone the bottom and top walls. . . . .	172
54	Quadrilateral enclosure with boundary conditions. . . . .	173
55	Contour temperature plot for a quadrilateral enclosure. . . . .	173

56	Strong scaling performance for (a) total run time for AD, (b) average iteration time for AD, and (c) total run time for DD. . . . .	174
57	A schematic for the square geometry with obstacles (a) Circular, (b) Square. . . . .	175
58	A schematic for the contour temperature field with obstacles (a) Circular, (b) Square. . . . .	175
59	A schematic for the contour temperature field with obstacles (a) Circular, (b) Square. . . . .	176
60	Specular, uniform diffuse, and directional diffuse reflection from a surface.	176
61	Radiative intensity diffusely and specularly reflected from a surface boundary. . . . .	176
62	Space-angle mesh generated by 2D element extrusion from spatial mesh.	177
63	An example of angular decomposition for the scattering integral term. (a) Spatial mesh. The sample element $\mathcal{Q}$ contains 6 quad points in space. (b) Angular domain at spatial point $\mathcal{Q}_3$ . 16 angular elements are divided evenly into four slabs. Slab 1 and its quadrature points (solid dots) are in red; the other slabs and quadrature points (hollow dots) are in blue. . . . .	177
64	Illustrations of the implementation of the reflective BCs. (a) For a given spatial quadrature point $\partial\mathcal{Q}_2$ on the boundary of element $\mathcal{Q}$ , the spatial normal $\mathbf{n}$ is known and determines the slant line that divides the angular domain into incidence angles and reflected angles in (b) and (c) that correspond to the angular domain of point $\partial\mathcal{Q}_2$ . The red solid dots are the quadrature points in slab 1. (b) The blue hollow dots are the decoupled quadrature points. (c) The blue hollow dots are the quadrature points in the reflected angle. The red dash-dot circle (pointed to with an arrow) is the specular incident angle corresponding to the specularly reflected angle solid red point, pointed to by the other arrow. . . . .	178

65	Six cases with different reflection boundary conditions. Boundaries in red represent the reflective boundaries. . . . .	179
66	Schematic for the problem with a prescribed incident on the left wall. The other three walls are either specularly reflective or vacuum depending on the case described in Fig. 65. . . . .	179
67	Spatial mesh for the specular reflection problem. . . . .	180
68	Contour plots of radiative density $D$ for the specular reflection problem with incidence on the left boundary for the cases (1), (2), (3), and (5) listed in Fig. 65 in rows. The columns from left to right correspond to albedo $\omega_s = 0$ (zero scattering), and $\omega_s = 0, 5, 1$ , respectively. . . . .	181
69	Evolution of errors with respect to iterations for $\omega_s = 1$ . . . . .	182
70	Convergence rate with respect to number of specularly reflective boundaries when $\omega_s = 0, 0.25, 0.5$ , and $1$ . . . . .	182
71	Contour plots of radiative density $D$ for the uniformly diffuse reflection problem with incidence on the left boundary, the diffusely reflective boundary at the bottom, and vacuum boundaries on the right and top (case (2) in Fig. 65). . . . .	183
72	Contour plots of radiative density $D$ for the directional diffuse reflection problem with incidence BC on the left, diffuse reflective BC on the bottom, and vacuum on the right and top boundaries (case (2) in Fig. 65). The solutions correspond to different values of $a_b$ . . . . .	183
73	Spatial mesh for the point source problem. . . . .	184
74	Contour plots of radiative density $D$ for the point source problem in the first and third rows. The second and fourth rows are the subtractions of the solutions from the free box solution. The top colorbar at the second row and first column is for the solutions; and the bottom colorbar is for the subtractions. . . . .	185
75	Spatial mesh for the parabolic reflector problem. . . . .	186
76	Contour plots of Radiative density $D$ for the parabolic reflector problem. . . . .	186

# Chapter 1

## Introduction

This thesis is devoted to the development of an efficient algorithm to solve radiative transfer problems in multi-dimensions. A significant barrier for current computers, aside from the requirement to reduce computing time, is the amount of memory required to hold operators and data. We, therefore, examine the entire procedure, from discretization to solution algorithms to implementation strategies, in order to offer a way to solve physics problems with reasonable time and storage. Our main direction of improvement is the implementation on clusters and supercomputers.

## 1.1 Radiative transfer equation

The radiative transfer takes place in a wide range of natural phenomena and engineering applications. The propagation of radiation in the form of electromagnetic waves through a medium is affected by absorption, emission, and scattering processes. The radiative transfer equation (RTE) mathematically describes these interactions, which have a wide range of applications in such areas as heat transfer, neutron transport, atmospheric science, optical molecular imaging, and some other applications, as shown in Fig. 1 [42]. In brief, modeling radiative transfer is essential in many engineering fields. The equation used in most radiative transfer models is the radiative transfer equation, which describes a beam radiation that loses energy to absorption, gains energy via emission, and redistributes energy by scattering. In the quasi-steady state we investigated, the RTE can be viewed as an integro-differential equation of five independent variables, given by [109, 60, 32, 42]

$$\hat{\mathbf{s}} \cdot \nabla I + \beta I = \kappa I_b + \frac{\sigma_s}{4\pi} \oint_{4\pi} I(\mathbf{x}, \hat{\mathbf{s}}') \Phi(\hat{\mathbf{s}}, \hat{\mathbf{s}}') d\Omega. \quad (1.1)$$

The solution of the radiative intensity  $I$  is dependent on the direction  $\hat{\mathbf{s}}$  and the spatial position  $\mathbf{x}$ . Other parameters are described in the following chapters.

## 1.2 Motivations

The main difficulties in solving the RTE numerically are high-dimensionality and discontinuity solutions in both space and angle. The former requires a huge amount of memory and computation time even at a reasonable accuracy. Aside from reducing the dimension of a problem, adaptive and parallel methods are the common ways to overcome this issue. Therefore, the discontinuous Galerkin (DG) method is adopted for the following advantages:

1. The DG method allows discontinuous solutions of RTE in angle and space for their discontinuous base functions.
2. Due to the judicious use of the target fluxes, which are determined by the values on the two sides of the element interface, the “wave motion” which is the propagation of incident radiation in the RTE can be captured.
3. The DG method has its natural advantage in parallel computing, because of the weak couplings of elements. It is necessary to make our program parallel, since we are going to solve the RTE potentially in a 5-dimensional domain.
4. The element size and polynomial order can be changed arbitrarily due to the weak enforcement of jump conditions.

Opposed to the common idea of discretizing the derivative operator on the spatial domain and the integral operator in the angular domain, independently, we show a possibility to combine these into one Galerkin approximation on a space-angle domain. Clearly, the space-angle DG (saDG) method includes the opportunity of using efficient parallelization techniques and obtaining highly accurate solutions. Furthermore, the saDG software has an object-oriented design based on the software for the solutions of *causal Spacetime Discontinuous Galerkin* (cSDG) methods for elastodynamics [5], advection-diffusion equation [93], and electromagnetics [7], just to name a few. It allows for the creation of reusable classes, which can be easily instantiated to create

objects that can be used multiple times in different parts of a finite element simulation. The object-oriented design can reduce the amount of code that needs to be written and make it easier to maintain and update the software, which is suitable for handling different forms of RTEs.

### 1.2.1 Different forms of the RTE

As mentioned above, the dimension of the general RTE can be reduced to different versions, for example, for a symmetric problem or a two-dimensional Cartesian problem that has different dependencies, as shown in Fig. 2. One can easily implement any version of the RTE thanks to the object-oriented design by providing the forms of the derivative operator and the integral operator. So far, the versions of one-dimension Cartesian (1x1s), two-dimension Cartesian (2x2s), three-dimension Cartesian (3x2s), one-dimension cylindrical (1x2s), and two-dimension cylindrical (2x1s) RTEs have been implemented.

Our publications related to this topic are listed below:

1. Clarke, P., Wang, H., Garrard, J., Abedi, R., and Mudaliar, S. (2019a). Space-angle discontinuous Galerkin method for plane-parallel radiative transfer equation. *Journal of Quantitative Spectroscopy and Radiative Transfer*, 233:87–98
2. Wang, H., Abedi, R., and Mudaliar, S. (2020c). Space-angle discontinuous Galerkin method for radiative transfer between concentric cylinders. *Journal of Quantitative Spectroscopy and Radiative Transfer*, 257:107281
3. Wang, H., Abedi, R., and Mudaliar, S. (2019). A discontinuous Galerkin method for the solution of two dimensional axisymmetric radiative transfer problem. In *2019 USNC-URSI Radio Science Meeting (Joint with AP-S Symposium)*, Atlanta, Georgia, USA. In press

4. Wang, H., Abedi, R., and Mudaliar, S. (January 6-9, 2020b). Space-angle discontinuous Galerkin method for one-dimensional cylindrical radiative transfer equation. In *AIAA Science and Technology Forum and Exposition 2020*, Orlando, Florida, USA. In press
5. Wang, H., Abedi, R., and Mudaliar, S. (2021a). Iterative space-angle discontinuous galerkin method for radiative transfer problems from 1d to 3d. In *2021 XXXIVth General Assembly and Scientific Symposium of the International Union of Radio Science (URSI GASS)*, pages 1–4

### 1.2.2 Efficiency & scalability

Due to the high dimension of the computational domain, the linear algebraic system assembled by the saDG method easily leads to an untreatable size, even for a one-dimensional cylindrical problem (three-dimensional in space and angle) [119]. Therefore, it is not feasible to directly solve the discrete system of linear equations. We, hence, applied the decomposition methods in angle and space to the computational domain. After such decomposition, a solution to the global system is sought while performing local processes in each subdomain and communications between subdomains. These methods are applied to parallel computing for the solution of the RTE, which significantly improves the efficiency, performance, and scalability to solve radiative transfer problems on supercomputers.

#### Angular decomposition & iterative method

For the angular decomposition (AD) method, the challenges are decouplings of the integral operator in (1.1) and reflective boundary conditions. For example, in the space-angle domain,  $\mathbf{x} \times \hat{\mathbf{s}}$ , as shown in Fig. 3, element  $\mathcal{Q}$  in gray couples with the other three elements in the second column (in angle) if the integral term is applied. This is because the interval of the integral operator is form  $[\hat{\mathbf{s}}_0, \hat{\mathbf{s}}_4]$ . If reflective boundary conditions are applied, assuming the element boundary at  $\mathbf{x}_4$  in cyan contains the

reflected angle, it is then coupled with the incident angle which is located in the element in green. To decouple these terms, we slice the angular domain at  $\hat{\mathbf{s}}_1$ ,  $\hat{\mathbf{s}}_2$ , and  $\hat{\mathbf{s}}_3$  to achieve 4 slabs. Then, the computation is taken individually in each slab. When it comes to the integral operator or the boundary conditions, the communications between each slab are taken by exchanging the solutions. Such processes require mesh renumbering and an iterative method, such as the successive over-relaxation method that can accelerate the convergence with a proper relaxation factor. Although iteration is inevitable for decouplings, memory requirements and total computation time for the AD method are much less than for the direct solver.

### Domain decomposition

For the domain decomposition (DD) method, the spatial mesh is divided into smaller subdomains. As shown in Fig. 3, the dark green line split the domain into two subdomains. One option is to solve each subdomain with the same governing equation individually by the assigned processor, which is known as the conventional DD method, as shown in Fig. 4a. Subdomains are not isolated, since the continuity on the subdomain interfaces is weakly enforced. Therefore, communications to pass the interface solutions are needed. Similar to the AD method, to achieve the global solutions, iteration is required, since the local solutions inside subdomains depend on the previous iteration from the neighbor subdomains. Another option is to obtain the global linear system of equations directly by assembling the local stiffness matrices in the subdomains in a distributed manner and solving the whole with a distributed-memory linear solver, such as MUMPS [8]. In this case, calculation of the jump conditions is required on the subdomain interface from the neighbor elements in other subdomains. To reduce the amount of communication, additional elements belonging to the respective adjacent processor are added to the border of each subdomain. These elements are referred to as ghost elements. As depicted in Fig. 51, the ghost elements in green in subdomain 1 are duplicated from subdomain 2. Because of the creation of ghost elements, each processor is required to take more memory than

the conventional DD method. However, it is worth solving the global linear system directly rather than iteratively by sacrificing some memory usage.

Our publications related to this topic are listed below:

1. Wang, H., Abedi, R., and Mudaliar, S. (forthcoming). Iterative space-angle discontinuous Galerkin method for radiative transfer equation. *Waves in Random and Complex Media*
2. Wang, H., Abedi, R., and Mudaliar, S. (2020a). A parallel space-angle discontinuous galerkin method for radiative transfer in two-dimensional rectangular enclosures. In *2020 IEEE USNC-CNC-URSI North American Radio Science Meeting (Joint with AP-S Symposium)*, pages 1–2
3. Wang, H., Abedi, R., and Mudaliar, S. (2021b). A space-angle discontinuous galerkin method for one-dimensional cylindrical radiative transfer equation with angular decomposition. In *2021 United States National Committee of URSI National Radio Science Meeting (USNC-URSI NRSM)*, pages 107–108

### 1.2.3 Problems of interests of RTE

#### Reflections

In real-world physics, surface reflections can be very complex with radiative transfer problems. The widely used assumptions for surfaces are diffuse reflectors of radiant energy. However, many surfaces deviate substantially from this behavior. All clean metals, many glassy materials, and most polished materials in industrial applications display strong specular reflection. It is important to import different reflective boundary conditions. We consider the model of reflections, such as specular, diffuse, and directional diffuse reflection, which allows us to better understand the radiative transfer phenomenon, as shown in Fig. 5. This work is supported by The Air Force Research Laboratory’s Sensors Directorate.

## Refraction

Another important phenomenon in radiative transfer problems is refraction. This includes the assumptions of piece-wise constant and variable refractive indices, as shown in Fig. 6. The refractive index can be a function of spatial location. At a given location, it also varies if there is a change in the density. These changes may be due to the structure of the system under consideration or due to the heating effect caused by the spatial and temporal variations in the medium. Modern electronic and electrical components like thermal barrier coatings, connectors, electrochromic displays, sensors, *etc.* are some of the examples that require consideration of variable refractive indices. Our goal is to simulate refraction problems with both the piece-wise constant and variable refractive indices in year 2023.

Our publications related to these topics are listed below:

1. Wang, H., Abedi, R., and Mudaliar, S. (2022). A space-angle discontinuous galerkin method for two-dimensional radiative transfer equation with reflective boundary conditions. In *2022 United States National Committee of URSI National Radio Science Meeting (USNC-URSI NRSM)*, pages 326–327

## 1.3 Dissertation Format

The following chapters contain several journal articles in which the dissertation author was either the primary author or a major contributor. Figure 7 shows the contents of the following chapters.

## Chapter 2

Space-Angle Discontinuous

Galerkin Method for Plane-Parallel

Radiative Transfer Equation

## 2.1 Abstract

The radiative transfer equation (RTE) for a plane-parallel problem involving scattering, absorption and radiation is solved using the discontinuous Galerkin (DG) finite element method (FEM). Both space and angle directions are discretized by the DG method. Thus, while the method has a higher accuracy in angle direction than hybrid FEM-Discrete Ordinate ( $S_N$ ) and FEM-Spherical Harmonic ( $P_N$ ) methods, it removes the continuity constraint implied by the form of basis function for continuous FEMs in space and angle. The discrete formulation of the problem is presented for nonzero phase function and a variety of boundary conditions. The numerical results demonstrate a  $p + 1$  convergence rate when the intensity is interpolated by an order  $p$  polynomial in both space and angle. The method is validated against exact solutions, and compared with other space-angle and hybrid FEMs for a few benchmark problems. The appropriateness of the DG formulation for problems with discontinuous solution is demonstrated by solving a problem with delta source term, where an in-element averaging of the source term eliminates negative intensity values for high order elements. Finally, a problem with an angular-line source term and a convergence study where the solution order is zero in angle are used to further demonstrate the advantages of the high order space-angle DG formulation; for the convergence study problem, the error was reduced by about 13 binary orders of magnitude, by increasing the order in both space and angle, rather than in space only.

## 2.2 Introduction

The radiative transfer equation (RTE) describes the interaction of radiation in an absorbing, scattering medium. These equations describe such wide-ranging processes as radiation transfer in the atmosphere, flow-field heat transfer for hypersonic vehicles, or x-ray imaging. Two of the most popular solution methods for these transfer

equations are the Discrete Ordinate ( $S_N$ ) method and Spherical Harmonic ( $P_N$ ) method. In the Discrete Ordinate method, the angular domain is discretized by a discrete set of ordinate directions, which creates a set of spatial RTE equations for each specific direction. The spatial domain is solved using finite difference, finite volume (FV), or finite element methods (FEMs). Integrals over the solid angles are replaced by sums over the ordinate directions. The spherical harmonic method involves multiplying the RTE by various powers of direction cosines of the intensity, which forms a set of moment equations which are solved to find the solution. The intensity is approximated by an orthogonal series of spherical harmonics, thereby giving the method its name [109].

One common method for solving the equation in the spatial domain, while utilizing the  $S_N$  or  $P_N$  method for the angular domain, is the Galerkin finite element method. Shmygevsikii [108], Krim [1], Razzaghi [98], and Sallah [105] implemented the Galerkin technique for the RTE. Egger *et al.* [44] used the Galerkin finite element method in space/spherical harmonic method in the angular domain to solve the RTE. Because the normal Galerkin method can show numerical oscillations for certain problems, Avila [11] instead used two stabilized Galerkin finite element methods: the streamline-upwind Petrov Galerkin (SUPG) method, and the Orthogonal Subcales (OSS) method, to resolve this issue while using the discrete ordinate method to discretize in angle. Both SUPG and OSS methods showed better accuracy than the Galerkin finite element method. To improve convergence rates of the solution, Grella implemented a sparse tensor Galerkin approach using both the ( $S_N$ ) [55] and ( $P_N$ ) [56] methods. To solve radiative transfer problems in the random space, Jin and Lu [67] developed a Stochastic Galerkin method.

The Galerkin finite element method does have a disadvantage in solving the radiative transfer equation for certain types of problems in that it cannot handle discontinuities in the solution. Because the RTE has wave propagation characteristics along all ray directions, this frequently leads to discontinuities. A particular way to resolve this issue is to soften the requirements of continuity from element to

element. The Discontinuous Galerkin (DG) method was developed to solve this type of problem. Liu *et al.* [84] developed an  $(S_N)$  Discontinuous Galerkin method for solving the RTE in semitransparent graded index medium. Zhao *et al.* [139], Han *et al.* [58] and Eichholz [45] developed an  $(S_N)$  Discontinuous Galerkin method for solving RTE problems. Crockatt *et al.* [33] developed a  $(S_N)$ -DG method for the RTE while implementing an integral deferred correction scheme in time for transient RTE problems. Yuan *et al.* [133] used a  $(S_N)$ -DG method while implementing a high order positivity preserving limiter that prevents negative intensities which can lead to an inaccurate solution. Similarly, Laboure *et al.* [75] developed a  $(P_N)$ -DG method for the RTE. Cui *et al.* [34, 35] used a hybrid DG method for multi-dimensional RTE, where the solution space is the product of a polynomial function in space and a delta function for the solid angle.

In spite of their popularity, the discrete ordinate method and spherical harmonic method are not the only methods used to solve the RTE in the angular domain. Liu [83] utilized the FEM in both space and angle to solve the one-dimensional RTE with variable spatial refractive index, which also been studied later by using the hybrid FV/ FE method [137]. The hybrid FV/ FE method for solving the RTE in multi-dimensional enclosure was developed by Coelho [30]. Gao and Zhao [50], [51] implemented a method using the DG in space and a piece-wise constant finite element method in angle. Olbrant *et al.* [91] implemented a DG spatial discretization, but used an entropy-based M1 model to solve in the angular domain. As in the spatial domain, continuous methods can fail when discontinuities occur in the angular space or domain interfaces. Therefore, over the past several years, Kophazi *et al.* [73] and Kitmann *et al.* [37] have both developed space-angle DG methods to solve both spaces for this issue. Kophazi implemented the method for a simplified equation without the phase function, known as the Boltzmann transport equation. Kitmann solved the RTE in spherical symmetry, which is a more complex version of the RTE because it includes an additional derivative with respect to the polar angle.

The Discontinuous Galerkin method has been shown to have advantages for solving the radiative transfer equation. As detailed above, an arbitrary number of discontinuities in the spatial and angular domains can be considered. When applying the discrete ordinate or spherical harmonic methods, the radiative transfer equation is solved as a set of coupled equations in space and angle. Because the DG method is discontinuous by its nature, it prevents the artificial coupling in angle that the continuous methods imply. These discontinuities also allow for an arbitrary order of accuracy for each element, which is a very important consideration for future adaptive implementations of this method.

This paper will detail an implementation of the space-angle DG method for a one-dimensional RTE equation. In the next section, the formulation of the DG method into a general RTE solver is detailed. Then, results from the code are validated and a convergence study performed. Next, to compare the performance of the solver against known exact solutions, benchmark problems are chosen as detailed in papers [96, 22]. Test cases selected to test the point source function implemented in the solver are detailed. Finally, to further show the properties of the DG method, especially in angle, a problem with an angular-line source term and a convergence study where the solution order in angle is kept zero are investigated.

## 2.3 Mathematical Description

### 2.3.1 RTE equation and boundary conditions

For the one dimensional scattering medium with spatial- and angular-dependent properties, the plane-parallel radiative transfer equation can be written as,

$$\mu \frac{dI}{dz} + \beta I - \frac{\sigma_s}{2} \int_{-1}^1 \Phi(z, \mu, \mu') I(z, \mu') d\mu' = S \quad (2.1)$$

where  $\mu$  is the direction cosine,  $I(z, \mu)$  is the radiant intensity,  $S$  is the source term, and  $\Phi(z, \mu, \mu')$  is the anisotropic scattering phase function. The values  $\beta = \kappa_\eta + \sigma_s$ ,

$\kappa_\eta$ , and  $\sigma_s$ , are space-dependent extinction, absorption, and scattering coefficients, respectively.

The partial differential equation (PDE) is enforced on the square domain  $(z, \mu) \in \Omega = (\underline{z}, \bar{z}) \times (-1, 1)$ , where  $\underline{z}$  and  $\bar{z}$  are the minimum and maximum values of the spatial coordinate  $z$ . The boundary conditions are specified on inflow boundaries for  $I$  which are comprised of  $\mu > 0$  and  $\mu < 0$  for  $z = \underline{z}$  and  $z = \bar{z}$ , respectively. The specific forms of boundary conditions used herein are discussed in §2.4.

### 2.3.2 Discontinuous Galerkin formulation

Fig. 8 shows an  $m$  by  $n$  tensor product discretization of  $\Omega$ , where  $(\underline{z}, \bar{z})$  and  $(-1, 1)$  are discretized into  $\{z_0, z_1, \dots, z_m\}$  and  $\{\mu_0, \mu_1, \dots, \mu_n\}$ , respectively, for  $z_0 = \underline{z}$ ,  $z_m = \bar{z}$ ,  $\mu_0 = -1$ , and  $\mu_n = 1$ . Due to the change of direction of waves at  $\mu = 0$ , 0 is included in the set  $\{\mu_0, \mu_1, \dots, \mu_n\}$ .

For an arbitrary element  $\mathcal{Q} \in \Omega$ , the residuals are,

$$\mathcal{R}_{\mathcal{Q}} = \mu \frac{dI}{dz} + \beta I - \frac{\sigma_s}{2} \int_{-1}^1 \Phi(\mu, \mu') I(z, \mu') d\mu' - S \quad (2.2a)$$

$$\mathcal{R}_{\partial\mathcal{Q}_z} = \mu(I^* - I) \quad (2.2b)$$

where (2.2a) corresponds to the residual in satisfying the PDE in equation (2.1). For discontinuous Galerkin methods, the continuity of the solution on boundaries of an element are weakly satisfied relative to target solutions. For this problem, since (2.1) does not involve any derivatives in  $\mu$ , no continuity condition is enforced on  $\partial\mathcal{Q}_\mu$ , the angle boundaries of the element as shown in the figure.

Equation (2.2b) corresponds to the residual in enforcing the target value for  $I$  on  $\partial\mathcal{Q}_z$ , the spatial boundaries of  $\mathcal{Q}$ . This condition and the factor  $\mu$  directly correspond to the jump part of the differential operator  $\mu \frac{dI}{dz}$  in (2.1). The target value  $I^*$  corresponds to the upstream value along the direction of wave propagation. From the form of (2.2a), this corresponds to the left side value of a spatial interface for  $\mu > 0$  and

right side value for  $\mu < 0$ . This is demonstrated in Fig. 9, where for the boundaries of the domain, boundary conditions  $\bar{I}$  are specified at  $\underline{z}, \mu > 0$  and  $\bar{z}, \mu < 0$ . The other two spatial boundaries,  $\underline{z}, \mu < 0$  and  $\bar{z}, \mu > 0$ , are outflow boundaries where  $I^* = I$  implies that (2.2b) is trivially satisfied. For interior interfaces,  $\mathcal{Q}^+$  and  $\mathcal{Q}^-$  show how the target fluxes are specified. For  $\mathcal{Q}^+$  in  $\mu > 0$ , the upstream value corresponds to the left trace of  $I$  on  $\partial\mathcal{Q}_z$ ; since on the right boundary  $I^* = I$ , the left boundary is the only boundary of the element where the nontrivial jump condition  $\mathcal{R}_{\partial\mathcal{Q}_z} = \mu(I^{out} - I)$  is enforced. Conversely, for  $\mathcal{Q}^-$  in  $\mu < 0$ , the condition  $\mathcal{R}_{\partial\mathcal{Q}_z} = \mu(I^{out} - I)$  is enforced on the right boundary and this residual is trivially satisfied on the left boundary.

The unknown fields in each element are interpolated by tensorial product polynomials of order  $p_z$  in  $z$  and  $p_\mu$  in  $\mu$ . The space of a complete one-dimensional polynomial of order  $p$  can be spanned by a variety of basis functions, such as monomials  $\phi_i(s) = s^i, i = 0, \dots, p$ . For example, for  $p_z = 2$  and  $p_\mu = 1$ , the basis  $\{1, z', z'^2, \mu', z'\mu', z'^2\mu'\}$  is formed by product of monomial bases  $\{\phi_i(z')|i = 0, \dots, p_z\} = \{1, z', z'^2\}$  and  $\{\phi_j(\mu')|j = 0, \dots, p_\mu\} = \{1, \mu'\}$ . The scaled coordinates  $z'$  and  $\mu'$  are given by,

$$\begin{aligned} z' &= 2\frac{z - c_z}{\Delta z} \\ \mu' &= 2\frac{\mu - c_\mu}{\Delta \mu} \end{aligned}$$

where  $c_z$  and  $c_\mu$  are the midpoints and  $\Delta z$  and  $\Delta \mu$  the spans of a quadrilateral element  $\mathcal{Q}$  in  $z$  and  $\mu$  directions, respectively. The use of  $z', \mu' \in [-1, 1]$  prevents ill-conditioning problems that can arise in the global linear system when  $z, \mu$  are directly used to interpolate element solutions. Using the scaled coordinates, the discrete solution field in an element  $\mathcal{Q}$  is interpolated as,

$$I_{\mathcal{Q}}^h(z', \mu') = \sum_{i=0}^{p_z} \sum_{j=0}^{p_\mu} a_{\mathcal{Q}}^{ij} \phi_i(z') \phi_j(\mu') = \sum_{i=0}^{p_z} \sum_{j=0}^{p_\mu} a_{\mathcal{Q}}^{ij} z'^i \mu'^j \quad (2.3)$$

where  $a_{\mathcal{Q}}^{ij}$  are unknowns for element  $\mathcal{Q}$ . Two sample space-angle basis functions are shown in Fig. 10.

The discrete solution is obtained by the solution of the following weighted residual statement,

$$\begin{aligned} \int_{\mathcal{Q}} \check{I} \mathcal{R}_{\mathcal{Q}} dz d\mu + \int_{\partial \mathcal{Q}_z} \check{I} \mathcal{R}_{\partial \mathcal{Q}_z} d\mu &= 0 \\ \int_{\mathcal{Q}} \check{I} \cdot \left\{ \mu \frac{dI}{dz} + \beta I - \frac{\sigma_s}{2} \int_{-1}^1 \Phi(\mu, \mu') I(z, \mu') d\mu' - S \right\} dz d\mu \\ &+ \int_{\partial \mathcal{Q}_z} \check{I} \cdot \mu (I^* - I) d\mu = 0 \end{aligned} \quad (2.4)$$

for all elements  $\mathcal{Q} \in \Omega$ . Since a Galerkin method is used, the weight functions are equal to discrete solution basis functions  $\phi_i(z')\phi_j(\mu')$  within one element  $\mathcal{Q}$  and zero elsewhere, for all elements  $\mathcal{Q}$  and  $0 \leq i \leq p_z$  and  $0 \leq j \leq p_\mu$ . The solution to (2.4) results in a global system of equations whose solution determines  $a_{\mathcal{Q}}^{ij}$  for all elements  $\mathcal{Q}$  in (2.3). The global coupling between different angle ranges  $\mu \in (\mu_j, \mu_{j+1})$ ,  $j \in \{0, \dots, m-1\}$  arises from the triple phase function integral in (2.4) or boundary conditions, such as reflective boundary condition, that can couple all angles at  $z = \underline{z}$  and  $z = \bar{z}$ . The numerical solutions in §2.4 are obtained by the solution of (2.4).

## 2.4 Numerical Examples

### 2.4.1 Method of Manufactured Solutions (MMS)

To validate and provide convergence estimates for the DG RTE code, the Method of Manufactured Solutions (MMS) is used. In the MMS, a solution to the RTE is manufactured that is of the form desired for the given test problem. For the RTE, assume a function form for  $I$ ,

$$I(z, \mu) = f(z, \mu) \quad (2.5)$$

Then, the solution is substituted into the base RTE, and a new source term is generated for the equation that exactly satisfies the partial differential equation.

$$\mathcal{R}_Q = 0 \quad \Rightarrow$$

$$S = \mu \frac{dI}{dz} + \beta I - \frac{\sigma_s}{2} \int_{-1}^1 \Phi(\mu, \mu') I(z, \mu') d\mu'$$

The new source term computed by the MMS is then input into the equation in a discrete solution. If the MS belongs to the space of finite element solution, *e.g.*, when it is a polynomial of order equal or less than that used to interpolate  $I$ , the exact solution is recovered. Otherwise, the discrete solution approaches the MS in the limit of mesh refinement and/or polynomial enrichment. The former approach is used in §2.4.1 and the latter in §2.4.1.

## Validation Study

When  $f(x)$  is a polynomial that belongs to discrete solution space, the FE solution  $I^h(z, \mu)$  should recapture the solution given by  $f(z, \mu)$ . However, due to finite precision errors there will be very small discrepancies between the two solutions that depend on machine precision. In the following examples, the two solutions are compared point-wise with a relative tolerance of  $\varepsilon = 1E - 6$ . All the test cases below share the same spatial(1D) $\times$ angle mesh(1D) mesh as shown in figure 11

It is important to note that each spatial layer  $z^{[i]}$  and angle layer  $\mu^{[i]}$  are subdivided into three bands (elements) and each layer is assigned different and independent material properties  $(\eta_a^{[i]}, \eta_s^{[i]})$  to ensure discontinuity in layers for code verification. Utilizing this setup, the two cases are characterized by a zero and non-zero phase function  $\Phi(z, \mu, \mu')$  within equation 2.1 respectively. For simplicity, the assumed exact solutions are only distinguished by angular layers; all spatial layers within a given angular layer will be assigned the same exact solution based on this angular layer.

**Test case I for  $\Phi(z, \mu, \mu') = 0$**

For a zero phase function equation 2.1 can be rewritten in terms of the source  $S(z, \mu)$  as:

$$S(z, \mu) = \mu \frac{dI}{dz} + \beta I. \quad (2.6)$$

For this relatively simpler case, each angle layer  $\mu^{[i]}$ , for  $i = 1, \dots, 4$  is assigned an assumed exact solution of the following polynomial forms:

$$\begin{aligned} I^{[1]} &= f^{[1]}(z, \mu) = 4.0 + 4.2z + 11.2z^2 - 10.3\mu + 4.0z\mu \\ &\quad + 3.3z^2\mu - 3.1\mu^2 + 2.5z\mu^2 + 4.1z^2\mu^2 \\ I^{[2]} &= f^{[2]}(z, \mu) = 4.0 + 4.2z + 11.2\mu - 10.3z\mu \\ I^{[3]} &= f^{[3]}(z, \mu) = 4.0 + 4.2z + 11.2z^2 - 10.3\mu + 4.0z\mu \\ &\quad + 3.3z^2\mu - 3.1\mu^2 + 2.5z\mu^2 + 4.1z^2\mu^2 \\ I^{[4]} &= f^{[4]}(z, \mu) = 1.0. \end{aligned}$$

In order to ensure that the FEM elements capture the imposed solution through in the element interpolations all elements in the spatial layers  $j$  are interpolated with second order basis order  $p = 2$  for  $z^{[j]}$  and the orders of the basis in the angular layers are  $k = 2$  for  $\mu^{[1]}$ ,  $k = 1$  for  $\mu^{[2]}$ ,  $k = 2$  for  $\mu^{[3]}$ , and  $k = 1$  for  $\mu^{[4]}$ .

With the above exact solution forms and their corresponding source terms defined by equation 2.6, the following solution is generated as visualized in figure 12.

**Test case II for  $\Phi(z, \mu, \mu') \neq 0$**

For a nonzero phase function equation 2.1 can be rewritten in terms of the source  $S(z, \mu)$  as:

$$S(z, \mu) = \mu \frac{dI}{dz} + \beta I - \frac{\sigma_s}{2} \int_{-1}^1 \mu' \Phi(z, \mu, \mu') I(z, \mu'). \quad (2.7)$$

The prescribed Phase function used in this case is of the following polynomial form with  $z$ ,  $\mu$ , and  $\mu'$  orders 2, 1, and 2, respectively:

$$\begin{aligned}\Phi(z, \mu, \mu') = & 4.0 + 4.2z + 11.2z^2 - 10.3\mu + 4.0\mu z + 3.3\mu z^2 \\ & - 3.1\mu' + 2.5\mu'z + 4.1\mu'z^2 - 5.1\mu\mu' - 2.6\mu\mu'z \\ & + 1.3\mu\mu'z^2 - 1.6\mu'^2 + 2.1\mu'^2z - 12.1\mu'^2z^2 \\ & - 15.2\mu\mu'^2 - 7.8\mu\mu'^2z - 2.5\mu\mu'^2z^2\end{aligned}$$

For this more complex problem, each angle layer  $\mu^{[i]}$ , for  $i = 1, \dots, 4$  is assigned the exact solution of the following polynomial form:

$$\begin{aligned}I^{[i]} = f^{[i]}(z, \mu) = & 4.0 + 4.2z + 11.2z^2 - 10.3\mu + 4.0z * \mu \\ & + 3.3z^2\mu - 3.1\mu^2 + 2.5z\mu^2 + 4.1z^2\mu^2, \text{ for } i = 1, \dots, 4\end{aligned}$$

For this case all elements in the spatial layers  $j$  and in the angular layers  $i$  are interpolated with second order basis  $k = 2$  for  $z^{[j]}$ , and  $k = 2$  for  $\mu^{[i]}$  respectively.

With the above exact solution forms and their corresponding source terms defined by equation 2.7, the following solution is generated as visualized in figure 13.

## Convergence Study

The MMS was performed with harmonic functions for both the phase and intensity to perform a convergence study for the proposed DG RTE method. These functions are chosen as

$$I^{exact}(z, \mu) = f(z, \mu) = \sin\left(\pi\frac{z}{L}\right) \sin(\pi\mu) \quad (2.8a)$$

$$\Phi(z, \mu, \mu') = \eta_s(z, \mu) \cos\left((\mu - \mu')\frac{\pi}{2}\right) \quad (2.8b)$$

The L2 norm of the point-wise error  $\mathcal{E}$  between the discrete and exact solution is used to characterize numerical error,

$$\text{Point-wise error: } \mathcal{E} = I^h(z, \mu) - I^{exact}(z, \mu)$$

$$\text{L2 norm of error: } L^2(\mathcal{E}) = \sqrt{\int_{\Omega} \Omega \|\mathcal{E}\|^2} = \sqrt{\int_{\Omega} \Omega (I^h(z, \mu) - I^{exact}(z, \mu))^2}.$$

Since the exact solution (2.8a) is not a polynomial and does not belong to DG solution space, there will exist a finite discrete solution error. The rate of the convergence of the solution is obtained by determining the slope  $\nu^p$  of the logarithm of the solution error versus logarithm of element size  $h$ . Polynomial order of  $p = p_z = p_{\mu} = 0$  to  $p = p_z = p_{\mu} = 3$  are used to interpolate  $I$  in both space and angle. As shown in Fig. 14, asymptotic convergence rate of  $\nu^p = p + 1$  is achieved for polynomial order  $p$  as  $h \rightarrow 0$ .

## 2.4.2 Benchmark problems

Consider radiative transfer in an anisotropically scattering slab of thickness of  $L$  with space dependent scattering coefficient,  $\sigma_s(z) = z/L$ , and a unit extinction coefficient,  $\beta = 1$ . The anisotropic phase function,  $\Phi(\mu, \mu')$ , is assumed to be

$$\Phi(\mu, \mu') = \sum_{m=0}^M a_m P_m(\mu) P_m(\mu'), \quad (2.9)$$

where  $a_m$  are specified constants,  $P_m$  are Legendre polynomials, and  $M$  is the order of anisotropic scattering. In this paper, the slab is a forward-scattering medium with  $M = 7$  and  $a_m = \{1.0, 1.98398, 1.50823, 0.70075, 0.23489, 0.05133, 0.00760, 0.00048\}$ . Two cases of isotropic and anisotropic incident radiations at the left boundary surface are investigated. The numerical results are compared with analytic solutions for the first case, as well as the least-square finite element method (LS) and LS employing the discrete ordinates method (LS-DOM) [96] for both cases.

## Isotropic incidence

The boundary conditions in this case are given by,

$$\begin{cases} I(z = 0, \mu) \cdot \hat{n}_z = 1, & \mu > 0 \\ I(z = 1, \mu) \cdot \hat{n}_z = 0, & \mu < 0 \end{cases}. \quad (2.10)$$

The basis order in both space and angle is  $p = 4$ . As shown in Fig. 15, the computations are performed in a  $6 \times 8$  finite element grid with refinement at  $\mu = 0$  to resolve the strong gradients.

The distribution of radiative intensity in spatial and angular domain is shown in Fig. 16 obtained by LS [96] and DG methods, respectively. It shows that DG results are in agreement with LS results.

Figure 17 shows the exit, the outflow boundaries, distributions of radiative intensity at  $z = 0$  and  $z = 1$ , respectively. For the purpose of comparison, analytic solutions of Cengel and Özişik [22] are plotted, and numerical results obtained by LS method and LS-DOM method [96] are also shown. Obviously, DG results are in good agreement with those results.

The radiative heat fluxes for forward ( $\mu > 0$ ) and backward ( $\mu < 0$ ) are defined by

$$q^+(z) = 2\pi \int_0^1 I(z, \mu) \mu d\mu \quad (2.11a)$$

$$q^-(z) = -2\pi \int_{-1}^0 I(z, \mu) \mu d\mu \quad (2.11b)$$

In this paper, the backward and forward radiative heat fluxes are normalized by the inflow flux,  $2\pi \int_0^1 I(0, \mu) \mu d\mu$ , for the comparison purpose. Fig. 18 shows that the results by DG method coincide with the analytic solution [22] and those results by the LS and LS-DOM method [96].

The computed results of hemispherical reflectivity ( $q^-(z = 0)$ ) and transmissivity ( $q^+(z = 1)$ ) of the slab in Table 1 are in agreement with the analytic values of Cengel and özişik [22] and the results obtained by LS method and LS-DOM method.

### Anisotropic incidence

In this case, the anisotropic incidence boundary condition is adopted. The incident radiation at boundary  $z = 0$  arrives along specified directions, and can be expressed as [96],

$$\begin{cases} I(z = 0, \mu) \cdot \hat{n}_z = g(\mu), & \mu > 0 \\ I(z = 1, \mu) \cdot \hat{n}_z = 0, & \mu < 0 \end{cases} \quad (2.12)$$

where

$$g(\mu) = \begin{cases} 0 & 0.0 < \mu \leq 0.1 \\ \frac{1}{2} \left\{ 1 + \sin \left[ \frac{\pi}{0.1} (\mu - 0.15) \right] \right\} & 0.1 < \mu \leq 0.2 \\ 1 & 0.2 < \mu \leq 0.5, \\ \frac{1}{2} \left\{ 1 - \sin \left[ \frac{\pi}{0.1} (\mu - 0.55) \right] \right\} & 0.5 < \mu \leq 0.6 \\ 0 & 0.6 < \mu \leq 1.0 \end{cases}, \quad (2.13)$$

and the function  $g(\mu)$  defines a piece-wise constant radiative intensity distribution between 0 and 1, with smooth transitions by sinusoidal curves. Fig. 19 shows the contour plots of radiative intensity in spatial and angular domains solved by DG and LS [96] methods.

The exit distributions of radiative intensity at  $z = 0$  and  $z = 1$  are depicted in Fig. 20, respectively. Results obtained by the DG method agree well with those results by the space-angle LS method. As expected results obtained by a hybrid LS method for space, and DOM in angle are less accurate due to discrete nature of this solution in angle, i.e., the so-called ray effect.

Backward and forward radiative heat flux distributions are shown in Fig. 21, respectively. Also compared with the results by LS-DOM method, backward and forward radiative heat flux distributions by the DG method are in better agreement with those obtained by the LS method [96].

Table 2 shows that the computed reflectivity and transmissivity of a slab are in good agreement with those results obtained by LS method [96].

### 2.4.3 Point source

In addition to the benchmark problems detailed above, several other test problems were chosen to evaluate the DG formulation. The method has capability to have point sources  $S_I(\bar{z}, \bar{\mu})$  on both the boundary and interior of the domain. For a source term at point  $(\bar{z}, \bar{\mu})$ , the source term value at any arbitrary point within the computational domain at point  $(z, \mu)$  with respect to the reference source can be written as,

$$S(z, \mu) = S_I(\bar{z}, \bar{\mu})\delta(z - \bar{z})\delta(\mu - \bar{\mu})$$

where  $S_I(\bar{z}, \bar{\mu})$  is the intensity of the point source.

The first test case was run with scattering neglected, i.e a zero phase function. The left boundary was subject to a vacuum (homogeneous) boundary condition,

$$I(0, \mu) \cdot \hat{n}_z = 0$$

while the right side was given a reflective boundary.

$$I(1, -\mu) \cdot \hat{n}_z = I(1, \mu) \cdot \hat{n}_z.$$

These boundary conditions hold for each test case given in this section. The slab was discretized with a 16x 32 grid in the  $(z, \mu)$  domain with element order  $p = 0$ . The

given point source term is,

$$S(z = 0.375, \mu = 0.75) = 10$$

With the goal to solve the problem with higher order elements, the domain is solved with  $p = 1$  in Fig. 22b. This test case highlights an issue with numerical error, caused by numerical overshoot and undershoot, near the point source location. We obtain negative values for  $I$ , which are obviously nonphysical. This is caused by direct integration of the point source in the element(s) containing it. Since delta function has no inherent length scale, this problem persists regardless of the resolution of the mesh. That is  $h$ -refinement does not address it. In addition,  $p$ -enrichment, increasing the order of element, generally exacerbates the problem.

To address the undershoot (and overshoot) problem, we propose to use the average of the point source over the elements covering it. Therefore, instead of a delta function source of magnitude  $S$  over elements with space-angle area  $\Delta z \Delta \mu$ , the source term becomes a uniform  $S_a$  of magnitude,

$$S_a(z, \mu) = \frac{S_I(\bar{z}, \bar{\mu})}{\Delta z \Delta \mu} \quad (2.14)$$

This averaging scheme approximates the delta function at a resolution that is dictated by the underlying DG grid size. Clearly, as the element size  $h$  of the element(s) containing delta source approach zero, the solution tends to exact solution wherein  $I$  focuses on angle  $\bar{\mu}$  with infinite intensity. Figure 22e shows the result obtained by using the average source term for the same grid specification in Fig. 22b. As can be seen, the numerical undershoot is resolved, thereby removing the non-physical negative intensity.

With this issue resolved,  $h$ -refinement was performed in Fig. 22d. Using a refinement ratio of two, a  $32 \times 64$  grid is used for this example. Due to the halving of the mesh resolution in each direction, the area over which the point source is averaged

is divided by four, resulting in fourfold increase in  $S_a$ . By inspecting the weighted residual statement (2.4), and the averaging scheme (2.14) one can show that when angular size of elements is halved, the maximum observed  $I$  doubles for this problem. This feature can be observed in comparison of Figs 22c and 22d.

Figure 22e shows a  $p$ -enrichment with respect to the solution in 22d, where element order is increased from  $p = 1$  to  $p = 3$ . For this particular problem,  $p$ -enrichment does not drastically change the solution, although the variation of  $I$  from the element of application of point source down to the reflected side is slightly smoother. Finally, Fig. 22f solves this problem when Rayleigh scattering is used, where the phase function,  $\Phi(\mu, \mu')$  is given,

$$\Phi(\mu, \mu') = \frac{3}{8} (3 - \mu^2 - \mu'^2 + 3\mu^2\mu'^2)$$

The small values of  $I$  at angles other than those covered by the source term and its reflection are caused by scattering of these rays.

#### 2.4.4 Properties of the space-angle DG formulation

In this section, two cases are conducted to further elaborate on the properties of the space-angle DG formulation, as opposed to those by continuous methods or methods with low order of accuracy in angle. The first case mainly focuses on the discontinuous property of the DG method. The second case shows the advantages of the DG method, when a high order of accuracy in angle is needed.

##### Discontinuous basis functions in both space and angle

To further show the capability of the DG method, an angular-line source is added in the  $(z, \mu)$  domain with a  $16 \times 32$  grid. The scattering is neglected to clearly demonstrate the advantage of using a DG formulation in the angle direction. The

given intensity source term is,

$$S(z, \mu) = \delta(z - 0.4) [-100(\mu - 0.5)^2 + 5.76], \quad \mu \in [0.26, 0.74]$$

That is, the source term is the product of a delta function in space and a second order parabola with a maximum value of 5.76 at  $\mu = 0.5$  in angle. This corresponds to a line source along  $\mu$ . The left boundary is given a vacuum boundary condition, while the right boundary is a reflective boundary wall. The polynomial order of the solution is  $p = 3$  in space and angle.

Similar to the point source case, the wave propagating forward does not pollute the solution of the upstream elements in space ( $M_z$  in Fig. 23), *i.e.*, ahead of the source term the solution remains zero as physically it should be. This is made possible by using the upstream value for the target solution at a quadrature point on vertical inter-element boundaries; *cf.* (2.2b) and Fig. 9. Another interesting observation is the high order approximation of the solution in the elements that contain the source line (shown by the white thick line) and downstream of it. The smoothness of the source term in the angle direction also facilitates a higher order solution in space; unlike the point source problems in §2.4.3, there was no need to evenly distribute the source term in space, in the elements containing it, to avoid negative solution for  $I$ .

The DG method also ensures that elements in angle direction that should have zero solution, will end up with zero solution. Three groups of elements can be seen in terms of approximating the source term in angle. For the 6 inner most layers in angle, the source term is entirely nonzero and smooth within the elements. The solution variation in angle is accurately captured by the second order polynomial in angle within each of these elements. For the elements right on top and bottom of these 6 angular layers, the source term only penetrates half way though the elements, as indicated by the white line. Since the solution is second order in angle in an element, the discontinuous nature of the solution in angle cannot be exactly captured in these elements. Specifically, we do not recover a zero solution right outside the source term

angular span within these elements. Finally, in the next immediate upward  $N_\mu^+$  and downward  $N_\mu^-$  angular neighbors in Fig. 23, the finite elements capture the exact zero solution.

The methods that enforce the continuity of solution cannot capture either of these feature exactly. For example, if a continuous finite element method is used in space, due to the continuity constraint of the solution, the source term incorrectly penetrates a bit in the upstream elements in the  $M_z$  region. Likewise, if a continuous finite element approximation is employed in the angle, again due to the same continuity constraint, the elements in layers  $N_\mu^+$  and  $N_\mu^-$  end up with nonzero solution. The same holds true for the spherical harmonic and other methods that use globally continuous functions to approximate the solution in angle. This example demonstrates that the discontinuity of the solution between elements, and the use of physically-based target values in DG methods lends itself to accurate solutions for the RTE.

### High order of accuracy in angle

To better understand the importance of high order of accuracy in angle for solving the RTE, the same example for the convergence study in §2.4.1 is solved again. However, the polynomial order in angle is fixed to be  $p_\mu = 0$ , while the polynomial order in space is still set to be  $p_z = 0$  to  $p_z = 3$ . It is clear in Fig. 24 that the convergence rate does not improve (stays at 1) as the low order of  $p_\mu = 0$  limits the convergence rate. That is, the convergence rate  $\nu^{p_z} = p_z + 1$  no longer holds as  $h \rightarrow 0$ . Because of this low convergence rate, the errors are significantly larger for this configuration, especially for smaller elements. This is evident in an about 13 binary orders of magnitude higher error for  $p_z = 3$ ,  $\log_2 h \approx -3.6$  in Fig. 24 compared to the corresponding solution in Fig. 14.

This example demonstrates that going to high spatial orders can be a waste of computational resources given that the convergence rate is hindered by such a low angular order. Methods that use FE in space and use a low order scheme in angle, basically gain not much accuracy by using a high order approximation in space. The

variation of the DG method presented in this section, resembles a hybrid DG in space and FV, FD, or DOM method in angle, given that the order of polynomial solution in angle is zero. From this perspective, we can compare it to the hybrid DG-DOM in [139]. As mentioned, many of these methods cannot change the order of accuracy in angle.

Other methods, such as the spherical harmonic method and spectral FEMs in angle, have the same capability of the DG method in that the solution can be arbitrarily high order in angle. But these methods basically have two disadvantages in comparison to the DG method. First, due to the global nature of interpolation functions in angle, no local adjustment of the order of accuracy in angle can be made. Second, there is a tendency for such methods to result in oscillatory solution, especially, when dealing with concentrated sources. The example of the angular-line source term in §2.4.4 does not exhibit any of these problems. First, in principal, in the DG method the order of each element can be adapted when needed, such as a zeroth order in angle for elements excluding the line source and high orders for elements that span the source line. Second, the locally high order methods such as FEMs and especially DG methods are less prone to nonphysical solutions oscillations. For example no oscillations are observed in the angle direction for the point and line source problems in §2.4.3 and §2.4.4. However, it is noted that for problems that have very smooth and globally nonzero solutions in angle, spherical harmonic and spectral methods in angle may be preferred due to their exponential convergence property.

## 2.5 Discussion and conclusions

The FEM enables high order solution for the RTE in space and can readily handle complex geometries. The continuous representation of solution for angle spans and high order solution in this direction makes using finite elements in angle direction promising as well. Such space-angle FEM methods have shown better accuracy, than

hybrid FEM-SN (FEM-DOM) or FEM-PN methods, as for example can be seen in Fig. 19a for the LS and LS-DOM methods.

While both the proposed space-angle DG method and the LS method [96] show very good accuracies for the problems considered in §2.4.2, there are some important differences. First, the RTE models a wave propagation equation along individual ray directions. Unlike continuous FEMs, which enforce the continuity of solution between neighboring elements, DG methods enforce continuity only along direction implied by the RTE (2.1). For example, in Fig. 9 continuity is enforced only along the upstream spatial direction and no angular continuity is enforced. This explains why the source term in Figs 22a to 22f do not pollute the upstream element (and neighboring elements in angle direction when phase function is zero). If continuous Galerkin elements were used, the solution in such immediate neighboring elements would not have been zero.

The examples in §2.4.4 are used to further elaborate on the discontinuity property of the space-angle DG method, especially in angle direction. The solution of the spherical harmonic or other methods that use continuous solution in the entire space and/or angle, tend to exhibit non-physical oscillations. The weak enforcement of the jump conditions between the elements relaxes such global continuity constraint and results in a better solution when the DG method is used. In addition, since the line source term in §2.4.4 is a second order polynomial in angle, it is more accurate and efficient to use this high space-angle order DG formulation. In fact, high order accuracy in angle is quite necessary as discussed in §2.4.4. The convergence rates in Fig. 24 show that the low order in angle limits the overall convergence rate. When more accurate solutions are required, the gain in efficiency and accuracy of a space-angle high order method is substantially more than a space-only high order method, such as a hybrid FEM-DOM formulation. For the convergence study problem presented, by using a high order approximation in angle, the error was reduced by about 13 binary orders of magnitude for the smallest elements considered, compared to a space-only high order formulation.

Another main advantage of the DG method is the increased flexibility offered in both  $h$  and  $p$  adaptivity, wherein the size and order of elements can change from one element to another one without the need for connecting elements used in continuous FEMs. For example, by using  $h$ -adaptivity we could have highly refined elements around the source term location in §2.4.3, while leaving the other elements coarse. In [6] a novel adaptive scheme is proposed in which for dynamic problems space and time are simultaneously adapted when needed. We are currently working on a similar scheme where instead of physical time, angular direction is simultaneously adapted along with space directions, as for example in Fig. 24, where elements including the source term can undergo  $h$ - and  $hp$ -adaptivity, while elements having no source term remain zeroth order. Moreover, the fully discretized DG method in space and angle is also promising to solve more types of the RTE, such as the multi-dimensional RTE in different space and angle configurations and the polarized (vector) form of the RTE.

## Chapter 3

# Space-Angle Discontinuous Galerkin Method for Radiative Transfer between Concentric Cylinders

### 3.1 Abstract

The integro-differential radiative transfer equation (RTE) for concentric cylinders problem involving scattering, absorption and emission is solved using the discontinuous Galerkin (DG) finite element method (FEM). The space-angle DG method directly solves the cylindrically-symmetric RTE as a three-dimensional problem, where a 1D spatially domain in radial distance  $r$  is twice extruded in the cosine of polar angle ( $\mu$ ) and the difference in azimuthal angle ( $\tilde{\varphi}$ ) directions. Thus, the method has a higher accuracy than hybrid FEM-Discrete Ordinate ( $S_N$ ) and FEM-Spherical Harmonic ( $P_N$ ) methods. This is reflected by numerically verified convergence rate of  $p + 1$  for smooth problems and space-angle polynomial interpolation order of  $p$ . The axisymmetric RTE formulation is more complicated than the plane-parallel formulation, for having two independent angle directions ( $\mu$  and  $\tilde{\varphi}$ ) and an extra derivative term with respect to  $\tilde{\varphi}$  in the differential equation. This results in a complex characteristic structure in  $r - \tilde{\varphi}$  plane with strong discontinuity lines in radiation intensity  $I$ . A method of characteristics is formulated and implemented to verify the DG formulation and demonstrate its accuracy when such strong discontinuities persist in the solution, specifically when there are no scattering and absorption terms. The relaxation of inter-element continuity constraint of continuous FEMs by this DG method implies its superiority in numerically capturing such discontinuities. Finally, a benchmark problem pertained to heat radiation in a gray gas and another one with nonzero phase function demonstrate the effectiveness of the method in modeling black-body and scattering angular integration terms.

### 3.2 Introduction

The *Radiative Transfer Equation* (RTE), a first order integro-differential equation, describes the radiation intensity while propagating in an absorbing and scattering medium. The RTE plays an important role in radiation transfer in atmosphere,

semitransparent liquid and solids, porous materials, and many other participating media [109, 88]. Different numerical methods have been formulated to solve the RTE over the past few decades. These methods, including *Finite Volume* (FV) method [31] and *Finite Element Method* (FEM) [99], are commonly hybridized with the *Discrete Ordinates Method* ( $S_N$  or DOM) [49, 114] or *Spherical Harmonic Method* ( $P_N$ ) [46, 89, 15] to handle the integrals over the solid angle.

In  $S_N$  methods, the angular dependence of radiation intensity in the RTE is decoupled by the angular discretization using a discrete set of directions (discrete ordinates) while the integral terms are replaced by quadratures. The spatial dependence in the RTE is discretized by the numerical methods mentioned above. Thus, the RTE and its corresponding boundary conditions are transformed into a set of *Partial Differential Equations* (PDEs) only in terms of the spatial coordinates. Two drawbacks of the classical  $S_N$  method are known as *false scattering* and the *ray-effect* [17] that mainly caused by the form of angular discretization [23]. In addition, the  $S_N$  method can be problematic when specularly reflecting boundaries are present [102]. If a reflected beam on the boundary does not coincide with any discrete ordinate, the intensity of the specularly reflected beam is generally undetermined. Besides, special schemes are needed in the DOM for coping with the angular derivative terms in the RTE in curvilinear coordinates [104]; that is, the angular redistribution [81] makes it difficult to handle the angular derivative terms in the RTE.

In  $P_N$  methods, the radiation intensity field is approximated by an orthogonal series of spherical harmonics, thereby giving the method its name [109]. In the spherical harmonics series, each term has one spatial coefficient and one angular coefficient. After the integration, the expansion coefficients are formulated into a set of PDEs. The drawbacks of the  $P_N$  method are the derivation of the set of PDEs and the corresponding boundary conditions for high-order approximations, tendency of getting nonphysical oscillations and negative values for radiation intensity for high order approximations [43], and the lack of accuracy in optically thin media [24].

The (continuous) FEM is a versatile method that can simulate a wide range of problems in scientific and engineering fields which allows complex geometries. It has also been used for solving the RTE in the spatial domain by Shmygevkii [108], Krim [1], Razzaghi [98], Sallah [105], and Egger *et al.* [44]. When solving the RTE in spatial domain by the FEM, the radiation intensity is approximated by a series of shape functions in space. FEMs are generally preferred over FV and *Finite Difference* (FD) methods if higher orders of accuracy are sought. However, continuous FEMs do have a disadvantage in dealing with discontinuous and high gradient solution features. This is particularly important for the RTE, since the propagation of rays along characteristics can result in strong discontinuities in radiation intensity. The *Discontinuous Galerkin* (DG) method is more appropriate for this class of problems, including the RTE, since it relaxes the strong inter-element continuity of continuous FEMs.

The DG method was originally introduced by Reed and Hill [101] to study the neutron transport equation. For DG methods the basis functions are discontinuous across element interfaces; accordingly the jump between interior traces of solution and the so-called numerical fluxes is weakly enforced on inter-element boundaries. DG methods are specifically suitable for hyperbolic PDEs and the RTE, since the evolution of solution along characteristics can result in (strong) discontinuities. Several hybrid DG methods such as the  $S_N$ -DG method [84, 139, 58, 45, 33, 133], and the  $P_N$ -DG method [75] have been proposed, wherein the spatial domain is discretized by the DG method.

One can take advantage of FEM and DG methods to discretize the entire spatial and angular domain rather than only the spatial domain, as in the aforementioned hybrid DG methods. Liu [83] and Pontaza [96] used the FEM in both space and angle to solve the one-dimensional RTE. Castro and Trelles [21] developed the spatial and angular finite element to solve multi-dimensional RTE with high order of accuracy. Gao and Zhao [50, 51] associated the DG in space with a piece-wise constant FEM in angle. As in the spatial domain, continuous methods may fail to accurately capture

discontinuities of the solution that can occur in the angular domain. Formulating a DG method in both space and angle is desirable since it prevents the artificial continuity constraint of hybrid DG methods in angle. Moreover, arbitrarily high orders of accuracy can be achieved both in space and angle directions. Kophazi and Lathouwers [73] implemented the DG method in both space and angle to solve the Boltzmann transport equation. Kitzmann *et al.* [37] solved the one-dimensional RTE with spherical symmetry by the DG method. In previous works [29, 27], a high order space-angle discontinuous Galerkin (DG) method for the plane-parallel RTE was proposed.

There are fewer computational works for the steady state radiative heat transfer in one-dimensional cylindrical medium compared to plane-parallel and some other RTEs. Some numerical methods formulated for this problem are *Monte Carlo* (MC) [62] and variational [86, 69, 94] methods. Nowadays, with the huge improvement of computing power, the MC method can solve this type of radiative transfer problems efficiently and accurately. In fact, due to its accuracy, the MC method has been recommended as benchmark for comparison of other methods [116, 16]. Besides, the MC method can handle complex geometries easily, and have a low algorithmic complexity. However, it has disadvantages. For example, for intensively scattering cases, it becomes very slow because of the exponentially increasing number of photon interactions. For the computation of conduction and/or convection parts involved in the problems, it is difficult for the MC method match the required grid size needed for coupling other grid-based method, whereas, it is relatively easy for the DG method in this case. No matter what method is used, a few difficulties associated with the one-dimensional cylindrical RTE are: (1) it involves two independent variables in angle direction, which results in a high dimensional problem in spatial and angular domain; (2) an additional angular derivative term in the RTE in curvilinear coordinates requires the specification of target fluxes and their integration on new angle-normal element interfaces; (3) the additional angular term results in curved characteristics in space and angle and more complex jump manifolds for radiation intensity. For

simplification, only the steady state radiative transfer in gray media is discussed in this paper. The spectral radiation is not focused here. However, the existing approaches to band correlation can help study the spectral properties by providing the radiative intensity in a set of gray gases and the probability density function (PDF) of absorption coefficient [61]., *e.g.*,  $k$ -distribution method [113], correlated- $k$  method [54, 82] and spectral-line-weighted sum-of-gray-gases (SLWSGG) [132, 110]

The remainder of manuscript is structured as follows. The formulations of the method of characteristic and the DG method for the steady state RTE in one-dimensional cylindrical coordinates are presented in §3.3. The implementation of the DG method and the required extrusion operations in the angle direction and the implementation of the method of characteristics are described in §3.4. Next, several numerical examples are presented in §3.5 to verify and validate the DG formulation. This includes the use of *Method of Manufactured Solution* (MMS), an example of a sharp discontinuous solution in space and angle obtained by the method of characteristic, a benchmark problem from [86], and another problem in an anisotropic scattering medium. Final conclusions are drawn in §3.6.

## 3.3 Mathematical description

### 3.3.1 Radiation transfer equation and boundary conditions

The general form of RTE for a gray medium is,

$$\frac{dI(\mathbf{x}, \hat{\mathbf{s}})}{ds} = -\beta I(\mathbf{x}, \hat{\mathbf{s}}) + \kappa I_b(\mathbf{x}) + \frac{\sigma_s}{4\pi} \oint_{4\pi} I(\mathbf{x}, \hat{\mathbf{s}}') \Phi(\hat{\mathbf{s}}, \hat{\mathbf{s}}') ds' + S(\mathbf{x}, \hat{\mathbf{s}}). \quad (3.1)$$

This equation describes the change of radiation intensity  $I(\mathbf{x}, \hat{\mathbf{s}})$  at spatial location  $\mathbf{x}$  along the path  $ds$  in the angle space with angle coordinate  $\hat{\mathbf{s}}$ . The values  $\beta$ ,  $\kappa$ , and  $\sigma_s$ , are the spatial-dependent extinction, absorption, and scattering coefficients, respectively. The anisotropic scattering phase function is represented by  $\Phi(\hat{\mathbf{s}}, \hat{\mathbf{s}}')$  and  $s'$  is the solid angle for phase function integration. The solid angle differential for  $s'$  is

denoted by  $ds'$ . The spatial-dependent total black-body radiation intensity is given by  $I_b$ . The source term is denoted by  $S(\mathbf{x}, \hat{\mathbf{s}})$ . If radiative equilibrium prevails,  $I_b$  is [88],

$$I_b(\mathbf{x}) = \frac{1}{4\pi} \oint_{4\pi} I(\mathbf{x}, \hat{\mathbf{s}}') ds' \quad (3.2)$$

For one-dimensional axisymmetric problems (infinite in  $z$  direction), the RTE for a gray medium that emits, absorbs and anisotropically scatters in an cylindrical enclosure is written as,

$$\begin{aligned} & \sin \theta \cos \tilde{\varphi} \frac{\partial I(r, \mu, \tilde{\varphi})}{\partial r} - \frac{\sin \theta \sin \tilde{\varphi}}{r} \frac{\partial I(r, \mu, \tilde{\varphi})}{\partial \tilde{\varphi}} \\ & = -\beta I(r, \mu, \tilde{\varphi}) + \kappa I_b(r) + \frac{\sigma_s}{4\pi} \int_{-\pi}^{\pi} \int_{-1}^1 I(r, \mu', \tilde{\varphi}') \Phi(\mu, \tilde{\varphi}, \mu', \tilde{\varphi}') d\mu' d\tilde{\varphi}' + S(r, \mu, \tilde{\varphi}), \end{aligned} \quad (3.3)$$

where the spatial location  $\mathbf{x}$  is represented in polar coordinates with  $r$ ,  $\varphi_x$ , and  $z$  corresponding to radial distance, spatial azimuthal angle, and coordinate along the axis of symmetry, respectively. The spherical coordinates of solid angle  $\hat{\mathbf{s}}$  are polar angle  $\theta$  and angular azimuthal angle  $\varphi_s$ , as shown in Fig. 25. The radiation intensity is expressed as  $I(r, \mu, \tilde{\varphi})$ , where  $\mu = \cos(\theta)$  \* and  $\tilde{\varphi}$  is the azimuthal angle measured from the local radial direction; that is,  $\tilde{\varphi} = \varphi_s - \varphi_x$ . The spatial coordinates  $z$  and  $\varphi_x$  are removed due to invariance along the axis of symmetry, and angular symmetry of the problem (enabling the use of  $\tilde{\varphi}$  instead of two coordinates  $\varphi_s$  and  $\varphi_x$ ). The direction of the ray at point  $\mathbf{x}$  and angular coordinates  $\theta$  and  $\tilde{\varphi}$  is expressed as  $\hat{\mathbf{s}} = (\sin \theta \cos \tilde{\varphi}, \sin \theta \sin \tilde{\varphi})$ . To guarantee the energy conservation, the phase function is normalized as,

$$\frac{1}{4\pi} \int_{-\pi}^{\pi} \int_{-1}^1 \Phi(\mu, \tilde{\varphi}, \mu', \tilde{\varphi}') d\mu' d\tilde{\varphi}' = 1. \quad (3.4)$$

---

\*Since, the spatial coordinate  $(r, \varphi_x, z)$  does not include a spatial azimuthal angle, the subscript  $s$  is dropped from angular azimuthal angle and its cosine value for brevity.

Equation (3.3) is solved on the three-dimensional domain  $(r, \mu, \tilde{\varphi}) \in \Omega = (R_1, R_2) \times (-1, 1) \times (-\pi, \pi)$ , where  $R_1$  and  $R_2$  are the radii of inner and outer surface walls; cf. Figure 25. For an opaque surface that emits and reflects specularly and diffusively, the radiation intensity on the domain boundary,  $R_w$ , with index  $w \in \{1, 2\}$  referring to the inner and outer radii, is given by [88],

$$I(R_w, \hat{\mathbf{s}}) = \epsilon(R_w)I_b(R_w) + \frac{\rho^d(R_w)}{\pi} \int_{\hat{\mathbf{s}}' \cdot \mathbf{n} > 0} I(R_w, \hat{\mathbf{s}}') \hat{\mathbf{s}}' \cdot \mathbf{n} d\mu' d\tilde{\varphi}' + \rho^s(R_w)I(R_w, \hat{\mathbf{s}}_s) \quad (3.5)$$

where  $\mathbf{n}$  is the surface normal,  $\epsilon$  is the wall emissivity and  $\rho$  is the reflectivity divided in a diffuse component  $\rho_d$  and a specular component  $\rho_s$  with the relationship,  $\rho = \rho_d + \rho_s$ . Since the surface is opaque,  $\epsilon + \rho = 1$ . The first term on the right side of (3.5) arises from the surface emission. Under the assumption of diffuse-gray  $I_b = n^2 \sigma T^4 / \pi$  [88]. The second term is the diffusively reflected component. The third term is the specularly reflected component, where  $\hat{\mathbf{s}}_s$  is the specular direction defined as the direction of a light beam traveling from the surface in a direction of  $\hat{\mathbf{s}}$  after a specular reflection. This direction is given by  $\hat{\mathbf{s}}_s = \hat{\mathbf{s}} - 2(\hat{\mathbf{s}} \cdot \mathbf{n})\mathbf{n}$ . Equation (3.5) is specified on the inflow boundaries which are defined when  $\hat{\mathbf{s}} \cdot \mathbf{n} > 0$ .

### 3.3.2 Characteristic directions for the RTE

The method of characteristics was firstly introduced to solve the RTE in 1970 [20]. Rukolaine *et al.* [102] extended this method to solve the 2-D RTE in cylindrical coordinates with complex boundary conditions. By solving *Ordinary Differential Equations* (ODEs) along the characteristic lines, this method provides physical insight on how the rays propagate in the space-angle domain and can be computationally advantageous for high spatial or angular dimension problems.

To validate DG solution, the method of characteristics is introduced. Along a characteristic line, the RTE takes the form,

$$\frac{dI}{ds} = \check{S}(r, \mu, \tilde{\varphi}), \quad (3.6)$$

where  $\check{S}$  is the *total source term* which is the right hand side of (3.3),

$$\begin{aligned} \check{S}(r, \mu, \tilde{\varphi}) &= -\beta I(r, \mu, \tilde{\varphi}) + \kappa I_b(r) \\ &+ \frac{\sigma_s}{4\pi} \int_{-\pi}^{\pi} \int_{-1}^1 I(r, \mu', \tilde{\varphi}') \Phi(\mu, \tilde{\varphi}, \mu', \tilde{\varphi}') d\mu' d\tilde{\varphi}' + S(r, \mu, \tilde{\varphi}). \end{aligned} \quad (3.7)$$

Equation (3.6) is written as,

$$\mathbf{V} \cdot \left( \frac{\partial I}{\partial r}, \frac{\partial I}{\partial \mu}, \frac{\partial I}{\partial \tilde{\varphi}} \right) = |\mathbf{V}| \frac{dI}{dl} = \check{S}, \quad (3.8)$$

where  $\mathbf{V} = (\sin \theta \cos \tilde{\varphi}, 0, -\frac{\sin \theta \sin \tilde{\varphi}}{r})$ ,  $\tilde{\mathbf{e}} = \frac{\mathbf{V}}{|\mathbf{V}|}$  is the unit vector (direction) along the characteristic, and  $l$  is the length coordinate along the characteristic starting from the inflow (upstream) towards the outflow (downstream), tangent to  $\tilde{\mathbf{e}}$  as shown in Fig. 26. The relation between the increments of space-angle coordinates and characteristic length is,

$$\begin{aligned} dr &= \frac{\sin \theta \cos \tilde{\varphi}}{|\mathbf{V}|} dl, \\ d\mu &= 0, \\ d\tilde{\varphi} &= -\frac{\sin \theta \sin \tilde{\varphi}}{r|\mathbf{V}|} dl, \end{aligned} \quad (3.9)$$

accordingly, characteristic lines stay in the  $r - \tilde{\varphi}$  plane, since  $d\mu = 0$ .

The ODE (3.8) is solved starting from inflow parts of spatial boundary of  $\Omega$  (at  $R_1$  or  $R_2$ ), where  $I$  is given at the beginning of characteristic lines as initial condition. This can easily be done when there are no angular integration terms in (3.7), that is when  $I_b, \Phi = 0$ . For details of the implementation of this method when these angle integrals are present, refer to §3.4.2.

### 3.3.3 Discontinuous Galerkin formulation

Figure 27 shows an  $m \times n \times l$  tensor product discretization of space-angle domain  $\Omega = (R_1, R_2) \times (-1, 1) \times (-\pi, \pi)$ , discretized into  $\{r_0, r_1, \dots, r_m\}$ ,  $\{\mu_0, \mu_1, \dots, \mu_n\}$ , and

$\{\tilde{\varphi}_0, \tilde{\varphi}_1, \dots, \tilde{\varphi}_l\}$  along  $r$ ,  $\mu$ , and  $\tilde{\varphi}$  directions, respectively, for  $r_0 = R_1$ ,  $r_m = R_2$ ,  $\mu_0 = -1$ ,  $\mu_n = 1$ ,  $\tilde{\varphi}_0 = -\pi$ , and  $\tilde{\varphi}_l = \pi$ . For an arbitrary element  $\mathcal{Q} \in \Omega$  in Fig. 27, the interior residual corresponding to PDE (3.3) is,

$$\begin{aligned} \mathcal{R}_{\mathcal{Q}} = & \sin \theta \cos \tilde{\varphi} \frac{\partial I}{\partial r} - \frac{\sin \theta \sin \tilde{\varphi}}{r} \frac{\partial I}{\partial \tilde{\varphi}} + \beta I - \kappa I_b \\ & - \frac{\sigma_s}{4\pi} \int_{-\pi}^{\pi} \int_{-1}^1 I(r, \mu', \tilde{\varphi}') \Phi(\mu, \tilde{\varphi}, \mu', \tilde{\varphi}') d\mu' d\tilde{\varphi}' - S(r, \mu, \tilde{\varphi}). \end{aligned} \quad (3.10)$$

For DG methods the continuity of solution on the boundary of elements is weakly satisfied relative to a *target* or *numerical flux*  $I^*$ . As mentioned in §3.2, this relaxes the continuity constraint of continuous finite element methods, which can be both nonphysical and not accurately model the propagation of waves along characteristic lines. For RTE, the residual on  $\partial\mathcal{Q}$ , the boundaries of the element  $\mathcal{Q}$ , corresponds to differential operator  $dI(\mathbf{x}, \hat{\mathbf{s}}) / ds$  in (3.1) and is expressed as,

$$\mathcal{R}_{\partial\mathcal{Q}} = \hat{\mathbf{s}} \cdot \mathbf{n}(I^* - I), \quad (3.11)$$

where  $\mathbf{n} = (n_r, n_{\varphi_x}, n_z)$  is the normal direction on  $\partial\mathcal{Q}$  in spatial coordinates and  $\hat{\mathbf{s}}$  is the direction of radiation.

The target value  $I^*$  corresponds to the upstream value along the direction of wave propagation and is given by,

$$I^* = \begin{cases} I & \hat{\mathbf{s}} \cdot \mathbf{n} \geq 0 \text{ outflow} \\ I^{out} & \hat{\mathbf{s}} \cdot \mathbf{n} < 0 \text{ inflow} \end{cases} \Rightarrow \mathcal{R}_{\partial\mathcal{Q}} = \begin{cases} 0 & \hat{\mathbf{s}} \cdot \mathbf{n} \geq 0 \\ \hat{\mathbf{s}} \cdot \mathbf{n}(I^{out} - I) & \hat{\mathbf{s}} \cdot \mathbf{n} < 0 \end{cases}. \quad (3.12)$$

That is, on outflow boundary of  $\mathcal{Q}$ , where  $\hat{\mathbf{s}} \cdot \mathbf{n} \geq 0$ ,  $I^*$  is set equal to interior trace and the jump condition  $\mathcal{R}_{\partial\mathcal{Q}}$  is trivially satisfied. On the other hand, the inflow boundaries correspond to  $\hat{\mathbf{s}} \cdot \mathbf{n} < 0$ . For inflow boundaries, the target flux is set equal to outside intensity  $I^{out}$ . When the inflow boundary of  $\mathcal{Q}$  is on the boundary of domain,  $\partial\Omega$ ,  $I^{out}$  is set to the boundary flux determined from (3.5). For a point on

an inflow interface of  $\mathcal{Q}$  that is inside  $\Omega$ ,  $I^*$  is set to  $I^{out}$ , the interior trace of  $I$  at the same location for the neighboring element  $\mathcal{Q}^{out}$ . Clearly,  $I^{out}$  is also the target value for the same point on the boundary of neighbor element  $\mathcal{Q}^{out}$ . For  $\mathcal{Q}^{out}$  this point is on its outflow boundary and  $\mathcal{R}_{\partial\mathcal{Q}}$  is trivially satisfied. That is, for any interior interface in  $\Omega$ , there is exactly one non-trivially zero  $\mathcal{R}_{\partial\mathcal{Q}}$  on the side that is inflow boundary. This corresponds to the downstream direction of characteristic lines; *cf.* Fig. 26.

Next, the specific form of  $\hat{\mathbf{s}} \cdot \mathbf{n}$  for axisymmetric RTE in (3.3) is discussed to determine inflow and outflow boundaries of  $\mathcal{Q}$  and  $I^*$  from (3.12). For this configuration  $\hat{\mathbf{s}} = (\sin \theta \sin \varphi_x, \sin \theta \sin \varphi_x, \cos \theta)$ . Since the solution is invariant along  $z$ -direction and  $\varphi_x = -\tilde{\varphi}$  when  $\varphi_s = 0$  the expression for  $\hat{\mathbf{s}} \cdot \mathbf{n}$  in (3.11) is simplified to,<sup>†</sup>

$$\hat{\mathbf{s}} \cdot \mathbf{n} = \sin \theta \cos \tilde{\varphi} n_r - \sin \theta \sin \tilde{\varphi} n_{\tilde{\varphi}}. \quad (3.13)$$

Note that the factors of  $n_r$ ,  $n_{\tilde{\varphi}}$ , and  $n_\mu$  (zero) in  $\hat{\mathbf{s}} \cdot \mathbf{n}$  correspond to the factors of  $dI/dr$ ,  $dI/d\tilde{\varphi}$ , and  $dI/d\mu$  (zero) in (3.10), considering that the geometric Jacobian of the cylindrical coordinate system is equal to  $r$ .

A cubic element in Fig. 27 has 6 boundaries in  $\Omega$ . Figure 28 shows element  $\mathcal{Q}$  and its four neighbors in the  $r$ - $\tilde{\varphi}$  plane. The two boundaries along positive and negative  $\mu$  directions are not shown as  $\hat{\mathbf{s}} \cdot \mathbf{n}$  is trivially zero and there is no coupling between elements in  $\mu$  direction (this corresponds to the absence of  $dI/d\mu$  term in (3.10)). The normal vectors for element  $\mathcal{Q}$  point outward toward neighboring elements  $\mathcal{B}$ ,  $\mathcal{C}$ ,  $\mathcal{D}$  and  $\mathcal{E}$ . The normals of the neighboring elements on the shared boundaries with  $\mathcal{Q}$  point in the opposite directions. For normal vectors, the subscripts denote the element for which the normal vector is defined and the superscripts show the coordinate and the direction that the normal is pointing to. For example,  $n_{\mathcal{Q}}^{\tilde{\varphi}^-}$  is the normal from element  $\mathcal{Q}$  to  $\mathcal{E}$  in the negative  $\tilde{\varphi}$  direction.

---

<sup>†</sup>Due to axisymmetry, the same expression is obtained for  $\varphi_s \neq 0$ .

The specific values of  $(n_r, n_{\tilde{\varphi}}, n_\mu)$  are shown in parentheses for the four faces of the element  $\mathcal{Q}$  that are in the  $r$ - $\tilde{\varphi}$  plane in Fig. 28. Specifically,  $(n_r, n_{\tilde{\varphi}}, n_\theta) = (\mp 1, 0, 0)$  for  $\partial\mathcal{Q}_r^\mp$  and  $(n_r, n_{\tilde{\varphi}}, n_\theta) = (0, \mp 1, 0)$  for  $\partial\mathcal{Q}_{\tilde{\varphi}}^\mp$ , respectively, and their corresponding  $\hat{\mathbf{s}} \cdot \mathbf{n}$  and residuals are,

$$\hat{\mathbf{s}} \cdot \mathbf{n} = \sin \theta \cos \tilde{\varphi} n_r \quad \Rightarrow \quad \mathcal{R}_{\partial\mathcal{Q}_r} = \sin \theta \cos \tilde{\varphi} n_r (I^* - I), \quad \text{on } \partial\mathcal{Q}_r^\mp \quad (3.14a)$$

$$\hat{\mathbf{s}} \cdot \mathbf{n} = -\sin \theta \sin \tilde{\varphi} n_{\tilde{\varphi}} \quad \Rightarrow \quad \mathcal{R}_{\partial\mathcal{Q}_{\tilde{\varphi}}} = -\sin \theta \sin \tilde{\varphi} n_{\tilde{\varphi}} (I^* - I), \quad \text{on } \partial\mathcal{Q}_{\tilde{\varphi}}^\mp \quad (3.14b)$$

The coordinates  $\tilde{\varphi}$  and  $\mu = \cos \theta$  at each point on these four boundaries determine the value of  $\hat{\mathbf{s}} \cdot \mathbf{n}$  in (3.14) and whether the residual is trivially zero for  $\hat{\mathbf{s}} \cdot \mathbf{n} \geq 0$ .

It is noted that while the boundary of  $\Omega$  in Fig. 27 includes  $r$ -,  $\tilde{\varphi}$ -, and  $\mu$ -normal surfaces, boundary conditions are only enforced on  $r$ -normal spatial boundaries of the domain at  $r = R_1$  and  $r = R_2$ , on the parts that are wave-inflow; the description of regions on  $r = R_1$  and  $r = R_2$  that are inflow is provided in §3.4.2. For  $\mu$ -normal boundaries, by default there are no boundary residuals, as for element facets at  $\mu = \pm 1$  we have  $n_r = n_{\tilde{\varphi}} = 0$ ; accordingly, the corresponding element boundary residual is zero from (3.13). Finally, for  $\tilde{\varphi}$ -normal facets,  $\mathcal{R}_{\partial\mathcal{Q}_{\tilde{\varphi}}} = 0$  in (3.14b) as  $\tilde{\varphi} = \pm\pi$  for these facets on the boundary of  $\Omega$ .

In this work, the unknown intensity in each element is expressed in terms of scaled coordinates  $r', \mu', \tilde{\varphi}'$ ,

$$\begin{aligned} r' &= \frac{r - m_r}{\Delta r} \\ \tilde{\varphi}' &= \frac{\tilde{\varphi} - m_{\tilde{\varphi}}}{\Delta \tilde{\varphi}} \\ \mu' &= \frac{\mu - m_\mu}{\Delta \mu} \end{aligned}$$

where  $m_r, m_{\tilde{\varphi}}$ , and  $m_\mu$  are the minimum values of the coordinates within the element and  $\Delta r, \Delta \tilde{\varphi}$ , and  $\Delta \mu$  the spans of a cubic element  $\mathcal{Q}$  in  $r, \tilde{\varphi}$ , and  $\mu$  directions, respectively. The use of scaled coordinates  $(r', \tilde{\varphi}', \mu') \in [0, 1]$  prevents ill-conditioning

problems that can arise if  $r$ ,  $\tilde{\varphi}$ , and  $\mu$  are directly used to interpolate the solution within elements.

The discrete solution for element  $\mathcal{Q}$ ,  $I_{\mathcal{Q}}^h$ , is interpolated by the tensorial product monomials of order  $p_r$ ,  $p_\mu$ , and  $p_{\tilde{\varphi}}$ , in  $r$ ,  $\mu$  and  $\tilde{\varphi}$ , respectively, and is given by,

$$I_{\mathcal{Q}}^h(r', \mu', \tilde{\varphi}') = \sum_{i=0}^{p_r} \sum_{j=0}^{p_{\tilde{\varphi}}} \sum_{k=0}^{p_\mu} a_{\mathcal{Q}}^{ijk} r'^i \tilde{\varphi}'^j \mu'^k, \quad (3.15)$$

where the coefficients  $a_{\mathcal{Q}}^{ijk}$  are the unknowns for element  $\mathcal{Q}$ . Note that  $I_{\mathcal{Q}}^h$  is zero outside the element  $\mathcal{Q}$ . In general, for example in the context of a  $p$ -adaptive scheme, each space-angle element  $\mathcal{Q}$  can have its distinct orders  $(p_r, p_{\tilde{\varphi}}, p_\mu)$ . However, this option is not practiced in the numerical studies presented in §3.5 and a constant polynomial order  $p := p_r = p_{\tilde{\varphi}} = p_\mu$  is used for all directions.

The discrete solution  $I^h$  is obtained by multiplying the interior residual (3.10) and boundary residual (3.11) by weight functions  $\hat{I}$  and integrating them over the interior and boundary of elements, respectively. The discrete form of this weighted residual statement for an arbitrary element  $\mathcal{Q} \in \Omega$  is,

$$\begin{aligned} \int_{\mathcal{Q}} \hat{I}_{\mathcal{Q}} \left( \sin \theta \cos \tilde{\varphi} \frac{\partial I_{\mathcal{Q}}^h}{\partial r} - \frac{\sin \theta \sin \tilde{\varphi}}{r} \frac{\partial I_{\mathcal{Q}}^h}{\partial \tilde{\varphi}} + \beta I_{\mathcal{Q}}^h - \kappa I_b - S(r, \mu, \tilde{\varphi}) \right. \\ \left. - \frac{\sigma_s}{4\pi} \int_{-\pi}^{\pi} \int_{-1}^1 I^h(r, \mu', \tilde{\varphi}') \Phi(\mu, \tilde{\varphi}, \mu', \tilde{\varphi}') d\mu' d\tilde{\varphi}' \right) r dr d\mu d\tilde{\varphi} \\ + \int_{\partial \mathcal{Q}_r} \hat{I}_{\mathcal{Q}} [\sin \theta \cos \tilde{\varphi} (I^* - I_{\mathcal{Q}}^h)] n_r r d\mu d\tilde{\varphi} \\ + \int_{\partial \mathcal{Q}_{\tilde{\varphi}}} \hat{I}_{\mathcal{Q}} [-\sin \theta \sin \tilde{\varphi} (I^* - I_{\mathcal{Q}}^h)] n_{\tilde{\varphi}} dr d\mu = 0. \quad (3.16) \end{aligned}$$

Since a Bubnov Galerkin method is used, the weight functions,  $\hat{I}_{\mathcal{Q}}$ , are taken from the basis functions of the discrete solution  $\hat{I}_{\mathcal{Q}}^h$ , equal to monomials  $r^i \mu^j \tilde{\varphi}^k$  for  $0 \leq i \leq p_r$ ,  $0 \leq j \leq p_{\tilde{\varphi}}$ , and  $0 \leq k \leq p_\mu$ , within the element  $\mathcal{Q}$  and zero outside. The global coupling between different angle ranges  $\mu \in (\mu_j, \mu_{j+1})$ ,  $j \in \{0, \dots, m-1\}$  and  $\tilde{\varphi} \in (\tilde{\varphi}_k, \tilde{\varphi}_{k+1})$ ,  $k \in \{0, \dots, l-1\}$  arises from the triple phase function integral

in (3.16) or boundary conditions, such as reflective boundary condition, that can couple all angles at  $r = R_1$  and  $r = R_2$ ; cf. (3.5).

## 3.4 Implementation

### 3.4.1 Discontinuous Galerkin implementation

The implementation of the RTE is based on a general purpose C++ software code for the solution of discontinuous Galerkin methods. This software was originally designed for the solution of *causal Spacetime Discontinuous Galerkin* (cSDG) methods for elastodynamics [5], advection-diffusion equation [93], and electromagnetics [7], just to name a few. The cSDG method directly discretizes space and time with simplicial elements that satisfy a special causality constraint. The weak enforcement of the jump conditions between interior and target fluxes on the boundaries of elements provides unique opportunities to model complex interface matching problems; see for example [134, 3, 135]. However, these facet terms require more general modeling of integration cells capable of integration of coincident interior and facets cells for interface problems [4], facet and cofacet neighborhood information, and computational geometry operations.

We have used the existing functionalities of the cSDG software for the implementation of general RTEs. Specifically, the support for coupling of space with other coordinates (time in aforementioned references) simplified the implementation of space-angle coupled elements. However, a major overhaul of the software and implementation of a new geometry library (GMeshing) was required to analyze space-angle elements used for the RTE. To implement general RTEs, the software supports the extrusion of a 1D to 3D spatial domain, discretized by simplicial elements, into arbitrary number of extrusions in angle or other coordinates. For example, in Fig. 27, 1D simplicial spatial elements (lines) on the left are extruded first to the 9 once-extruded simplicial elements (squares) in the  $r - \tilde{\varphi}$  plane and next to

twice-extruded simplicial elements (cubes) in  $\Omega$ . Some specific challenges with this implementation included setting neighborhood information (facets and cofacets in spatial and extrusion directions), formation and processing of integration cells, and computational geometry information of the extruded cells. Moreover, for angle integration terms in (3.3) and (3.5) additional neighborhood information between space-angle cells and their corresponding *base* spatial elements, *e.g.*, elements  $\mathcal{Q}$  and  $\mathcal{Q}_x$  in Fig. 27, and integration routines were required. The software architecture of GMeshing and this expanded finite element DG module are expected to be discussed in more detail in subsequent publications.

### 3.4.2 Method of characteristic

The method of characteristic is implemented in MATLAB and C++ to visualize the solution and compare the results with the DG method. The RTE formulation with or without angular integration terms (emission term and scattering term) can be modeled with this method. The forward and backward implementations of this method are discussed next.

#### Forward scheme

Characteristics corresponds to the path of radiation rays that go through the disk depicted in Fig. 25. According to (3.9), each characteristic is invariant to  $\mu$ . This implies that the characteristics remain in the  $r - \tilde{\varphi}$  plane and that the characteristic lines coincide for all  $r - \tilde{\varphi}$  planes at different  $\mu$  values. All of the characteristics starting at the inflow boundary on the inner wall eventually reach the outflow boundary on the outer wall. However, the characteristics starting at the outer wall end at either the inner wall or the outer wall. These inflow and outflow boundaries are shown by red and blue, respectively, in Fig. 29. This is because in a disk-like medium some inflow rays on the outer wall intersect the outer wall and some reach the inner wall.

To calculate the radiation intensity field, the domain is first discretized into  $N$   $r - \tilde{\varphi}$  planes for  $\mu_k \in \{\mu_1, \dots, \mu_N\}$ . The characteristic lines and other quantities on the  $k^{\text{th}}$   $r - \tilde{\varphi}$  plane are decorated with the left superscript  $k$ , corresponding to  $\mu_k$ . For example, the characteristic lines on the  $k^{\text{th}}$  plane are  ${}^k l_j$  for  $j \in \{1, 2, \dots, M\}$  where  $M$  is the number of characteristic lines considered on this plane and  $j$  is the index of characteristic line. As shown in Fig. 29, the characteristic lines start from points on the inflow boundaries of the domain, that is  $\tilde{\varphi} \in [-\pi/2, \pi/2]$  at  $r = R_1$  the inner wall and  $\tilde{\varphi} \in [-\pi - \pi/2] \cup [\pi/2, \pi]$  at  $r = R_2$  the outer wall. Finally, each characteristic line  ${}^k l_j$  is discretized into segments separated by points  ${}^k p_j^i$ , with  $i$  being the index of points on this line, as shown in the figure. Thus, the radiation intensity at the end of the segment point,  ${}^k p_j^{i+1}$ , along characteristic,  ${}^k l_j$ , is calculated by forward Euler scheme derived from (3.8),

$$|\mathbf{V}| \frac{{}^k I_j^{i+1} - {}^k I_j^i}{\Delta l} = {}^k \check{S}_j^i, \quad k \in \{1, \dots, N\}, j \in \{1, \dots, M\}, \quad (3.17)$$

where  ${}^k \check{S}_j^i$  is the source term at point  ${}^k p_j^{i+1}$  and  $\Delta l = \sqrt{\Delta r^2 + \Delta \tilde{\varphi}^2}$  is the distance of the points  ${}^k p_j^i$  and  ${}^k p_j^{i+1}$  with relative positions  $\Delta r$  and  $\Delta \tilde{\varphi}$  in  $r$  and  $\tilde{\varphi}$  directions, respectively. This ODE starts from initial condition  ${}^k I_j^0$  at the first point of characteristic  ${}^k l_j$  on the corresponding inflow boundary; *cf.* Fig. 29.

If angle coupling exists (with angular integration terms in (3.3)), an iterative method is needed to update the total source term,  ${}^k \check{S}_j^i$ . The trapezoidal rule is used to approximate the integrals over the angle at  ${}^k p_j^i$ . Since all characteristics overlap each other over  $\mu$  direction, no interpolation of solutions is needed in this direction and a trapezoidal rule is employed for angle integrations in  $\mu$  direction. For example, the two points  ${}^k p_j^i$  and  ${}^{k-1} p_j^i$  are shown for the integrals in  $\mu$  at  $p_j^i$  location in  $r - \tilde{\varphi}$  planes in Fig. 29. However, the solutions for solid angle integration along  $\tilde{\varphi}$  need to be interpolated from existing solutions at points  ${}^k p_j^i$ . A trapezoidal rule based on the interpolated solutions is used for the  $\tilde{\varphi}$  direction integrals. The iterations start with

an initial guess, *e.g.*, the solution with no angular integration, and continues until the intensity at all points converges.

### Backward scheme

A backward scheme is preferred if the solution is sought on a structured grid. The domain is discretized into a structured cube with points  ${}^k q_j^l = (r_i, \tilde{\varphi}_j, \mu_k)$ , where  $r_i \in \{r_0, r_1, \dots, r_M\}$ ,  $\tilde{\varphi}_j \in \{\tilde{\varphi}_0, \tilde{\varphi}_1, \dots, \tilde{\varphi}_L\}$ , and  $\mu_k \in \{\mu_0, \mu_1, \dots, \mu_N\}$ . Since the RTE is a linear differential equation, the path of a characteristic line passing through a point, both forward and backward, is independent of the solution of radiation intensity along its path. This is reflected in the independence of the increments of the characteristic path on solution  $I$  in (3.9). Accordingly, the backward path of a characteristic passing through a grid point  ${}^k q_j^l$ , shown in green in Fig. 29, can be determined by (3.9), without having the solution of radiation intensity along its path (shown in dashed line). Once the starting point on the inflow boundary of the domain, shown by  ${}^k \bar{q}_j^l$ , is determined, the initial condition along this determined characteristic path is obtained from the boundary condition. Next, a forward Euler integration scheme similar to (3.17) can be used to determine the solution at  ${}^k q_j^l$  from the boundary condition at  ${}^k \bar{q}_j^l$ . When angular integration terms in (3.3) are nonzero, an iterative solution scheme similar to that described in §3.4.2 is used; the initial solution (guess) corresponds to the solution with zero angle integral terms and at each iteration source term and radiation intensity are updated until the differences of radiation intensities of two successive solutions is below a user specified tolerance at all grid points.

The backward scheme has several advantages. First, the structured points  ${}^k \bar{q}_j^l$  can coincide with quadrature points of a DG method discretization. This enables the computation of the error between discrete DG solution and a solution represented by this backward method of characteristics. The latter solution can be considered as the (exact) reference solution as long as sufficiently small  $\Delta l$  is chosen for the integration of solution in (3.17). Second, since a structured grid is used in all directions, the points in  $\tilde{\varphi}$  direction also coincide; thus, unlike the forward scheme in §3.4.2 there

is no need to interpolate the solution in  $\tilde{\varphi}$  direction when angular integration terms are nonzero. Third, as will be discussed in §3.5.2, *cf.* Fig. 32, the characteristic lines are sparse in certain parts of the domain. Using a backward scheme ensures that the solution can be represented by uniform resolutions in all directions. However, it is noted that the backward scheme is more expensive as for each point, the solution along one characteristic is required. In contrast, in forward scheme, the solution along each characteristic line represents many solution points.

## 3.5 Numerical examples

In this section, the DG method is first verified for problems with exact smooth solutions; the MMS is used in §3.5.1 to first capture polynomial solutions that belong to discrete solution space and next obtain the convergence rate of the DG method. A furnace radiation problem for which closed form analytical solution does not exist is studied in §3.5.2. The method of characteristics is used to verify the DG method for this problem and demonstrate the form of characteristics for this axisymmetric RTE formulation. Finally, a blackbody emission problem and an anisotropic scattering problem are presented in §3.5.3.

### 3.5.1 Method of manufactured solution

The MMS is used to validate formulation and implementation of the DG RTE method. In the MMS, a function  $I^M$  is chosen to satisfy the RTE,

$$I(r, \mu, \tilde{\varphi}) = I^M(r, \mu, \tilde{\varphi}). \quad (3.18)$$

The source term in (3.3) is determined such that  $I^M$  satisfies this equation. Accordingly, source term, specifically denoted by  $S^M$  for the MMS, is obtained by

plugging (3.18) in the RTE to obtain,

$$\begin{aligned}
S^M &= \sin \theta \cos \tilde{\varphi} \frac{\partial I^M}{\partial r} - \frac{\sin \theta \sin \tilde{\varphi}}{r} \frac{\partial I^M}{\partial \tilde{\varphi}} + \beta I^M - \kappa I_b \\
&\quad - \frac{\sigma_s}{4\pi} \int_{-\pi}^{\pi} \int_{-1}^1 I^M(r, \mu', \tilde{\varphi}') \Phi(\mu, \tilde{\varphi}, \mu', \tilde{\varphi}') d\mu' d\tilde{\varphi}'. \tag{3.19}
\end{aligned}$$

Conversely, if the RTE problem is solved with the source term (3.19) and boundary conditions consistent with  $I^M$  on the inflow parts of the spatial boundary of domain at  $R_1$  and  $R_2$ , the function  $I^M$  is recovered as the exact solution of the RTE (3.3). In discrete setting, if the manufactured solution  $I^M$  belongs to the space of finite element solution, *i.e.*, when it is a polynomial of order equal or less than that used to interpolate  $I^h$  in (3.15), the exact solution  $I^M$  is recovered. Otherwise,  $I^h$  asymptotically converges to  $I^M$  as finer meshes ( $h$ -refinement) or higher order polynomials for  $I^h$  ( $p$ -enrichment) are used. The former and latter cases are applied for problems in §3.5.1 and §3.5.1, respectively.

### Validation study for polynomial exact solutions

Two cases are conducted for validating the formulation and implementation in an annulus with inner and outer radii of  $R_1 = 1$  and  $R_2 = 2$ , respectively. In the first case, the MS solution  $I^M$  is given as a second order polynomial in both space and angle,

$$I^M(r, \mu, \tilde{\varphi}) = r^2 \mu^2 + r^2 \tilde{\varphi}^2 - r \mu^2 - r \tilde{\varphi}^2 + \mu^2 \tilde{\varphi}^2 + \mu \tilde{\varphi} + \frac{1}{2} \tilde{\varphi}^2. \tag{3.20}$$

The phase function  $\Phi$  and black-body radiation  $I_b$  are equal to zero. The DG method recovers the exact solution to within machine precision. Several contour plots of the solution in  $r - \tilde{\varphi}$  planes are shown in Fig. 30. In the second case, the MS solution  $I^M$  remains the same as in the first case in (3.20). The black-body radiation  $I_b = (1/4\pi) \oint_{4\pi} I ds'$  is assumed at radiative equilibrium; *cf.* (3.2). The phase function is set to  $\Phi = 1$  for an isotropic scattering. Again, the DG method recovers the exact solution to within machine precision.

## Convergence study

The following harmonic function is used as the manufactured solution to perform a convergence study for the proposed DG method,

$$I^M(r, \mu, \tilde{\varphi}) = \sin(\pi r) \sin(\pi \mu) \sin(\pi \tilde{\varphi}). \quad (3.21)$$

The L2 norm of the point-wise error  $\varepsilon$  between the discrete and manufactured solution is used to characterize the numerical error,

$$\text{Point-wise error :} \quad \varepsilon(r, \mu, \tilde{\varphi}) = I^h(r, \mu, \tilde{\varphi}) - I^M(r, \mu, \tilde{\varphi}), \quad (3.22a)$$

$$\text{L2 norm of error :} \quad L_2(\varepsilon) = \sqrt{\int_{\Omega} |\varepsilon|^2 d\Omega}. \quad (3.22b)$$

Since polynomials are used for the discrete solution in (3.15),  $I^h$  cannot exactly represent the manufactured solution (3.21) and the numerical error is nonzero for all element sizes and polynomial orders. The spatial domain corresponds to an annulus with inner and outer radii of  $R_1 = 1$  and  $R_2 = 2$ , respectively. The coarsest mesh used for convergence study contains four elements in space, corresponding to uniform element size of  $h = (R_2 - R_1)/4 = 0.25$ . In angle directions, this mesh contains four elements in  $\tilde{\varphi}$  and  $\mu$  directions, corresponding to inter-element values of  $\tilde{\varphi} \in \{-\pi, -\pi/2, 0, \pi/2, \pi\}$  and  $\mu \in \{-1, -0.5, 0, 0.5, 1\}$ , respectively. For convergence analysis this mesh is uniformly refined in all directions by factors of 2. For example, for the next coarsest mesh  $h = 0.125$  and 8 elements are used in each angle direction. Uniform space and angle polynomial orders of  $p = 0$  to  $p = 3$  are used for the analysis. The convergence rate of the discrete solution is obtained by determining the slope  $\beta_p$  of the logarithm of L2 norm of error  $L_2(\varepsilon)$  versus the logarithm of the element size  $h$ . As shown in Fig. 31, the asymptotic convergence rate of  $\beta_p = p + 1$  is achieved for polynomial order  $p$  as  $h \rightarrow 0$ .

### 3.5.2 Verification of the DG method with the method of characteristics

A practical problem of radiation in an annular furnace with inner and outer radii of  $R_1 = 1$  and  $R_2 = 2$  is considered with inflow boundary conditions  $I(R_1) = I(R_2) = 1$ . There are no angular coupling integrals in (3.3) as  $\kappa = 0$  and  $\sigma_s = 0$ . The extinction coefficient is  $\beta = 0.01$ . Since this problem does not have a closed-form exact solution, the method of characteristics is used to verify the DG solution.

For the method of characteristic, it is worth mentioning that a sparse zone exists along  $\tilde{\varphi} = \pm\frac{1}{2}\pi$ . While in this case 200 characteristic lines are used in each  $r - \tilde{\varphi}$  plane, the solution points are still very sparse in the regions shown in Fig. 32. To better show this sparsity and noting the symmetry of the solution with respect to  $\tilde{\varphi} = 0$  plane, the solution  $I$  is only shown on the top half of the domain. As done for the next results, one can simply increase the number of characteristics lines to reduce the sparsity. However, for comparison of the two methods, it is noted that the DG method does not have this issue, since the solution is interpolated by polynomials over the entire space-angle domain.

The results for both methods are shown in Fig. 33 in sliced  $r - \tilde{\varphi}$  planes for  $\mu = -0.5, 0, 0.5$ . These planes are chosen since characteristic lines stay in them. For the method of characteristics,  $\Delta l = 0.01$  and 2000 characteristic lines are used in each  $r - z$  plane to generate the plots; *cf.* §3.3.2 and §3.4.2. As shown in Fig. 33a, there are two lines of strong discontinuity in  $I$  that coincide for all values of  $\mu$ . The distance between these lines decreases and the discontinuity jump increases as  $r$  increases toward  $R_2 = 2$ . As shown in Fig. 33b, the DG method is capable to accurately capture this discontinuity without much numerical oscillations around these lines with a moderately refined mesh of  $32 \times 32 \times 32$  elements and  $p = 3$ . It is emphasized that one main advantage of DG methods over continuous finite element methods is their superior performance for problems with jumps and high gradient solutions features. Due to the structure of characteristic lines, such jumps

in the solution are common for the axisymmetric RTE. This example demonstrates the advantage of using a DG method for this RTE formulation.

To compare the results of the DG method and the method of characteristics, a convergence study is performed in terms of the L2 error norm between the two solutions. That is, the high resolution solution of the method of characteristics plays the role of exact solution  $I^M$  in (3.22). The convergence rate of  $\beta_p \approx 0.4$  is not improved by increasing the polynomial order. The limit in the convergence rate of the solution is due to the strong discontinuity lines that pass through finite elements.

### 3.5.3 Benchmark problems between two concentric cylinders

#### Blackbody emission

The problem of a gray gas at radiative equilibrium between two concentric cylinders with infinite height is conducted and compared with the numerical results by Loyalka [86] which are accurate enough to be considered as the benchmark solution [88]. The ratio of inner and outer radii of the walls takes the values  $R_1/R_2 = 0.1, 0.5, 0.9$ . Moreover, the optical thickness,  $\tau = \int_0^r \beta(r)dr$ , also changes in different cases by changing the extinction coefficient  $\beta$ . The inner surface is hot ( $T_1 = 2000K$ ) and highly reflective ( $\epsilon_1 = 0.1$ ); the outer surface is relatively cool ( $T_2 = 400K$ ) and is a strong absorber ( $\epsilon_2 = 0.9$ ). Inside the concentric cylinder, the medium is gray and non-scattering ( $\sigma_s = 0$ ).

The nondimensional radiative heat transfer,  $\Psi$ , is defined as [86],

$$\Psi = \frac{q(\tau_1)}{J_1 - J_2}, \quad (3.23)$$

where  $q(\tau_1)$  is the radiative flux density at  $r = R_1$  ( $\tau = \tau_1$ ). The radiative flux density at radius  $r$  is obtained by the inner product of the surface normal  $\mathbf{n}_x$  and heat flux

vector  $\mathbf{q}(r)$ ,

$$q(r) = \mathbf{q}(r) \cdot \mathbf{n}_x, \quad \text{where} \quad \mathbf{q}(r) = \oint_{4\pi} I(\mathbf{r}, \hat{\mathbf{s}}) \hat{\mathbf{s}} ds'. \quad (3.24)$$

Since only inner surface is concerned, the surface normal  $\mathbf{n}_x = (-1, 0, 0)$  is used for  $r = R_1$  in  $(e_r, e_{\varphi_x}, e_z)$  coordinate system; *cf.* Fig. 25.

The values  $J_1$  and  $J_2$  are the radiosity of the walls at radii  $R_1$  and  $R_2$ , respectively. They account for non-black emission and diffuse reflection. For wall  $w \in \{1, 2\}$ ,  $J_w$  has the relation with net radiative flux  $q_w = q(R_w)$  [86],

$$q_w = \frac{\epsilon_w}{1 - \epsilon_w} (\pi I_{bw} - J_w), \quad (3.25)$$

where the black-body radiation at wall  $w$ , denoted by  $I_{bw}$ , is obtained from (3.2). Since  $q_w$  and  $I_{bw}$  are computed from the solution to RTE and  $\epsilon_w$  is the emissivity of wall  $w$ ,  $J_w$  can be obtained from (3.25). Once  $J_1$  and  $J_2$  are obtained,  $\Psi$  is computed from (3.23).

A  $16 \times 16 \times 16$  grid with polynomial order  $p = 1$  is used for DG solutions. As shown in Fig. 35, the DG results agree well with the numerical results by Loyalka [86]. It is observed that the nondimensional radiative heat transfer decreases with the increase of the optical thickness as well as the increase of the radius ratio. The effect of the radius ratio can be attributed to the fact that as  $R_1/R_2 \rightarrow 0$  less energy is reflected from the inner boundary and most of the energy exits from the outer boundary. It is noticed that the difference between DG and reference solution is slightly larger for thinner optical thicknesses and the difference has overall lower values for smaller  $R_1/R_2$  ratios. This may be attributed to numerical integration errors and other approximations involved in the solution method employed in [86].

Comparing to the previous example in Fig. 33b, where strong discontinuity is inside the domain along the characteristic lines  $r \sin \tilde{\varphi} = \pm 1$ , the results with diffuse reflection on boundaries and emission in the domain seem much smoother; this is

shown in Fig. 36 for a particular case of  $R_1/R_2 = 0.5$  and  $\tau_2 - \tau_1 = 10$ . In general, the angle integrations through scattering and black-body radiation terms, as well as emissive and diffusive terms on the boundary of domain in (3.5), smoothen the solution around the characteristic jump lines in Fig. 33b. These angle integral terms improve the accuracy and order of convergence of the DG method.

### Anisotropic scattering

In this case, the enclosure of two infinite concentric cylinders with radii of  $R_1 = 1$  and  $R_2 = 2$  contains an anisotropic scattering medium with the cold inner wall with  $I(R_1) = 0$  and isotropic incidence on outer wall with  $I(R_2) = 1$ . The extinction, absorption, and scattering coefficients are  $\beta = 0.1$ ,  $\kappa = 0$ , and  $\sigma_s = 0.05$ , respectively. The Rayleigh scattering is used, where phase function  $\Phi(\mu, \tilde{\varphi}, \mu', \tilde{\varphi}')$  is given,

$$\Phi(\mu, \tilde{\varphi}, \mu', \tilde{\varphi}') = \frac{3}{4} \left\{ 1 + \left[ \sqrt{(1 - \mu^2)(1 - \mu'^2)} \cos(\tilde{\varphi} - \tilde{\varphi}') + \mu\mu' \right]^2 \right\}. \quad (3.26)$$

A  $64 \times 64 \times 64$  grid with polynomial order  $p = 2$  is used for DG solutions, whereas, a  $201 \times 201 \times 201$  structured grid with  $\Delta l = 0.01$  is used for the backward iterative method of the method of characteristics; *cf.* §3.4.2. It took the iterative method 221 steps to converge to  $1 \times 10^{-12}$  relative error, which is quite inefficient. The results for both methods, as shown in Fig. 37a, indicate a strong discontinuity which is similar to the results in §3.5.2. Again, the DG method accurately captures the discontinuity without much numerical oscillations along the jumps, with coarser grid compared to the method of characteristics. Fig. 37b shows the results of the difference between the solutions with anisotropic scattering and the solutions without scattering, *i.e.*,  $\sigma_s = 0$  for the two methods. It provides a better perspective of how the medium scatters the radiation energy. As shown, strong scattering is observed near the outflow outer boundary where rays intersect with the outer wall. Moreover, the backward scattering is weaker from the outer wall towards the inner wall.

## 3.6 Discussion and conclusions

A discontinuous Galerkin method for the solution of steady state radiative heat transfer between concentric cylinders, described by the one-dimensional RTE in cylindrical coordinates, was presented. The application of the discontinuous Galerkin method is described for problems in which radiation intensity varies over one dimension in space and two dimensions in angles. In this application, the RTE is spontaneously discretized over the space and angle by the DG method.

To discretize the angular directions, the spatial elements are extruded in two angular directions. This allows the basis function to be high order not only in space but also in angle. This aspect improves the convergence rate as shown in §3.5.1 and [27], compared to the hybrid methods that are capable of changing the order of accuracy only in space, such as hybrid ( $S_N$ ) FEM [108, 1, 98, 105], ( $S_N$ ) DG method [84, 139, 58, 45, 33, 133], and other hybrid methods [50, 51, 34, 35] which use a piece-wise constant or a delta function in angle. Specific to this RTE formulation, the discretization of the  $dI/d\tilde{\varphi}$  term in (3.3) with finite difference in discrete ordinate method poses new implementation challenges and introduces additional discretization errors. For the DG formulation, the RTE is fully discretized in space and angle, so no additional scheme is needed to model this derivative term.

The use of DG formulation has several advantages. First, similar to continuous FEMs complex spatial geometries can be modeled with arbitrarily high order of accuracy in space. Second, inter-element continuity constraint is enforced weakly using the target flux  $I^*$ . In contrast, for the RTE formulation presented herein, a continuous space-angle FEM formulation would enforce a continuity constraint along the  $\mu$  direction. This continuity condition is nonphysical when there are no angle-integration terms in (3.1) and (3.5). Moreover, the use of upstream values for  $I^*$  results in very accurate representation of solution, consistent with the characteristic structure of problem; as discussed DG methods have a superior performance to continuous FEMs in capturing jumps in solution, such as those observed in  $r-\tilde{\varphi}$  planes

in Fig. 33. Third, a major advantage of DG methods is the increased flexibility in both  $h$  and  $p$  adaptive schemes, where the size and order of the elements can change suddenly without the need to use transition elements used in FEMs. We plan to extend the novel adaptive operations proposed in [6] from space and spacetime to the space-angle RTE problem. Fourth, as discussed in detail in [27], while both DG in angle and spherical harmonic method can achieve arbitrary high order of accuracy in angle, the former has a better performance for problems with concentrated point or line sources.

Several numerical examples were presented for this DG formulation. The convergence study was conducted for both smooth and discontinuous solutions. While for the latter, the convergence rate is relatively poor as shown in Fig. 34, the space-angle DG method is still able to accurately capture discontinuities in the solution in  $r - \tilde{\varphi}$  planes. Moreover, the benchmark problem from [86] shows the high accuracy of the DG method for different optical thicknesses and ratios of the inner to outer radii. The last problem shows that the DG has a good flexibility for solving the RTE with complex properties, *e.g.*, scattering in an anisotropic medium.

In order to verify the results by the DG solver, the method of characteristic is employed for the one-dimensional cylindrical RTE. The method of characteristic performs much better, especially, with respect to the strong discontinuity, since the intensity is calculated along the corresponding characteristics without jumps involved. However, its lack of complexity in geometry (boundary condition particularly) and the low iteration convergence rate when having the angular integration term make the scheme limited. Although the transition region at the discontinuity is inevitable for the DG method, for example in Fig. 37, where continuity of the solution in each element is required, other mesh-based methods such as continuous FEMs can suffer even worse numerical oscillations [43]. In the previous work [27], it was demonstrated that having both the discontinuous property between elements and the capability of high order accuracy makes the space-angle DG method outstanding for solving the

RTE. One extension to this work is to apply the  $h$ - and  $hp$ -adaptive mesh scheme to mitigate the transition region as much as possible.

Another important extension to this work is the formulation of an iterative solution of the RTE when angular integration terms are present. In this case, the system stiffness matrix is very dense and even for moderate resolutions of the grid in space and angle, this matrix may not fit in computer RAM memory. We are currently working on an iterative scheme that each time only one slab of the domain in  $r - \tilde{\varphi}$  plane is solved. This would enable solving the problem in §3.5.3 with much higher resolutions.

## Chapter 4

### Iterative Space-Angle

### Discontinuous Galerkin Method for Radiative Transfer Equation

## 4.1 Abstract

The radiative transfer equation (RTE) is an integro-differential equation that describes the radiation energy absorbing, emitting, and scattering in both space and angle, which can be up to five-dimensional problems. It is difficult for an RTE solver to satisfy both accuracy and efficiency (less computational resources) for such high-dimensional problems. In this paper, an iterative solver for one-dimensional cylindrical radiative transfer problems using the space-angle discontinuous Galerkin (DG) method is developed to achieve both accuracy and efficiency. The iterative solver is based on the angular decomposition (AD) method, which slices the spatial-angular domain into slabs and decouples the angular integration between slabs. Both Gauss-Seidel (GS) and successive over-relaxation (SOR) iterative methods are investigated by numerical analysis and examples. The comparison of the two iterative methods suggests that an appropriate relaxation factor for the SOR method may accelerate the convergence. Finally, the iterative method is more efficient than the direct solution of the system both in terms of memory usage and computational time, especially for finer meshes.

## 4.2 Introduction

Radiative transfer takes place in a wide range of natural phenomena and engineering applications. The propagation of radiation in the form of electromagnetic waves through a medium is affected by absorption, emission, and scattering processes. The radiative transfer equation (RTE) mathematically describes such processes and heat transfer, neutron transport, atmospheric science, optical molecular imaging are a few areas of its application [109]. In the steady state, the RTE is an integro-differential equation of up to five independent variables, which are 3 dimensions in space and 2 directions of the solid angle. The high dimensionality and the integral term present serious challenges when trying to solve the RTE numerically. The discontinuous

Galerkin (DG) finite element method (FEM), introduced by Reed and Hill [100], is one of the most popular grid-based numerical methods for solving the RTE due to its high order accuracy and flexibility in mesh grids. The basis functions used in the DG method are discontinuous across element interfaces; accordingly, the jump condition between interior traces of solution and the so-called numerical flux is weakly enforced on the interface boundaries. The space-angle DG method is specially suitable for the RTE, since the evolution of solution along characteristics can be strongly discontinuous in both space and angle [88]. However, the direct solution of the linear system formed by the DG formulation can be quite expensive.

*Discrete ordinates method* (DOM), also known as  $S_N$  method, is a common approach to discretize the angle domain by using a quadrature method for the integrations in solid angles. The spatial dependence in the RTE is discretized by the numerical methods mentioned above. Thus, the RTE and its corresponding boundary conditions are transformed into a set of *Partial Differential Equations* (PDEs) only in terms of the spatial coordinates. Two drawbacks of the classical  $S_N$  method are known as *false scattering* and the *ray-effect* [17] that are mainly caused by the form of angular discretization [23]. In addition, when reflective boundaries are present, the performance of the  $S_N$  may not be satisfactory [102]; if a beam on the specular reflective boundary does not coincide with any discrete ordinate, the intensity of the specularly reflected beam is missed in the absent directions. Besides, special methods are needed in the DOM for coping with the angular derivative terms in the RTE in curvilinear coordinates [104]; that is, the angular redistribution [81] makes it difficult to handle the angular derivative terms in the RTE. The spherical harmonic method involves multiplying the RTE by various powers of direction cosines of the intensity, known as spherical harmonics [109]. Due to spectral nature of spherical function approximation, the discrete implementation of the RTE has super convergence properties in angle for sufficiently smooth solutions. Moreover, due to orthogonality of spherical harmonics the solutions for different spherical harmonics can be obtained independently for a nonscattering medium.

*Discontinuous Galerkin* (DG) methods [127, 97, 72, 26] are another family of methods used for the discretization of space and/or angle directions. The DG discretization of solution in space can be combined with different discretization methods in angle. Some examples are  $S_N$  [133, 33] and  $P_N$  [75, 111] angle discretizations. We have used DG discretization in both space and angle in [26, 119]. DG discretization in angle has at least two advantages to  $P_N$  method for certain problems. First, if the underlying exact solution is not smooth enough, the superconvergence property of the  $P_N$  method no longer holds as shown in [57] and [111]. This is the case for many RTE solutions, for example those in cylindrical axisymmetric setting [119]. Second, high accuracy may be required only in a narrow band of angles for example for concentrated incident wave or source terms. Due to discrete nature of the solution, DG methods are ideal for local refinement of the solution around the angles of interest.

For RTE problems with nonzero angle integration terms, *i.e.*, with nonzero scattering coefficient or reflective boundary conditions, the global system matrix that arises from numerical discretization of the all aforementioned methods can be quite large. When  $S_N$  or  $P_N$  methods are used, the otherwise independent solutions for different angles or spherical harmonics become coupled. For example, for the cylindrical axisymmetric problems considered herein, instead of solving a number of 1D problems in space, a space-angle three dimensional coupled problem needs to be solved. If the number of unknowns in angle is high, for example a space-angle DG discretization with high angle order or element count, the direct solution of these systems can result in high CPU times and memory usage.

Iteration methods can alleviate the issues pertained to solving such high dimensional problems to some extent. There are many existing methods such as Jacobi, Richardson, and generalized minimal residual (GMRES) [40] methods to iteratively solve a linear system. One approach that will be the most relevant to this paper is to split the global matrix  $\mathbf{K}$  into two matrices  $\mathbf{A}$  and  $\mathbf{B}$ . Some examples of these methods are Jacobi and Gauss-Seidel methods [80, 70], where  $\mathbf{A}$  is diagonal part for

the former one and diagonal and lower part for the latter one. As it will become evident, this class of methods is related to how the source iteration is used for the solution of RTEs with scattering.

For the RTE, the source iteration [38] is to decouple scattering and transport, and to exploit that the transport part can be inverted efficiently. The scattering part is treated as the source term with an initial guess and taken to the right-hand side of the linear equation. This approach resembles Gauss-Seidel (GS) iteration where only the block diagonals  $\mathbf{A}$  (transport part) is maintained in the part of the global matrix  $\mathbf{K}$  that is explicitly formed. Since the transport part is inverted explicitly, this method converges very fast for transport dominant problems. However, in the case of scattering dominance, this method converges more slowly. Besides the above iterative methods, the *successive over-relaxation* (SOR) method is a good alternative to the usual source iteration method as it can accelerate the convergence [76]. An optimal relaxation parameter in the SOR method can tremendously expedite the iteration. However, finding the optimal relaxation parameter is not straightforward and can be expensive.

In this paper, the angular decomposition (AD) method is introduced and associated with two different iterative methods to numerically solve the RTE iteratively. The formulation of the DG method is presented in §4.3. The AD method, and its combination with the GS and the SOR iterative methods are described in §4.4.1. Next, a series of numerical examples are conducted in §4.5 to compare the efficiencies of the iterative solvers and the direct solver.

### 4.3 Discontinuous Galerkin formulation of RTE

The general form of steady-state RTE for a gray medium is given as,

$$\frac{dI(\mathbf{x}, \hat{\mathbf{s}})}{ds} = -\beta I(\mathbf{x}, \hat{\mathbf{s}}) + \kappa I_b(\mathbf{x}) + \frac{\sigma_s}{4\pi} \oint_{4\pi} I(\mathbf{x}, \hat{\mathbf{s}}') \Phi(\hat{\mathbf{s}}, \hat{\mathbf{s}}') ds'. \quad (4.1)$$

This equation describes the change of radiation intensity  $I(\mathbf{x}, \hat{\mathbf{s}})$  at spatial location  $\mathbf{x}$  along the path  $ds$  in the angle space with angle coordinate  $\hat{\mathbf{s}}$ . The values  $\beta$ ,  $\kappa$ , and  $\sigma_s$ , are the spatial-dependent extinction, absorption, and scattering coefficients, respectively. The anisotropic scattering phase function is represented by  $\Phi(\hat{\mathbf{s}}, \hat{\mathbf{s}}')$  and  $\mathbf{s}'$  is the solid angle for phase function integral. The solid angle differential for  $\mathbf{s}'$  is denoted by  $ds'$ . The spatial-dependent total black-body radiation intensity is given by  $I_b$ . For problems in different dimensions or different coordinate systems, the left hand side term of Eqn. 4.1,  $dI(\mathbf{x}, \hat{\mathbf{s}})/ds$ , is different.

Our space-angle DG implementation of (4.1) supports 1D to 3D spatial domains, discretized by simplicial elements, and arbitrary number of angles that are represented by extrusion of spatial elements in angle directions. In this paper, we use the space-angle DG formulation for 1D cylindrical symmetric problems [119] to study the performance of the proposed iterative methods in Section 4.4. Figure 38 illustrates how the space-angle mesh is generated for a 1D spatial mesh extruded in two angular directions for this problem. This particular RTE formulation is chosen due to interesting inter-element couplings that occur in one of the angle directions. The 1D simplicial spatial elements (lines) on the left are extruded first to the 9 once-extruded simplicial elements (squares) in the  $r - \tilde{\varphi}$  plane and next to twice-extruded simplicial elements (cubes) in  $\Omega$ . This grid can correspond to a steady-state RTE in 1D cylindrical coordinate, whose specific expression of (4.1) is,

$$\begin{aligned} & \sin \theta \cos \tilde{\varphi} \frac{\partial I(r, \mu, \tilde{\varphi})}{\partial r} - \frac{\sin \theta \sin \tilde{\varphi}}{r} \frac{\partial I(r, \mu, \tilde{\varphi})}{\partial \tilde{\varphi}} \\ &= -\beta I(r, \mu, \tilde{\varphi}) + \kappa I_b(r) + \frac{\sigma_s}{4\pi} \int_{-\pi}^{\pi} \int_{-1}^1 I(r, \mu', \tilde{\varphi}') \Phi(\mu, \tilde{\varphi}, \mu', \tilde{\varphi}') d\mu' d\tilde{\varphi}' + S(r, \mu, \tilde{\varphi}), \end{aligned} \quad (4.2)$$

where  $(\mu, \tilde{\varphi})$  represents the coordinates in the angular domain. The above RTE can then be discretized over a space-angle finite element domain.

In a DG formulation, residuals (errors) must be specified both in the interior and on the boundary of elements. The weighted residual (WR) statement for a space-angle

region  $\mathcal{Q}$  is formed by multiplying the RTE (equation 4.1) by the weight function  $\hat{I}$  and adding the corresponding weighted residuals on the boundary of the element,

$$\int_{\mathcal{Q}} \hat{I} \left[ \frac{dI(\mathbf{x}, \hat{\mathbf{s}})}{ds} + \beta I(\mathbf{x}, \hat{\mathbf{s}}) - \kappa I_b(\mathbf{x}) \right] dV - \int_{\mathcal{Q}} \hat{I} \left[ \frac{\sigma_s}{4\pi} \oint_{4\pi} I(\mathbf{x}, \hat{\mathbf{s}}') \Phi(\hat{\mathbf{s}}, \hat{\mathbf{s}}') ds' \right] dV + \int_{\partial\mathcal{Q}} \hat{I} (I^* - I) \hat{\mathbf{s}} \cdot \mathbf{n} dA = 0 \quad (4.3)$$

where  $\partial\mathcal{Q}$  is the boundary of  $\mathcal{Q}$  and  $\mathbf{n}$  is the spatial normal vector on  $\partial\mathcal{Q}$ . In discrete setting,  $\mathcal{Q}$  represents a space-angle element as shown in Figure 38 and the intensity  $I$  is replaced by its discrete approximation in  $\mathcal{Q}$ ,  $I_{\mathcal{Q}}^h = \mathbf{H}_{\mathcal{Q}} \cdot \mathbf{a}_{\mathcal{Q}}$ , where  $\mathbf{H}_{\mathcal{Q}}$  is the tensorial product basis function formed by the monomials within element  $\mathcal{Q}$  and  $\mathbf{a}_{\mathcal{Q}}$  is the unknown vector for element  $\mathcal{Q}$ . Moreover, any of the basis functions can be used for the weight function  $\hat{I}$ ; that is,  $\hat{I} = \hat{\mathbf{H}}$  in discrete setting. The term  $(I^* - I) \hat{\mathbf{s}} \cdot \mathbf{n}$  is the jump condition which weakly enforces the continuity between each element.

For this RTE, the derivative  $dI(\mathbf{x}, \hat{\mathbf{s}})/ds$  involves derivatives in the angle direction  $\tilde{\varphi}$ . As a result, the term  $(I^* - I)n$  is active not only on element boundaries with spatial normal, but also those with normals along  $\tilde{\varphi}$  direction. Figure 39 shows the neighbors of an element in  $r - \tilde{\varphi}$  plane. Along  $r$  and  $\tilde{\varphi}$  normal planes  $(I^* - I)n$  takes specific forms. For more information on the space-angle DG formulation of 1D cylindrical coordinate, we refer the readers to *cf.* [119]. Using the RTE in cylindrical coordinate and the specific forms of jump terms on  $\partial\mathcal{Q}$ , equation (4.3) is expressed as,

$$\begin{aligned} \int_{\mathcal{Q}} \hat{\mathbf{H}} \left( \sin\theta \cos\tilde{\varphi} \frac{\partial I_{\mathcal{Q}}^h}{\partial r} - \frac{\sin\theta \sin\tilde{\varphi}}{r} \frac{\partial I_{\mathcal{Q}}^h}{\partial \tilde{\varphi}} + \beta I_{\mathcal{Q}}^h - \kappa I_b - S(r, \mu, \tilde{\varphi}) \right. \\ \left. - \frac{\sigma_s}{4\pi} \int_{-\pi}^{\pi} \int_{-1}^1 I^h(r, \mu', \tilde{\varphi}') \Phi(\mu, \tilde{\varphi}, \mu', \tilde{\varphi}') d\mu' d\tilde{\varphi}' \right) r dr d\mu d\tilde{\varphi} \\ + \int_{\partial\mathcal{Q}_r} \hat{\mathbf{H}} [\sin\theta \cos\tilde{\varphi} (I^* - I_{\mathcal{Q}}^h)] n_r r d\mu d\tilde{\varphi} \\ + \int_{\partial\mathcal{Q}_{\tilde{\varphi}}} \hat{\mathbf{H}} [-\sin\theta \sin\tilde{\varphi} (I^* - I_{\mathcal{Q}}^h)] n_{\tilde{\varphi}} dr d\mu = 0. \quad (4.4) \end{aligned}$$

Equation above is enforced for all elements  $\mathcal{Q}$  in the entire space-angle domain  $\Omega$ . Elements are coupled through  $I^*$  terms in the  $r - \tilde{\varphi}$  plane and the phase integral in angle directions  $\mu$  and  $\tilde{\varphi}$ . This results in a global linear system of equations,

$$\mathbf{K}\mathbf{a} = \mathbf{F}. \quad (4.5)$$

where  $\mathbf{a}$  is the global unknown vector formed from individual element unknowns  $\mathbf{a}_{\mathcal{Q}}$ ,  $\mathbf{K}$  is the *stiffness matrix*, and  $\mathbf{F}$  is the force vector comprising the terms that are independent of element unknowns  $\mathbf{a}$ .

## 4.4 iterative methods and angular decomposition

Directly solving the system requires dealing with a large stiffness especially for the multi-dimensional RTEs with the angular integral term. In the AD method, the space-angle domain is sliced along the angle direction and divided into several slabs. Subsequently, each slab can be solved separately. In this section, the GS and SOR iterative methods are formulated in conjunction with the AD scheme. The relaxation factor provided by the SOR method is discussed.

### 4.4.1 Angular decomposition

There are two types of coupling between elements, in general: a) the coupling through  $I^* - I$  term; b) the angular integration coupling. For the first one, the coupling is generally in space boundaries of the space-angle element. But in the case of curvilinear coordinate or when refractive index gradually changes in space-angle, the coupling can also be through angle boundaries of element. The 1D cylindrical RTE has a numerical flux in the azimuthal angle direction  $\tilde{\varphi}$  measured from the local radial direction; that is,  $\tilde{\varphi} = \varphi_s - \varphi_x$ . The spatial coordinates  $\varphi_x$  is removed due to invariance along the axis of symmetry, and angular symmetry of the problem (enabling the use of  $\tilde{\varphi}$  instead of two coordinates  $\varphi_c$  and  $\varphi_x$ ). In this case, the whole space-angle domain can

be sliced into slabs along the directions that have no *numerical fluxes* ( $I^* - I$  term) on the element boundaries that form the exterior boundary of the slab. Figure 38b) illustrates how each slab is formed after the base elements are extruded. Different colors represent different slabs. The slabs are coupled only through angle integration terms such as the phase function integration inside the domain and diffuse or specular reflective interface conditions. The angular integration terms can be divided into those within a slab and those that couple distinct slabs. The angle integration terms make the stiffness matrix dense. Accordingly, forming and storing the entire stiffness matrix can be computationally expensive and require extensive memory resources as the system size increases. The AD scheme drastically reduces the memory use.

An example of a  $4 \times 4 \times 4$  space-angle mesh (a) and its stiffness pattern (b) are depicted in Figure 40 for the discussion of such couplings. The elements are numbered as  $\mathcal{A}_{i,j}$ ,  $\mathcal{B}_{i,j}$ ,  $\mathcal{C}_{i,j}$  and  $\mathcal{D}_{i,j}$ , where the spatial elements are denoted by the letters  $\mathcal{A}$ ,  $\mathcal{B}$ ,  $\mathcal{C}$ , and  $\mathcal{D}$ , the subscripts  $i$  and  $j$  represent the numbering in  $\tilde{\varphi}$  and  $\mu$  directions, respectively. For example,  $\mathcal{D}_{3,1}$  is the green element in Figure 40(a) which is fourth in  $r$ , third in  $\mu$ , and first in  $\tilde{\varphi}$ . Each dot in the stiffness pattern represents a space-angle element. The coupling through  $I^* - I$  term in space can be seen in the matrix at the off block-diagonal entries. For instance, the dot at (1, 5) is the coupling between element  $\mathcal{A}_{1,1}$  and  $\mathcal{B}_{1,1}$ . The coupling through  $I^* - I$  term in  $\tilde{\varphi}$  is overlapped with the angle coupling in  $\tilde{\varphi}$ . Four cases of the latter couplings are shown through matrices  $\mathcal{A}_{2,\tilde{\varphi}}$ ,  $\mathcal{B}_{2,\tilde{\varphi}}$ ,  $\mathcal{C}_{2,\tilde{\varphi}}$  and  $\mathcal{D}_{2,\tilde{\varphi}}$  for the second layer of elements and all layers  $i$  in  $\tilde{\varphi}$ , that is couplings between  $\mathcal{A}_{2,i}$ ,  $\mathcal{B}_{2,i}$ ,  $\mathcal{C}_{2,i}$ , and  $\mathcal{D}_{2,i}$ , respectively, for  $i = 1$  to 4. The angle coupling in  $\mu$  results in cross-slab couplings. This corresponds to blocks outside the four  $16 \times 16$  squares, for example, the gray square  $\mathcal{C}_{13,\tilde{\varphi}}$  in the figure that couples  $\mathcal{C}_{1,\tilde{\varphi}}$  and  $\mathcal{C}_{3,\tilde{\varphi}}$ .

The stiffness  $\mathbf{K}$ , thus, can be divided into two parts: the coupling within the slab,  $\mathbf{A}$ ; the coupling across slabs  $\mathbf{B}$  where  $\mathbf{K} = \mathbf{A} + \mathbf{B}$ . Accordingly, Eqn. (4.5) is written

as,

$$\mathbf{K}\mathbf{a} = \mathbf{A}\mathbf{a} + \mathbf{B}\mathbf{a} = \mathbf{F}. \quad (4.6)$$

If the AD scheme is applied, the above equation is solved iteratively by assembling  $\mathbf{A}$  only. The second term  $\mathbf{B}\mathbf{a}$  can be approximated by using the solution  $\mathbf{a}$  from the previous step. Instead of solving  $\mathbf{a} = \mathbf{K}^{-1}\mathbf{F}$ ,  $\mathbf{A}$  is used as the approximate stiffness, and  $\mathbf{B}$  is moved to the right hand side of the linear Eqn. (4.6). Then, the iterative methods, *Gauss-Seidel* and *successive over-relaxation* methods are used to solve the above equation.

#### 4.4.2 iterative methods

Two iterative methods are discussed in this section. The first iterative method is a regular iterative method based on the method of matrix splitting. The second iterative method provides a relaxation factor to accelerate the convergence.

##### Gauss-Seidel method

For a given linear system of equations, such as Eqn. (4.6), the stiffness can be split into  $\mathbf{K} = \mathbf{A} + \mathbf{B}$ , to rewrite the equation as  $\mathbf{a} = \mathbf{A}^{-1}\mathbf{F} - \mathbf{C}\mathbf{a}$ , where  $\mathbf{C} = \mathbf{A}^{-1}\mathbf{B}$ . Subsequently, this is solved iteratively by updating the solution of each sub-domain until the residuals of the solution  $R_n = x_n - x_{n-1}$  at step  $n$  in all slabs converge to zero. Conceptually, the solution is expressed as an iteration,

$$\mathbf{a}_{n+1} = \mathbf{A}^{-1}\mathbf{F} - \mathbf{C}\mathbf{a}_n. \quad (4.7)$$

##### Successive over-relaxation method

One of the well-known modifications for the above iterative method is successive over-relaxation (SOR) method. Here is a brief derivation of the SOR method used in solving the RTE. The stiffness is decomposed as  $\mathbf{K} = \mathbf{A} + \mathbf{B}$ . The system of the

linear equations (4.5) can be written as,

$$\mathbf{A}\mathbf{a} = \alpha\mathbf{F} + [(1 - \alpha)A - \alpha B]\mathbf{a}, \quad (4.8)$$

where the constant  $\alpha \in (0, 2)$  is the relaxation factor. By solving the left hand side of the above equation for  $\mathbf{a}$ , and using the previous solutions for  $\mathbf{a}$ , Eqn. (4.5) is solved by the following successive relation,  $\mathbf{a}_{n+1} = \alpha\mathbf{A}^{-1}\mathbf{F} + [(1 - \alpha)\mathbf{I} - \alpha\mathbf{C}]\mathbf{a}_n$ . Or it can be expressed by the increments of unknowns,  $\Delta\mathbf{a}_{n+1} := \mathbf{a}_{n+1} - \mathbf{a}_n$ ,

$$\Delta\mathbf{a}_{n+1} = [(1 - \alpha)\mathbf{I} - \mathbf{C}]\Delta\mathbf{a}_n. \quad (4.9)$$

The initial value of the unknowns is often set to be  $\mathbf{a}_0 = 0$ .

The SOR method used for the RTE has a different decomposition scheme for  $\mathbf{K}$  compared to the traditional SOR method where the matrix is decomposed into a diagonal component and strictly upper and strictly lower triangle components. However, the relaxation factor is assigned in the same manner in that a value of  $\alpha < 1$  is often used to help establish convergence of a diverging iterative process while a value of  $\alpha > 1$  is used to speed up convergence of a slow-converging process. If  $\alpha = 1$ , the SOR method simplifies to the GS method.

### Numerical analysis of iterative methods

The SOR scheme is conditionally convergent. The common ratio of the SOR scheme,  $q$ , which is related to the convergence rate can be acquired by factorizing  $\mathbf{C} = \mathbf{U}^{-1}\mathbf{\Lambda}\mathbf{U}$ , where  $\mathbf{U}$  is the  $n \times n$  matrix whose  $i$ th column is the  $i$ th eigenvector of  $\mathbf{C}$ , and  $\mathbf{\Lambda}$  is the diagonal matrix whose diagonal elements are the corresponding eigenvalues of  $\mathbf{C}$ ,  $\{\lambda_i\}$ . Then, by pre-multiplying  $\mathbf{U}$ , Eqn. (4.9) is modified into a factorized form. The common ratio of its characteristic equation is

$$q = \max_i \|1 - \alpha - \alpha\lambda_i\|, \quad (4.10)$$

where  $\lambda$  is the eigenvalues of  $\mathbf{C}$ . In order to maintain a convergent process, the common ratio should be less than 1,  $q < 1$ .

### Optimal relaxation factor $\alpha_{\text{opt}}$

Figure 41 depicts the common ratios changing with the eigenvalues and the relaxation factor for a better understanding of the properties of the SOR scheme. The smaller  $q$ , the better the convergence. The white curves shows the optimal relaxation factors for the corresponding eigenvalues, *i.e.*, for a single eigenvalue, the optimal relaxation factor results in the fastest convergence. When the eigenvalues ranges from  $-0.5$  to  $1$ , there is an optimal  $\alpha$  for which  $q$  is zero, whereas for  $\lambda < -0.5$  the optimal  $\alpha$  is 2.

The optimal  $\alpha_{\text{opt}}$  for a best convergence rate is obtained by plugging the maximum and minimum  $\lambda$  into Eqn. (4.10) and requiring that both have the same  $q$  value when possible,

$$\alpha_{\text{opt}} = \text{Min} \left\{ \frac{2}{2 + \lambda_{\min} + \lambda_{\max}}, 2 \right\}. \quad (4.11)$$

## 4.5 Numerical examples

First, the convergence study is conducted by adopting the method of manufactured solution. Second, the stability of the iterative methods is numerically investigated. Third, the performance of the iterative solver is compared with the direct solver. Finally, an example with Gaussian point source is presented to demonstrate the flexibility and efficiently of the space-angle DG method and show how the number of iterations increase versus the scattering coefficient.

### 4.5.1 Convergence study

The following harmonic function is used as the manufactured solution to perform a convergence study for the proposed DG method,

$$I^M(r, \mu, \tilde{\varphi}) = \sin(\pi r) \sin(\mu) \sin(\tilde{\varphi}). \quad (4.12)$$

The detailed method of manufacture solution can be found in [119]. Since polynomials are used for the discrete solution in (4.4),  $I^h$  cannot exactly represent the manufactured solution (4.12) and the numerical error  $\varepsilon = I^h - I^M$  is nonzero for all element sizes and polynomial orders. As shown in Fig. 42, the asymptotic convergence rate of  $\beta_p = p + 1$  is achieved for polynomial order  $p$  as the element size  $h \rightarrow 0$ .

### 4.5.2 Numerical investigation of the stability of the iterative methods

The enclosure of two infinite concentric cylinders with radii of  $R_1 = 1$  and  $R_2 = 2$  contains an anisotropic scattering medium with isotropic incidence on both inner and outer walls with  $I(R_1) = I(R_2) = 1$ . The medium is cold (no emitting), so  $I_b = 0$  in (4.1). The extinction, absorption, and scattering coefficients are  $\beta = 1$ ,  $\kappa = 0.05$ , and  $\sigma_s = 0.95$ , respectively, *i.e.*, the intensity is strongly scattered in the medium. The Rayleigh scattering is used, where the phase function  $\Phi(\mu, \tilde{\varphi}, \mu', \tilde{\varphi}')$  is given,

$$\Phi(\mu, \tilde{\varphi}, \mu', \tilde{\varphi}') = \frac{3}{4} \left\{ 1 + \left[ \sqrt{(1 - \mu^2)(1 - \mu'^2)} \cos(\tilde{\varphi} - \tilde{\varphi}') + \mu\mu' \right]^2 \right\}. \quad (4.13)$$

Four structured meshes of  $4 \times 4 \times 4$ ,  $8 \times 8 \times 8$ ,  $16 \times 16 \times 16$ , and  $32 \times 32 \times 32$  resolution are used in the simulations. The polynomial order in space and angle is  $p = 0$  or  $p = 1$ . Both direct and iterative methods are used. Due to the computational

resource limits, the results for the  $32 \times 32 \times 32$  grid resolution are only obtained by iterative methods.

We want to numerically investigate whether the GS iteration can be applied to the RTE problem. We also want to study the effect of mesh resolution on the optimum value of  $\alpha$  for the SOR method.

The maximum and minimum eigenvalues of  $\mathbf{C}$  are computed for the  $4 \times 4 \times 4$ ,  $8 \times 8 \times 8$  and  $16 \times 16 \times 16$  mesh resolutions and the polynomial order  $p = 0$  in space and angle. As discussed in section 4.4.2, for the stability of the method the spectral radius of the amplification matrix must be less than one. For the GS method this means that  $\rho(\mathbf{C}) = \max \|\lambda\| < 1$ . In Figure 43(a) the maximum and minimum eigenvalues of the  $\mathbf{C}$  are plotted versus normalized scattering parameter  $\sigma_s/\beta$ , where  $\sigma_s/\beta = 0$  and  $\sigma_s/\beta = 1$  correspond to zero and maximum scattering. The energy is balanced only for  $\sigma_s/\beta = 1$ , for which black-body emission is ignored in the media.

As it can be seen for all values of  $\sigma_s/\beta$ ,  $\rho(\mathbf{C}) < 1$ . For  $\sigma_s = 0$ ,  $\mathbf{B} = \mathbf{0}$  corresponds to a nonscattering medium. As  $\sigma_s \rightarrow 0$ , we have  $\mathbf{C} \rightarrow \mathbf{0}$  and the GS and SOR both converge. As  $\sigma_s/\beta$  increases, so does  $\rho(\mathbf{C})$ , but satisfies the stability limit for the GS method. We also observe that for higher mesh resolution, the spectral radius increases. For example, for  $\sigma_s = 1$ ,  $\rho(\mathbf{C})$  increases from about 0.5 to 0.6 from  $4 \times 4 \times 4$  to  $16 \times 16 \times 16$  meshes.

Figure 44(a) shows the optimal value  $\alpha_{\text{opt}}$  for different nondimensional scattering coefficients and mesh resolutions. Interestingly, for all cases considered  $\alpha_{\text{opt}} > 1$ . As the medium becomes more scattering, that is as  $\sigma_s/\beta$  increases,  $\alpha_{\text{opt}}$  further increases beyond 1. Moreover, for the same  $\sigma_s/\beta$ , finer meshes have a higher  $\alpha_{\text{opt}}$ . This means that a fine-tuned  $\alpha$  from a less computationally intensive coarse mesh is not suitable for a finer mesh. Still, this figure provides an insight on how to assign  $\alpha$  based on the scattering parameter and mesh resolution. This figure also shows that the common ratio  $q$  increases for a higher scattering medium. This is expected as in Eqn. (4.6) a bigger portion of  $\mathbf{K}$  is not explicitly considered through matrix  $\mathbf{B}$ . Moreover, we observe that once the optimal  $\alpha$  is chosen independently for any mesh resolution, the

corresponding  $q$  is rather insensitive to the mesh resolution. That is, a higher mesh resolution does not adversely affect the convergence rate, once the corresponding optimal  $\alpha$  is chosen.

In addition, to further inspect the convergence rate and  $\alpha$ , the geometry is changed by fixing the outer radius  $R_2$  and changing the inner radius from  $R_1 = 0.25, 0.5, 0.75, 1.5, 1.75$  using the  $16 \times 16 \times 16$  mesh resolution. The maximum scattering is considered, i.e.,  $\sigma_s = \beta = 1$ . Figure 44(b) shows the optimal value  $\alpha_{\text{opt}}$  and the common ratio  $q$  against the ratio of  $R_1$  and  $R_2$ . The optimal  $\alpha$  decreases from 1.5 to 1.1, while  $q$  decreases from 0.6 to 0.2. As the optical depth decreases ( $R_1/R_2 \rightarrow 0$ ), the faster convergence is achieved.

The overall results show that the iterative method is convergent for the 1D cylindrical problems.

### 4.5.3 Acceleration of iterative methods

To compare the efficiency of the iterative methods, the relative numerical error for the global radiative intensity at iteration  $n$  is defined as,  $e^n(\mathbf{J}) = \max \|(\mathbf{J}^n - \mathbf{J}^{n-1})/\mathbf{J}^n\|$ , where  $\mathbf{J}$  is the vector of the radiation intensity at all Gauss points. That,  $e^n(\mathbf{J})$ , is the  $L_\infty$  error norm of the solutions between iterations  $n$  and  $n - 1$ . The numerical iterations continue until the two successive iterations converge with this error norm to within the tolerance  $10^{-13}$ .

Next, we investigate how the mesh resolution affects the optimum range of  $\alpha$  for the SOR method. The analysis in section 4.5.2 provides the optimal  $\alpha$  and  $q$ , solely based on the range of eigenvalues of  $\mathbf{C}$ . However, in this section we carry out the actual numerical solutions for different mesh resolutions and  $\alpha$  to verify whether the conclusions drawn from Figure 44 apply to actual RTE solutions. To achieve a higher accuracy,  $p = 1$  is used for the solutions in this section. Moreover, instead of considering a range of values, only  $\sigma_s/\beta = 0.95$  is considered in this example to limit the number of actual RTE solutions.

Table 3 compares the number of iterations needed for convergence for different mesh resolutions for the GS method (corresponding to the SOR methods for  $\alpha = 1$ ) and SOR method for  $\alpha = 1.1, 1.2, 1.3, 1.4, 1.5, 1.6$ . The above criterion in terms of the error  $e^n(\mathbf{J})$  is used to terminate the iterations. As it can be observed, the lowest number of iterations are achieved for  $\alpha = 1.1$  for mesh resolutions 4 and 8 and  $\alpha = 1.2$  for mesh resolutions 8, 16, and 32. This example suggests that the optimum value of  $\alpha$  to increases for higher resolution meshes, which shows the same trend in Figure 44(a). For the remainder of this section, results for different mesh resolutions are reported based on their optimum  $\alpha$  within the range of values considered above.

Figure 45 shows the evolution of the error  $e(\mathbf{J})$  versus iteration number for the GS and SOR methods for the coarsest ( $4 \times 4 \times 4$ ) and the finest ( $32 \times 32 \times 32$ ) meshes with  $p = 1$ . The optimum value of  $\alpha$  is chosen for each mesh for the SOR results. It is shown that, for this particular case, the SOR method significantly outperforms the GS method for the fine mesh, while for the coarse mesh, there are not much difference in the performance of the two methods.

Next, we compare the efficiency of the iterative and direct solvers. Figure 46(a) shows the memory usage of the iterative methods (for all  $\alpha$ ) and the direct solver. The memory of direct solver is significantly higher than the iterative methods. For example, for the mesh resolution  $16 \times 16 \times 16$ , the memory usage of direct and iterative solvers are around 2.5 GB and 220 MB, respectively. Due to the fast growth of the memory, we could not use the direct solver for the  $32 \times 32 \times 32$  mesh. More significant is the rate at which the memory usage increases versus the problem size; for the direct solver, the memory usage scales linearly versus the total number of elements in space-angle, whereas for the iterative methods the memory usage is proportional to the number of elements in an individual slab. Thus, for the 1D cylindrical symmetry problem considered, the rate of increase of memory versus mesh resolution would be 3 and 2 for the direct and iterative methods, respectively. This explains the lower asymptotic slope of memory usage versus mesh resolution for iterative solvers as the mesh resolution increases in the figure.

Figure 46(b) compares the efficiency of the two methods in terms of the CPU time. For the iterative methods, the SOR method with  $\alpha = 1.2$  outperforms the GS method since overall a fewer number of iterations are needed. Otherwise, the solution cost per iteration is the same for the two iterative methods. For both direct and iterative solver, we solve the system directly using the LU factorization method provided by MUMPS library [8]. It is evident that for the coarse meshes, the solution cost of the direct and iterative solvers are close. In contrast, for finer meshes the iterative solvers are significantly more efficient even though for the iterative methods many iterations are needed to achieve convergence. This means that by dividing the space-angle domain to smaller slabs, we save not only on memory usage, but also on the overall CPU time.

#### 4.5.4 Internal Gaussian source in small scattering albedo media

A Gaussian point source added on the right-hand side of (4.2) is applied in the annulus where the inner circle radius  $R_1$  and outer circle radius  $R_2$  are 1 and 2, respectively. The source term is,

$$S = 10e^{-1000[(r-r_0)^2+(\mu-\mu_0)^2+(\tilde{\varphi}-\tilde{\varphi}_0)^2]}, \quad (4.14)$$

where the center point  $p_0$  is at  $(r_0, \mu_0, \tilde{\varphi}_0) = (1.23, 0, 2.5\pi)$ . The medium is cold and gray. The absorption coefficient  $\kappa = 3$  is fixed, while the scattering coefficient  $\sigma_s$  changes exponentially from  $1 \times 10^{-6}$  to 1. The relaxation factor for the SOR method is  $\alpha = 1$  in this case, because for the scattering albedo  $\sigma_s/\beta$  close to 0, the optimal  $\alpha_{\text{opt}}$  tends to 1.

The mesh shown in Figure 47a is refined around  $p_0$  with 96 elements in  $\tilde{\varphi}$  and 32 elements in  $\mu$ , as well as, 32 isometric elements in space. The polynomial order is  $p = 2$ . The number of iterations is measured for different scattering coefficients,

as shown in Figure 47b. For  $\sigma_s \leq 0.01$ , fast convergence rate and small number of iterations are observed. With the 0 initial guess of the iterative method, the minimum number of iterations is 5 for  $\sigma_s = 1e - 6$  and  $1e - 5$ . As the scattering coefficient  $\sigma_s$  increases beyond 0.1, the number of iterations increases linearly. Figure 47c shows the solution of  $\sigma_s = 1 \times 10^{-5}$  medium with the internal source in the  $r - \tilde{\varphi}$  plane, where  $\mu = 0$ . Since the scattering albedo is too weak, the intensity off the characteristics of the source term is close to zero.

## 4.6 Discussion and conclusions

An iterative RTE solver with an angular decomposition (AD) method using the space-angle discontinuous Galerkin method was presented. The iterative solver has several advantages compared to a direct space-angle solution method. First, the number of non-zero elements in the effective stiffness matrix is significantly reduced when the AD method is applied. That is, the stiffness matrix of the iterative solver uses less computational resources to assemble and compute than the direct solver. Second, Figure 46(b) indicates that the iterative solver becomes even more efficient than the direct solver as the problem size increases. Moreover, the AD method lends itself to parallel computing as individual slabs can be solved in parallel with minimal communication burden.

The GS method is very similar to the one used in the discrete ordinate methods. However, there are two advantages to the proposed iterative method. First, the use of the DG method for the angle (as well as space) direction(s) can enhance the robustness and accuracy of the solution. Second, by tuning the  $\alpha$  in the SOR method, we can expedite the convergence of the iterative method. In fact, the comparison made between the two iterative methods indicates that a proper (optimal) relaxation factor for the SOR method can expedite the convergence of the SOR method. Especially, once the optimal relaxation factor is determined, the common ratio (convergence rate) is insensitive to the mesh resolution for the same problem, as suggested in Figure 43(a). However, the determination of the optimal relaxation factor is difficult.

Hardy *et al.* [76] propose examining the performance of the method for a coarse mesh to determine the optimal value of relaxation parameter. Nevertheless, as shown in Table 3, the optimal relaxation factor changes for different mesh resolutions. The reason for this is that the eigenvalue range of the matrix  $\mathbf{C} = \mathbf{A}^{-1}\mathbf{B}$  changes as a function of mesh resolution, thus affecting the optimal value for  $\alpha$ . This is evident in terms of the minimum and maximum eigenvalues of  $\mathbf{C}$  in Figure 43(a).

There are several noteworthy extensions to this work. First, given that the space-angle domain is already divided into slabs in the angle-direction, we can employ an *Angle-Decomposition* (AD) method to parallelize the solution, as for example in [12]. This combined with the SOR iterative method can drastically reduce the computational time. Second, the determination of optimal value of  $\alpha$  for different mesh resolutions requires more rigorous analysis. Third, the real gains of the proposed AD SOR iterative method are expected to be for 2D and 3D problems; for example, the memory usage decreases by powers of 1/2 and 2/5 for 2D and 3D problems, respectively, as compared to 2/3 observed for the cylindrical symmetric problem considered herein. We note that our preliminary results for 2D problems are promising. First, the iterative method can drastically increase the problem sizes that can be tackled compared to the direct solution method. Second, in these results the over-relaxed iterations are about 33% more efficient than the GS iteration. Finally, adaptivity in space and/or angle can greatly reduce the computational cost for the same level of solution accuracy. Although done in a different context, we plan to employ the DG  $h$ -adaptive mesh operations proposed in [2, 6] for this purpose.

## Chapter 5

# Combined Angular and Domain Decomposition Parallel Methods to Solve 2D Radiative Transfer Problems Using Space-Angle Discontinuous Galerkin Method

## 5.1 Abstract

This article presents a useful method for employing distributed computing to simulate radiative transfer phenomena numerically. The discontinuous Galerkin (DG) finite element method (FEM) is used to solve the steady-state radiative transfer equation (RTE) for two-dimensional problems involving absorption, emission, and scattering with the semitransparent medium. The DG approach discretizes both spatial and angular directions. Angular decomposition (AD) and domain decomposition (DD) approaches are parallelization techniques implemented in this work. Two-dimensional radiative problems are constructed, and a thorough evaluation of scalability, performance, and efficiency on high processors is illustrated. A two-dimensional complex geometry involving inclined boundaries and a semi-trapezoidal enclosure is validated as a non-scattering homogeneous gray medium. The performance of hybrid AD-DD systems has been demonstrated to be superior to that of AD and DD methods utilized independently. Finally, we also investigate a square enclosure with circular and square obstacles with a scattering gray semitransparent medium.

## 5.2 Introduction

Radiative transfer is the energy transfer phenomenon in the form of electromagnetic waves, frequently distinguished by their radiative intensity. Contrary to heat conduction and convection, it does not require a medium to transport energy. All materials have a greater spontaneous capacity to emit and absorb electromagnetic waves at higher temperatures. Therefore, it is essential to involve the ultra-long or ultra-near functionalities, vacuum, and high temperatures applications, such as industrial furnaces and combustion chambers with high temperatures [10][85], infrared detectors [131][14], thermal images [115], neutrons [39][36], microelectronics [47][90], satellites and astrophysics [66][103], the solar photovoltaic and photo-thermal industry [65][64], optical imaging [71], to name a few. Radiative heat transfer is becoming more

crucial and in ever-increasing demand as contemporary technology progresses toward ultra-high temperatures, higher efficiency, extreme sizes, and space.

The governing equation for the radiative transfer process is the radiative transfer equation (RTE), an intricate integral-differential equation. The Monte Carlo method is a popular stochastic strategy for solving the RTE [141][106]. This approach is incredibly adaptable and easy to set up. The cons of this approach are that it is time-consuming and less efficient due to the iterative approach. The most popular deterministic approaches are the spherical harmonics method ( $P_N$  method) [52] and the discrete-ordinates method (DOM) [78]. The DOM may be susceptible to ray effects [130] and spurious scattering under some circumstances, which might result in incorrect solutions. In contrast, the most efficient methods for spatial discretization are the finite difference method (FDM) [18], finite volume method (FVM) [136], finite element method (FEM) [92], discontinuous Galerkin (DG) [129] [59], and so on. The FVM or (continuous) finite element method spatially discretized these differential equations. However, the continuous scheme utilized in the FEM rarely captures the discontinuity brought on by the existence of impediments. To enhance, the DG method is used. The DG approach is helpful in modeling discontinuous hyperbolic partial differential problems. It benefits from high-order precision, flexibility to irregular shapes, good convergence properties, ease of parallel calculation, and a strong theoretical foundation for error estimates and stability [126]. Using the DG method, Zhao and Liu [140] solved multidimensional discrete ordinate equations. The DG approach avoids artificial coupling since it is inherently discontinuous. Theoretically, it may be used to discretize angular direction and spatial domain. Clarke solved radiative transfer on parallel planes and concentric cylinders [28], and Wang *et al.* [120] using the space-angle DG (saDG) methods, respectively. The distribution of radiative intensity in spatial and angular domains varies significantly for multidimensional radiative transfer in irregular geometries with barriers. Therefore, it is crucial to discretize the spatial domain and angular direction using the DG approach.

Parallel computing can produce time- and memory-efficient methods, even though creating accurate angular and spatial discretization's is essential for the numerical solution of RTE. For difficult computational models, parallel processing is also necessary, coupled with scalable and effective methods (heterogeneous medium, three-dimensional complex geometry, *etc.*). The linear equations from the coupled spatial-angular discretization are implicitly used by a Krylov subspace incremental algorithm, in contrast to space-marching and source iteration methods for the solution of RTE [41]. The benefits of such an approach over more traditional ones like space-marching and source iteration in [107]. Implicit schemes are essential for dealing with ill-conditioned matrices, which typically appear in radiation issues with heterogeneity's, complicated geometries, high scattering, and reflections. Research has demonstrated the benefits of parallel computing to solve RTE [74][63]. Krishnamoorthy *et al.* [74] provided parallelization of the DOM-FVM for emitting-absorbing medium in Krylov subspace approaches, along with a domain decomposition (DD) method. Marc [25] proposed a pseudo-time marching-based implicit parallel approach utilizing the DD method for the DOM-FVM. They observed 256 processes, a two-dimensional spatial mesh with 5122 nodes in quadrature, 80 directions, and a remarkable scaling efficiency of more than 85%.

A comparison of parallelization based on spatial DD vs parallelization based on angular decomposition (AD) based on previous work suggests that the former is superior [48]. The most significant constraint of the AD approach is introduced since, in reality, only a small number of ordinates are used, often a few hundred for the largest applications. Gonçalves [53] studied employing AD and DD approaches for emitting-absorbing media to parallelize a space-marching algorithm for the DOM-FVM. Each processor handles only a few directions in the AD while performing calculations for the entire domain. In contrast, in the DD, each processor handles all directions while performing computations for only a single subdomain. Contrary to the DD, better efficiency was achieved in the AD since the number of iterations was independent of the number of processors. The AD and DD methods were

presented by Kanschat [68] for the DOM-FEM-based RTE solution. The advantages of ordinate parallelism of the AD method, as opposed to the DD method, were stressed. In this investigation, parallelization and adaptive mesh refinement were both employed. Badri *et al.* [13] investigated the high-performance computing numerical solution of RTE using the FEM alongside the DOM for spatial-angular discretization. They presented two parallel methods of AD and DD and examined the efficiency, performance, and scalability of thousands of processors for two- and three-dimensional examples. The numerical results showed that AD performs better than DD.

In this paper, the space-angle discontinuous Galerkin method is developed to solve the RTE for angular decomposition and domain decomposition parallel method for different 2-dimensional complex enclosures. The rest of the paper is organized as follows: Section 5.3 presents the formulations of the RTE equation and space-angle DG method. The implementation of AD and DD is elaborated on in Section 5.4. Section 5.5 illustrates some numerical examples of validation, scaling performance of weak and strong scaling of AD, DD, and hybrid AD-DD, and an anisotropic scattering problem of square geometry with obstacles. Finally, the concluding remarks of the article are presented in Section 5.6.

### 5.3 Formulation

The two-dimensional Cartesian steady-state RTE in a gray medium that absorbs, emits, and scatters has the form,

$$\begin{aligned} \zeta \frac{\partial I(x, y, \mu, \varphi)}{\partial x} + \eta \frac{\partial I(x, y, \mu, \varphi)}{\partial y} + \beta I(x, y, \mu, \varphi) = \\ \kappa I_b(x, y) + \frac{\sigma_s}{4\pi} \int_{-1}^1 \int_{-\pi}^{\pi} I(x, y, \mu', \varphi') \Phi(\mu, \varphi, \mu', \varphi') d\mu' d\varphi', \end{aligned} \quad (5.1)$$

where  $I(x, y, \mu, \varphi)$  is the radiative intensity in the  $x$ - $y$  plane along the solid angle direction  $\hat{\mathbf{s}}(x, y, z) = \{\zeta, \eta, \mu\}$  assuming that  $z$  axis is infinity, where  $\zeta = \sin \theta \cos \varphi = \sqrt{1 - \mu^2} \cos \varphi$ ,  $\eta = \sin \theta \sin \varphi = \sqrt{1 - \mu^2} \sin \varphi$ ,  $\mu = \cos \theta$ ;  $\theta$  and  $\varphi$  are the polar and

azimuthal angle measured with respect to a fixed axis in space, respectively. The range of the polar and azimuthal angle should be  $\theta \in [0, \pi]$  and  $\varphi \in [-\pi, \pi]$ . The values  $\beta$ ,  $\kappa$ , and  $\sigma_s$ , are the spatial-dependent extinction, absorption, and scattering coefficients, respectively. The spatial-dependent total black-body radiative intensity is given by  $I_b$ . The scattering phase function is represented by  $\Phi(\mu, \varphi, \mu', \varphi')$ . The often-used Rayleigh scattering phase function is expressed as,

$$\Phi(\mu, \varphi, \mu', \varphi') = \frac{3}{4} \left\{ 1 + \left[ \sqrt{(1 - \mu^2)(1 - \mu'^2)} \cos(\varphi - \varphi') + \mu\mu' \right]^2 \right\}. \quad (5.2)$$

The partial differential equation (PDE) is enforced in a 4-dimensional domain  $(x, y, \mu, \varphi) \in \Omega$ . The boundary conditions are specified on inflow boundaries for  $I$ ,

$$I(\mathbf{r}_w, \hat{\mathbf{s}}) = I^p, \quad \hat{\mathbf{s}} \cdot \mathbf{n} < 0, \quad (5.3)$$

where  $I^p$  is the prescribed intensity,  $\mathbf{n}$  is the outward surface normal. In the space-angle domain, the surface normal  $\mathbf{n}$  has spatial components and angular components  $\mathbf{n}(x, y, z, \mu, \varphi) = \{n_x, n_y, n_z, n_\mu, n_\varphi\}$ , so that  $\hat{\mathbf{s}} \cdot \mathbf{n} = \zeta n_x + \eta n_y + \mu n_z = \zeta n_x + \eta n_y$ , where  $n_z = 0$  in the 2D spatial geometry.

### 5.3.1 Space-angle discontinuous Galerkin method

In this paper, we employ the space-angle DG method to solve the RTE in both space and angle. The space-angle domain is generated by extruding the spatial domain as shown in Fig. 48 in a space-angle space. The space element  $\mathcal{Q}_x$  is extruded into  $m$  slabs in angle resulted in  $\mathcal{Q}_1, \mathcal{Q}_2, \dots, \mathcal{Q}_m$  space-angle elements. The sample element  $\mathcal{Q}^l$  has the boundaries in  $\mathbf{x}$  direction,  $\partial\mathcal{Q}_x^l$ , and boundaries in  $\hat{\mathbf{s}}$  direction,  $\partial\mathcal{Q}_s^l$ . In the 2D domain, the space mesh consists of unstructured triangles, whereas the extrusion process results in a structured rectangular mesh in angle. For an arbitrary element

$\mathcal{Q}^l$ , the residuals are,

$$\begin{aligned} \mathcal{R}_{\mathcal{Q}^l} &= \zeta \frac{\partial I}{\partial x} + \eta \frac{\partial I}{\partial y} + \beta I \\ &\quad - \kappa I_b - \frac{\sigma_s}{4\pi} \int_{-1}^1 \int_{-\pi}^{\pi} I(x, y, \mu', \varphi') \Phi(\mu, \varphi, \mu', \varphi') d\mu' d\varphi', \end{aligned} \quad (5.4a)$$

$$\mathcal{R}_{\partial\mathcal{Q}^l} = \hat{\mathbf{s}} \cdot \mathbf{n}(I^* - I), \quad (5.4b)$$

where (5.4a) corresponds to the residual inside element  $\mathcal{Q}^l$  in satisfying the RTE in (5.1).

(5.4b) corresponds to the residual in enforcing the target value,  $I^*$ , on  $\partial\mathcal{Q}^l$ , the boundaries of  $\mathcal{Q}^l$ . This condition and the factor  $\hat{\mathbf{s}} \cdot \mathbf{n} = \zeta n_x + \eta n_y$  directly correspond to the jump part of the differential operator  $\zeta \frac{\partial I}{\partial x} + \eta \frac{\partial I}{\partial y}$  in (5.1). The target value  $I^*$  corresponds to the upstream value along the direction of wave propagation, which is given,

$$I^* = \begin{cases} I, & \hat{\mathbf{s}} \cdot \mathbf{n} > 0 \\ I^{\text{out}}, & \hat{\mathbf{s}} \cdot \mathbf{n} \leq 0 \end{cases}, \quad (5.5)$$

if  $\hat{\mathbf{s}} \cdot \mathbf{n} > 0$ , the element boundaries are outflow boundaries, where  $I^* = I$  implies that (5.4b) is trivially satisfied. If  $\hat{\mathbf{s}} \cdot \mathbf{n} \leq 0$ , the element boundaries are inflow boundaries. In this case,  $I^* = I^{\text{out}}$  corresponds to the boundary value of its neighbor element. In the 2D space-angle domain, the direction of the wave only propagates along space, which means only the residuals on the element boundary  $\mathcal{R}_{\partial\mathcal{Q}_x^l}$  are considered in Fig. 48. The jump condition on  $\mathcal{R}_{\partial\mathcal{Q}_s^l}$  are trivially satisfied. For example in Fig. 49,  $\mathbf{n}_1$ ,  $\mathbf{n}_2$ , and  $\mathbf{n}_3$  correspond to the outward surface normal on element boundaries  $\partial\mathcal{Q}_{\mathbf{x}_1}^l$ ,  $\partial\mathcal{Q}_{\mathbf{x}_2}^l$ , and  $\partial\mathcal{Q}_{\mathbf{x}_3}^l$ , respectively. Outside  $\mathcal{Q}^l$ , the boundary condition  $I^p$  on  $\partial\mathcal{Q}_{\mathbf{x}_1}^l$  and the element boundary values  $I^{\text{out}}$  on  $\partial\mathcal{P}$  and  $\partial\mathcal{O}$  are specified. For a given angle  $\hat{\mathbf{s}}$ , since  $\hat{\mathbf{s}} \cdot \mathbf{n}_1 < 0$ ,  $\hat{\mathbf{s}} \cdot \mathbf{n}_2 < 0$ , and  $\hat{\mathbf{s}} \cdot \mathbf{n}_3 > 0$ , the nontrivial jump conditions are enforced on  $\partial\mathcal{Q}_{\mathbf{x}_1}^l$  and  $\partial\mathcal{Q}_{\mathbf{x}_2}^l$  (element boundaries in red), while boundary  $\partial\mathcal{Q}_{\mathbf{x}_3}^l$  (in blue) is the outflow boundary.

The unknown fields  $I_{\mathcal{Q}^l}^h$  in element  $\mathcal{Q}^l$  are interpolated by tensorial product polynomials of order  $p_{\mathbf{x}}$  in space and  $p_{\hat{\mathbf{s}}}$  in angle, which is written as,

$$I_{\mathcal{Q}^l}^h(\mathbf{x}, \hat{\mathbf{s}}) = H_r^{\mathcal{Q}^l}(\mathbf{x}) \otimes H_{\hat{\mathbf{s}}}^{\mathcal{Q}^l}(\hat{\mathbf{s}}) \cdot \mathbf{a}^{\mathcal{Q}^l}, \quad (5.6)$$

where  $\mathbf{a}$  is the vector of unknowns for the discrete solution,  $H$  is the basis function vector formed by polynomials, and the subscripts  $\mathbf{x}$  and  $\hat{\mathbf{s}}$  denote the space and angle, respectively. The tensorial product polynomials are used to interpolate the unknown field of order  $p_{\mathbf{x}}$  in space and order  $p_{\hat{\mathbf{s}}}$  in angle. For the 2D space-angle domain,  $H_r^{\mathcal{Q}^l}$  is formed by Pascal's triangle in  $x$  and  $y$ ,  $H_r^{\mathcal{Q}^l}(x, y) = \{x^i y^j | i + j \leq p_{\mathbf{x}}\}$ .  $H_{\hat{\mathbf{s}}}^{\mathcal{Q}^l}$  is formed by monomials,  $H_{\hat{\mathbf{s}}}^{\mathcal{Q}^l}(\varphi, \mu) = \{\varphi^i \mu^j | i = 0, 1, \dots, p_{\hat{\mathbf{s}}}, j = 0, 1, \dots, p_{\hat{\mathbf{s}}}\}$ . For example, for  $p_{\mathbf{x}} = 1$  and  $p_{\hat{\mathbf{s}}} = 2$ ,  $H_r^{\mathcal{Q}^l}(x, y) = \{1, x, y\}$  and  $H_{\hat{\mathbf{s}}}^{\mathcal{Q}^l}(\varphi, \mu) = \{1, \varphi, \varphi^2, \mu, \varphi\mu, \varphi^2\mu, \mu^2, \varphi\mu^2, \varphi^2\mu^2\}$ .

The weighted residual (WR) statement for a space-angle region  $\mathcal{Q}^l$  is formed by multiplying the RTE by the weight function  $\hat{I}$  and adding the corresponding weighted residuals on the boundary of the element, which is given as,

$$\int_{\mathcal{Q}^l} \hat{I} \mathcal{R}_{\mathcal{Q}^l} dV_{\mathcal{Q}^l} + \int_{\partial\mathcal{Q}^l} \hat{I} \mathcal{R}_{\partial\mathcal{Q}^l} dA_{\partial\mathcal{Q}^l} = 0. \quad (5.7)$$

In the 2D geometry discrete setting,  $\mathcal{Q}^l$  represents a space-angle element and the intensity  $I$  is replaced by its discrete approximation  $I_{\mathcal{Q}^l}^h = \mathbf{H}^{\mathcal{Q}^l} \cdot \mathbf{a}^{\mathcal{Q}^l}$  in  $\mathcal{Q}^l$ . By replacing  $\mathcal{R}_{\mathcal{Q}^l}$  and  $\mathcal{R}_{\partial\mathcal{Q}^l}$ , the above equation is written as,

$$\begin{aligned} & \int_{\mathcal{Q}^l} \hat{I} \left( \zeta \frac{\partial \mathbf{H}^{\mathcal{Q}^l}}{\partial x} + \eta \frac{\partial \mathbf{H}^{\mathcal{Q}^l}}{\partial y} + \beta \mathbf{H}^{\mathcal{Q}^l} - \kappa I_b \right) \cdot \mathbf{a}^{\mathcal{Q}^l} dV_{\mathcal{Q}^l} \\ & - \int_{\mathcal{Q}^l} \hat{I} \left[ \frac{\sigma_s}{4\pi} \sum_{j=1}^m \left( \int_{\mathcal{Q}_{\hat{\mathbf{s}}}^j} \mathbf{H}^{\mathcal{Q}^j} \cdot \mathbf{a}^{\mathcal{Q}^j} \Phi dA_{\mathcal{Q}_{\hat{\mathbf{s}}}^j} \right) \right] dV_{\mathcal{Q}^l} \\ & + \sum_{i=1}^3 \int_{\partial\mathcal{Q}_{\mathbf{x}_i}^l} \hat{I} [\hat{\mathbf{s}} \cdot \mathbf{n} (I^* - \mathbf{H}_{\partial\mathcal{Q}^l} \cdot \mathbf{a}_{\partial\mathcal{Q}^l})] dA_{\partial\mathcal{Q}_{\mathbf{x}_i}^l} = 0 \end{aligned} \quad (5.8)$$

The volume of space-element  $\mathcal{Q}^l$  is denoted by  $V_{\mathcal{Q}^l}$ . The area of the boundary  $\partial\mathcal{Q}_x^l$  is denoted by  $A_{\partial\mathcal{Q}_x^l}$ . The equation above is enforced for all elements  $\mathcal{Q}^l$  in the entire space-angle domain  $\Omega$ . Elements are coupled through  $I^*$  terms in the  $x$ - $y$  planes and the phase integral in angle directions  $\mu$  and  $\varphi$ . This results in a global linear system of equations,

$$\mathbf{K}\mathbf{a} = \mathbf{F} \tag{5.9}$$

where  $\mathbf{a}$  is the global unknown vector formed from individual element unknowns  $\mathbf{a}_{\mathcal{Q}^l}$ ,  $\mathbf{K}$  is the *stiffness matrix*, and  $\mathbf{F}$  is the force vector comprising the terms that are independent of element unknowns  $\mathbf{a}$ .

In the previous paper, we developed an accelerated iteration method for solving 1D cylindrical RTE using the space-angle DG formulation by adopting the successive over-relaxation (SOR) method. A short introduction is provided to facilitate the discussion of the angular decomposition method in Section [5.4.1](#).

## 5.4 Implementation

Assembling the entire system directly can result in a dense stiffness matrix that is difficult to solve due to its high dimension and the presence of scattering term. To handle this issue, especially when dealing with large-scale problems, it is important to parallelize the solution process. Two popular methods for increasing scalability are the angular decomposition and domain decomposition methods. In this section, we will outline the specifics of these two decomposition methods.

### 5.4.1 Angular Decomposition

The direct assembly of the whole system may result in a very dense stiffness matrix, which can be challenging to solve because of the interdependence between different angular domains. This is due to the second term, the scattering term  $\mathcal{S}$ , in the

equation (5.8) for element  $\mathcal{Q}^l$ , which requires interactions with all angular elements that have been extruded from the same spatial element. This can significantly increase the size of the stiffness matrix and make it difficult to store, especially as the system size grows.

To address this issue, we have developed the angular decomposition (AD) method to decouple the angular domain. This involves replacing the discrete solutions with calculated values, so that the coupling terms are treated as sources, contributing to the right-hand side of the equation. Unlike the direct solver, which solves the system directly, the AD method divides the angular domain into slabs and solves each slab separately, resulting in an iterative process. Therefore, the scattering term  $\mathcal{S}$  at iteration step  $k$  is written as,

$$\begin{aligned} \mathcal{S} = & - \int_{\mathcal{Q}^l} \hat{I} \left[ \frac{\sigma_s}{4\pi} \left( \int_{\mathcal{Q}_s^l} \mathbf{H}^{\mathcal{Q}^l} \cdot \mathbf{a}^{\mathcal{Q}^l} \Phi dA_{\mathcal{Q}_s^l} \right) \right] dV_{\mathcal{Q}^l} \\ & - \int_{\mathcal{Q}^l} \hat{I} \left[ \frac{\sigma_s}{4\pi} \sum_{j=1}^{j<l} \left( \int_{\mathcal{Q}_s^j} I_{\mathcal{Q}^j}^k \Phi dA_{\mathcal{Q}_s^j} \right) \right] dV_{\mathcal{Q}^l} \quad , \quad (5.10) \\ & - \int_{\mathcal{Q}^l} \hat{I} \left[ \frac{\sigma_s}{4\pi} \sum_{j=1}^{j>l} \left( \int_{\mathcal{Q}_s^j} I_{\mathcal{Q}^j}^{k-1} \Phi dA_{\mathcal{Q}_s^j} \right) \right] dV_{\mathcal{Q}^l} \end{aligned}$$

where  $I_{\mathcal{Q}^j}^k$  is the approximate solutions in element  $\mathcal{Q}^j$  at iteration  $k$ . The first term in (5.10) still contributes to the formation of the matrix, whereas the second and third terms play a role in the construction of the right-hand side. Such processes also significantly increase the sparsity of the stiffness matrix, resulting in a block-diagonal structure. This method is highly parallelizable, as the calculations of each slab can be performed independently.

If  $n_p$  MPI processors are applied to partition the angular domain, the above equation can be rewritten as,

$$\begin{aligned}
\mathcal{S}^M = & - \int_{\mathcal{Q}_{M,l}} \hat{I} \left[ \frac{\sigma_s}{4\pi} \left( \int_{\mathcal{Q}_{\hat{s}}^{M,l}} \mathbf{H}^{\mathcal{Q}_{M,l}} \cdot \mathbf{a}^{\mathcal{Q}_{M,l}} \Phi dA_{\mathcal{Q}_{\hat{s}}^{M,l}} \right) \right] dV_{\mathcal{Q}_{M,l}} \\
& - \int_{\mathcal{Q}_{M,l}} \hat{I} \left[ \frac{\sigma_s}{4\pi} \sum_j^{j < l} \left( \int_{\mathcal{Q}_{\hat{s}}^{M,j}} I_{\mathcal{Q}_{M,j}}^k \Phi dA_{\mathcal{Q}_{\hat{s}}^{M,j}} \right) \right] dV_{\mathcal{Q}_{M,l}} \\
& - \int_{\mathcal{Q}_{M,l}} \hat{I} \left[ \frac{\sigma_s}{4\pi} \sum_j^{j > l} \left( \int_{\mathcal{Q}_{\hat{s}}^{M,j}} I_{\mathcal{Q}_{M,j}}^{k-1} \Phi dA_{\mathcal{Q}_{\hat{s}}^{M,j}} \right) \right] dV_{\mathcal{Q}_{M,l}} \quad , \quad (5.11) \\
& - \int_{\mathcal{Q}_{M,l}} \hat{I} \left[ \frac{\sigma_s}{4\pi} \sum_{i,j}^{i \neq p, j < l} \left( \int_{\mathcal{Q}_{\hat{s}}^{i,j}} I_{\mathcal{Q}_{i,j}}^k \Phi dA_{\mathcal{Q}_{\hat{s}}^{i,j}} \right) \right] dV_{\mathcal{Q}_{M,l}} \\
& - \int_{\mathcal{Q}_{M,l}} \hat{I} \left[ \frac{\sigma_s}{4\pi} \sum_{i,j}^{i \neq p, j \geq l} \left( \int_{\mathcal{Q}_{\hat{s}}^{i,j}} I_{\mathcal{Q}_{i,j}}^{k-1} \Phi dA_{\mathcal{Q}_{\hat{s}}^{i,j}} \right) \right] dV_{\mathcal{Q}_{M,l}}
\end{aligned}$$

where  $M$  is the index of the angular subdomain. For the balancing purpose, the slabs have to be evenly assigned to each subdomain. Hence, the maximum number of processors can not exceed the number of slabs. Fig. 50 shows an example of 16 extruded elements in angles  $\varphi$  and  $\mu$  divided into 4 subdomains (red and blue boxes), so that each slab contains 4 slabs. The calculations of the scattering term in subdomain 1 by the AD method for one iteration can be broken into the following steps:

1. Assemble the local system for slab  $j$  in subdomain 1 by Equation 5.8, except for the scattering term  $\mathcal{S}^M$ .
2. For slab  $j$ , the scattering term  $\mathcal{S}^1$  is performed over the angular domain. The first term in Equation 5.11 contributes to the local stiffness matrix in slab  $l$  and subdomain  $M$ . The second and third terms contribute to the right-hand side (RHS), *i.e.*, the force vector. The last two terms need solutions from other subdomains so that interprocessor communication is required.

3. The solution of slab  $j$  is calculated after the assembly stage and the intensity is then updated.
4. Repeat steps (1) to (3), until the solutions for all slabs in subdomain 1 are updated.

### 5.4.2 Domain decomposition

For the domain decomposition (DD) method, the spatial mesh is divided into smaller subdomains. One option is to solve each subdomain with the same governing equation individually by the assigned processor, which is known as the conventional DD method. Subdomains are not isolated, since the continuity on the subdomain interfaces is weakly enforced. Therefore, communications to pass the interface solutions are needed. Similar to the AD method, to achieve the global solutions, iteration is required, since the local solutions inside subdomains depend on the previous iteration from the neighbor subdomains. Another option is to obtain the global linear system of equations directly by assembling the local stiffness matrices in the subdomains in a distributed manner and solving the whole with a distributed-memory linear solver, such as MUMPS [8]. In this case, calculation of the jump conditions is required on the subdomain interface from the neighbor elements in other subdomains. To reduce the amount of communication, additional elements belonging to the respective adjacent processor are added to the border of each subdomain. These elements are referred to as ghost elements. As depicted in Fig. 51, the ghost elements in green in subdomain 1 are duplicated from subdomain 2. For a given angle  $\hat{s}$ , the inflow and outflow boundaries between subdomains 1 and 2 are in red and blue, respectively. Because of the creation of ghost elements, each processor is required to take more memory than the conventional DD method. However, it is worth solving the global linear system directly rather than iteratively by sacrificing some memory usage. The implementation of the Domain Decomposition method in

the Discontinuous Galerkin (DG) method in parallel computing can be accomplished as follows:

1. Divide the computational domain into subdomains: The first step is to divide the computational domain into a number of smaller subdomains, each of which will be solved independently by a separate processing unit.
2. Assemble the local matrices: For each subdomain, the local matrices are assembled using the DG method. The local matrices are then used to form the global matrices, taking into account the information exchanged between subdomains.
3. Exchange information between subdomains: To ensure that the solution in each subdomain is consistent with the solutions in neighboring subdomains, information is exchanged between subdomains. This information is typically exchanged via ghost elements, which are used to communicate information between adjacent subdomains. For example, the subdomain interface of element 1 is the inflow boundary, where its neighbor element, the ghost element 6, is duplicated from subdomain 2.
4. Solve the global matrices: The global matrices are then solved internally, and the solutions are assigned to the respective subdomains.

## 5.5 Numerical examples

This section illustrates some numerical problems. A two-dimensional complex geometry with inclined boundaries of a semi-trapezoidal enclosure with a non-scattering homogeneous gray medium, scattering and non-scattering scaling performance checking of the enclosure, and a square enclosure with obstacles and scattering problems are considered to thoroughly test the numerical solution method for solving the RTE. These problems are solved by using C++with the University

of Tennessee in Knoxville's ISAAC (Infrastructure for Scientific Applications and Advanced Computing) cluster. The numerical tasks are executed on up to 256 processors, in order to analyze scaling performances.

### 5.5.1 Validation

Radiative heat transfer in a two-dimensional complex geometry involving inclined boundaries, a semi-trapezoidal enclosure is considered a non-scattering homogeneous gray medium, as shown in Fig. 52a. Byunt *et al.* [19] numerically solved this problem using the finite volume method (FVM) with block-off procedures, while Zhang *et al.* [138] used the natural element method (NEM). The dimensions of Cartesian system of the trapezoidal enclosure are  $A(0,0)$ ,  $B(1,0)$ ,  $C(1,1)$ ,  $D(0.75,1)$ , and  $E(0,0.5)$ . The unit of all dimensions is assumed in meters. The medium temperature  $T_g$  is maintained at 1000 K, but all boundary walls' temperature is maintained at  $T_w = 0$  K. All the boundary walls are considered black. Three different absorption coefficients  $\kappa = 0.1 \text{ m}^{-1}$ ,  $\kappa = 1.0 \text{ m}^{-1}$ , and  $\kappa = 10 \text{ m}^{-1}$  are considered with an absorbing-emitting and non-scattered gray medium. This problem is solved using the saDG method with the polynomial order of  $p = p_x = p_s = 1$  in both space and angle. The total number of spatial elements is 800, as shown in Fig. 52b, with a uniform  $8 \times 8$  extruded mesh for angles  $\varphi$  and  $\mu$ .

Figure 53a illustrates the comparison between the non-dimensional radiative heat flux on the bottom wall and the exact solution. It can be seen that the current solutions are close to the exact solutions, and the absorption coefficients have a big effect on how the radiative heat flux is distributed on the bottom wall. When the absorption coefficient is relatively low, such as  $\kappa = 0.1 \text{ m}^{-1}$ , the radiative heat flux on the bottom wall is primarily influenced by the surface temperature. In other words, as the surface temperature increases, the radiative heat flux on the bottom wall also increases. However, when the wall temperatures are zero (i.e., there is no temperature gradient), the radiative heat flux is relatively weak. On the other hand, in optically

thick media where the absorption coefficient is high, the radiative heat flux on the bottom wall is mainly controlled by the medium temperature (denoted by  $T_g$ ). In this case, the radiative heat flux on the bottom wall is expected to be close to  $\sigma T_g^4$ , where  $\sigma$  is the Stefan-Boltzmann constant. This means that the temperature of the medium has the most effect on the heat flow from radiation in optically thick media.

On the other hand, Fig. 53b shows the non-dimensional radiative heat flux on the inclined wall (top wall) compared to the exact solution. The findings suggest that a jump in wall heat flux occurs at the junction of different parts of the inclined wall, attributed to the disparity in how wall heat flux is defined at the inclined boundary and upper wall. This behavior is more pronounced in cases with higher optical thickness of the medium, indicating increased opacity. In summary, the jump in wall heat flux is directly linked to the definition of wall heat flux and is more prominent in opaque mediums. Further research is needed to better understand and account for this behavior in practical applications.

### 5.5.2 Scaling performance

High-performance computing has two common notions of scalability, strong scaling, and weak scaling. Strong scaling is defined as how the solution time varies with the number of processors for a fixed total problem size. Weak scaling is defined as how the solution time varies with the number of processors for a fixed problem size per processor. For the DGRTE solver, strong scaling means setting up a problem and measuring the solution time with different processors; weak scaling means fixing the problem size for one processor (same number of slabs for each processor) and measuring the solution time with different numbers of processors. In this section, we evaluate the strong and weak scalability of the 2D saDG RTE solver with AD-DD methods, as well as the efficiency of the hybrid AD-DD method. The problem is considered in a quadrilateral enclosure with constant heat source boundary conditions as depicted in 54. The non-scattering medium is considered for the weak scaling study

of the AD method, while the anisotropic Rayleigh scattering medium with scattering albedo,  $\omega = \sigma_s/\beta = 0.5$ , is considered for the rest cases. The space and angle mesh resolution may vary based on the memory capacity of the nodes with the polynomial order  $p = 1$ .

These two scaling properties are measured by the parallel speedup  $S_p$ , and efficiency  $n_p$  is defined as,

$$S_p = \frac{t_0}{t_p} \quad (5.12)$$

$$E_p = \frac{S_p \times n_0}{n_p} \quad (5.13)$$

where  $t_0$  and  $t_p$  are the total run time required to solve the problem with  $n_0$  processors (as a reference) and  $n_p$  processors, respectively.

### Angular Decomposition

We analyze both weak and strong scaling performance using the AD method. The weak scaling is conducted with a constant number of elements of 5009 triangular spatial mesh with uniform  $4 \times 4$ ,  $8 \times 4$ ,  $8 \times 8$ ,  $16 \times 8$  and  $16 \times 16$  extruded mesh in  $\varphi$  and  $\mu$  for 16, 32, 64, 128, and 256 processors for AD as shown in Table 4. The numerical results are analyzed for weak scaling of the relative parallel efficiency based on the 16 processors. We track the total run time of each simulation. The results show an excellent parallel efficiency for higher AD processors, as shown in Table 4, where the parallel efficiency is around 1 for all cases. Scaling up to the maximum number of processors studied here is not severely hindered by the communication cost. Hence, it demonstrates that this approach should also scale to larger high-performance computing systems.

Strong scaling is measured by dividing the  $16 \times 16$  angular mesh into  $n_p$  subdomains with 3469 triangular elements in the spatial domain and solving the

problem with 16, 32, 64, 128, and 256 MPI processors. The temperature field is shown in Fig. 55. The strong scaling allows the workload per processor to be varied by changing the number of angular slabs assigned to each processor. As a result, inter-processor communication’s effect on efficiency and the number of iterations to achieve converged solutions are observed. The relationship between parallel speedup, efficiency, and the number of processors is shown in Table 5 for AD. Fig. 56a depicts the strong scaling performance of relative parallel speedup and relative parallel efficiency for total run time. The relative parallel speedup and efficiency are calculated based on processor 16. Excellent parallel performance is achieved with an efficiency greater than 1 by 32 processors. The relative parallel speedup of processor 256 increases to almost 8.5 times, and the relative parallel efficiency decreases to 0.531 than processor 16. One of the main reasons for the decreasing efficiency is the growing number of iterations when more MPI processors are employed, as shown in Table 5. The calculation of the scattering term involves utilizing solutions from the previous iteration to update the current solutions. As more processors are employed, more previous solutions are considered, as described in Equation 5.11, which results in more iterations. Fig. 56b shows the efficiency evaluated by average iteration time, which is better than the total run time when using more processors. However, aside from the number of iterations, the quantity of communication among the processors growing along with the number of processors also has a great impact on the efficiency.

### **Domain Decomposition**

The simulation for weak scaling runs with 88 spatial elements per processor with a uniform  $4 \times 4$  extruded mesh in angle  $\varphi$  and  $\mu$ . Table 6 illustrates the weak scaling performance for the DD. The table 6 shows the relative parallel efficiency based on the 16 processors. The efficiency degrades significantly when using a higher number of processors, where the 256-processor case shows very low efficiency. This drastic performance loss is largely attributed to the performance of MUMPS at the solution stage that solves Equation 5.9, as shown in Table 6 in the third column.

As  $n_p$  increases, the ratio of the matrix solving time  $t_p^{\mathbf{K}}$  and the total run time  $t_p$ , denoted as  $\alpha$ , gradually increases to 1, which means the solution stage dominates the total run time. The overhead associated with the interagency communication necessary to preserve the multiscale aspect of the simulation is the limitation of MUMPS [8] in weak scaling challenges. The 256-processor simulation has a total number of triangular mesh elements of 22528 and the overall number of degrees of freedom in space and angle is 4325376. As the number of processors increases, the quantity of interagency communication necessary to preserve the multiscale aspect of the simulation expands. This may result in a considerable rise in processing costs, which would ultimately restrict the simulation’s capacity to scale. Woźniak *et al.* [128] investigated the weak scaling performance using MUMPS. The results showed that the relative parallel efficiency dropped rapidly when the matrix was solved by a high number of processors.

The strong scaling performance for DD simulates by dividing a uniform angular extruded mesh of  $4 \times 4$  with 3469 triangular elements in a quadrilateral enclosure. Table 7 shows the strong scaling performance for the DD method. There is a tendency for the ratio  $\alpha$  increases with the growing number of processors. This is a similar trend to the weak scaling case because the solution stage dominates the total run time. The relative parallel efficiency decreases significantly when using a higher number of processors, as shown in figure 56c. This results from MUMPS’s load imbalance and high weight of communications being present in significant scaling difficulties as reported in [87]. A scenario where some processors are idle while others are significantly loaded might occur in many simulations where certain aspects of the issue are more computationally intensive than others. This might lead to a situation where the overall efficiency of the simulation is lowered, restricting the scalability of the simulation.

## Hybrid Angular-Domain Decomposition

In this section, the AD and DD methods are combined with  $n_p = 256$  processors. The number of processors used for the AD and DD is denoted as  $n_p^{\text{AD}}$  and  $n_p^{\text{DD}}$ , respectively. The total number of processors, thus, is equal to  $n_p = n_p^{\text{AD}} \times n_p^{\text{DD}}$ . In order to merge the two methods, the angular domain is sliced into  $l$  slabs and assigned evenly to  $n_p^{\text{AD}}$  processors, while the spatial domain breaks into  $n_p^{\text{DD}}$  subdomains. Hence, iteration is needed with AD involved. By using the DD approach, the computational domain is divided into smaller subdomains that can be processed independently by different processors. By combining this with an AD approach, which divides the computational work based on different directions or angles, the amount of interprocessor communication required is significantly reduced. This can lead to higher performance and efficiency, particularly in simulations with a large number of processors. The hybrid AD-DD method with a proper combination can achieve better scalability by reducing inter-processor communication overhead and load imbalance. Table 8 shows the performance for combined AD-DD with  $n_p = 256$ . The parallel speedup is calculated for AD-DD based on the  $256 \times 1$  AD-DD processors using equation 5.12. Two factors mainly affect the speedup, the number of iterations and the ratio of time,  $\alpha$ . By increasing the number of processors for DD, the number of iterations decreases, while  $\alpha$  increases. It is investigated that the  $32 \times 8$  AD-DD processors have the highest speedup 1.444 times compared with 256 single AD configurations and the highest among the other six AD-DD combinations. We used the best relative parallel speedup for running the numerical example in Section 5.5.3.

### 5.5.3 Square geometry with obstacles

The geometry is considered a square containing an array of nine obstacles with an isotropic incidence. These obstacles consist of circular and square shapes, respectively. Fig. 57 shows the computational domain. The distances shown in the figure are

in meter units. The participating medium is cold and Rayleigh scattering with a scattering albedo  $\omega = \sigma_s/\kappa = 0.5$  for the square geometry with circular and square obstacles. The left boundary of the square geometry is maintained at a constant temperature  $T_w = 1000$  K; the other boundaries are black and cold. 13059 triangular elements are generated in space for the problem. The elements in the angle are uniformly extruded mesh,  $128 \times 16$ , in  $\varphi$  and  $\mu$ . The polynomial order is  $p = 1$ . The problem was executed  $32 \times 8$  AD-DD processors.

Fig. 58 depicts the contour temperature plot of a square enclosure with nine circular and square obstacles, respectively. Compared to the circular and square obstacles, the circular one has better resolution than the square obstacle due to the edge of the geometry. Fig. 59 shows the contour temperature plot of the same numerical problem with a uniform  $16 \times 16$  angular discretization. The so-called “Rays effect” appears in this contour plot. To avoid such effects, the author suggests improving the angular extrusion, which was implemented in figure 58.

## 5.6 Conclusion

This paper employed the space-angle discontinuous Galerkin (saDG) method to solve the steady-state radiative transfer equation (RTE). The saDG method allows fully discretizing the computational domain in both space and angle. Two parallelization methods, angular decomposition (AD) and domain decomposition (DD), were applied. The AD method divides the angular domain into subdomains and solves each subdomain in parallel. This approach enables us to solve the entire domain iteratively. The DD method partitions the spatial domain into subdomains with ghost elements added to facilitate forming the global stiffness matrix in a distributed way. By using the distributed parallel linear solver, MUMPS, the global solution can be obtained. Both AD and DD techniques for solving the RTE were implemented in C++-software for the DG finite element discretization.

We demonstrated that our implementation of the AD method exhibits near-linear weak scaling on a substantial number of processors. Additionally, it shows decent efficiencies for strong scaling. In comparison, the AD method outperforms the DD method. One of the challenges associated with the DD method is its scalability on a large number of processors. This issue arises due to the significant proportion of time spent on solving matrices by MUMPS. When the number of processors increases, the complexity of communication and synchronization between them also grows, which can lead to reduced efficiency. In contrast, though more iterations are needed, the AD method's parallelization across angular subdomains mitigates these challenges by solving each subdomain individually, resulting in better overall performance and scaling properties. To further enhance efficiency, the hybrid AD-DD method, which combines the advantages of both the AD and DD methods, displayed superior performance compared to AD alone. This improved performance is achieved by employing an appropriate number of processors for AD and DD, striking a balance between the two techniques to optimize computation and communication overhead.

In conclusion, our implementation of the AD method demonstrates promising scaling properties and outperforms the DD method in terms of efficiency. Although the DD method faces challenges related to scalability, the hybrid AD-DD approach successfully combines the strengths of both methods. This synergy yields improved performance, making it a viable solution for large-scale parallel computing applications.

A valuable extension to this work would be to explore alternative matrix solvers for the Domain Decomposition (DD) method. The current implementation relies on MUMPS, which has scalability limitations and communication overhead when used with a large number of processors. By identifying and implementing a more efficient matrix solver, it is possible to further improve the performance and scaling properties of the DD method. This extension would involve a comprehensive analysis of available matrix solvers, considering factors such as their parallelization capabilities, communication overhead, and convergence rates. In addition, it may be beneficial to

investigate the potential for developing customized or hybrid solvers tailored to the specific requirements of the problem at hand. By enhancing the matrix solver within the DD method, the overall efficiency and scalability of the hybrid AD-DD approach could be further optimized, ultimately leading to more effective large-scale parallel computing applications.

## **Acknowledgement**

The authors acknowledge the High Performance Scientific Computing (HPSC) team at the University of Tennessee for providing computational resources and technical support for this work.

## Chapter 6

Space-Angle Discontinuous

Galerkin method for 2D Radiative  
Transfer Equation with Diffusively

and Specularly Reflective

Boundary Conditions

## 6.1 Abstract

A space-angle discontinuous Galerkin (saDG) method for solving the Radiative Transfer Equation (RTE) in arbitrary 2D domains is proposed. The space-angle domain is fully discretized by the DG method. An angular decomposition approach, resulting in an iterative solution process, is adopted to accelerate the solution and reduce memory usage. The performance of the method is analyzed in the square geometry with different types of boundary conditions. For nonscattering and open systems, the number of iterations each time increases by one with one additional reflective boundary. For other cases, we show that the number of iterations or convergence rate of the iterative method for the specular reflection problems is not only affected by the number of the reflective surfaces, but also by the scattering and extinction properties of the media. Uniformly and directionally diffuse reflective boundary conditions are compared in the same medium. Finally, the localization at the focal point of a parabolic reflector is studied.

## 6.2 Introduction

The radiative transfer equation (RTE) is a first-order integro-differential equation, which describes the radiative intensity propagating in the media that absorbs, emits, and scatters [88]. While there are a variety of numerical methods available, methods for space discretization coupled with angle discretization methods, such as the discrete ordinate method (DOM) [49, 114] and spherical harmonics method [46, 89, 15], are among the most extensively utilized strategies for the solution of radiative transfer problems in participating media. These methodologies decouple the angle domain and use mesh-based methods to solve the spatial domain. The DOM discretizes the angular domain into a discrete collection of ordinate directions, resulting in a set of spatial RTE equations for each particular direction. Finite difference, finite volume (FV) [31], or finite element methods (FEMs) [99] are used to solve the spatial domain.

Sums over the ordinate directions are used in place of integrals over the solid angles. The spherical harmonic method entails multiplying the RTE by various powers of the direction cosines of the intensity, resulting in a set of moment equations that must be solved to obtain the solution. The approach is named after the fact that the intensity is approximated by an orthogonal series of spherical harmonics.

Despite their popularity, the discrete ordinate and the spherical harmonic methods are not the only ways of discretizing the RTE in the angular domain. The discontinuous Galerkin (DG) finite element method (FEM) is one of the most popular grid-based numerical methods for solving the RTE due to its high order accuracy and flexibility in mesh adaptivity. The basis functions used in the DG method are discontinuous across element interfaces; accordingly, the jump condition between interior traces of the solution and the so-called numerical flux is weakly enforced on the interface boundaries. The space-angle discontinuous Galerkin (saDG) methods that fully discretize the spatial and angular domain are especially suitable for the RTE since the evolution of solution along characteristics can be strongly discontinuous when there are local radiation sources, incidence radiation enters from the boundary surfaces, or upon reflection from reflective boundaries.

Gao and Zhao [50, 51] used a discontinuous Galerkin (DG) in space and a piecewise constant finite element method in angle. Olbrant *et al.* [91] employed an entropy-based model to solve in the angular domain while using a DG discretization in space. However, just like in the spatial domain, continuous approaches might fail when discontinuities arise in angular space or domain interfaces. As a result, over the last few years, Kophazi *et al.* [73] and Kitzmann *et al.* [37] have devised space-angle DG algorithms to handle this problem in both space and angle. The Boltzmann transport equation, which Kophazi implemented, is a simplified equation without a phase function. Kitzmann solved the RTE with spherical symmetry, which is a more complicated variant of the RTE due to the addition of a derivative with regard to the polar angle. Sun *et al.* [112] proposed a spectral element method to discretize the spatial and angular domains, while adopting the DG scheme in space to smoothen

the oscillations induced by the spatial discontinuity of radiative intensity. Previous works have shown that the space-angle DG method can be applied to solving the RTEs with high order of accuracy and in parallel with the domain decomposition (DD) and angular decomposition (AD) methods [118, 119, 124].

Reflections on surfaces include three types of reflection: specular reflection, uniform diffuse reflection, and directional diffuse reflection, as shown in Fig. 60. Specular reflection is mainly found on polished surfaces, while diffuse reflection dominates on rough surfaces. The surface roughness mainly determines whether diffuse reflection is uniform or directional. Although diffuse reflection is frequently discussed in the literature, specular reflection [102, 77, 79] is less frequently discussed due to the difficulty in its numerical treatment. When there are specularly reflecting boundaries, the use of the discrete ordinates method can be difficult, as seen in the following example. The direction of a specularly reflected beam does not coincide with any of the directions of the discrete ordinate set; since there is no analytic quadrature scheme for integrating the reflected wave in this case, it is often impossible to predict how intense the specularly reflected beam is. As a result, some form of interpolation is required, which is not straightforward on the sphere. This problem is exacerbated if the angle between the directions of the reflected ray and the reflecting plane is too small. This results from the fact that only half of the discrete ordinate set that is inside the computational domain at the boundary can be used to predict the reflected intensities, and the other half is out of the domain. Therefore, interpolation cannot be used to determine the intensity of this beam in this situation and extrapolation is necessary using half of the discrete ordinate set available. In addition to the discrete ordinate method, Castro and Trelles [21] used the FEM in space and angle to solve the radiative transfer problems in a parabolic concentrator with specularly reflective boundary conditions. However, therein the maximum angular discretization order is  $p = 1$ , that is only piecewise linear solutions are supported in angle. Clarke *et al.* [27] applied the saDG method to the simulation of plane-parallel radiative transfer

problems, with higher order polynomial in both space and angle, with specular boundary condition.

The saDG method is very suitable for solving the RTE with reflective boundary conditions because,

1. The saDG method robustly handles solution discontinuities both in space and angle, especially for the problems when a beam specularly reflects from a surface;
2. Accuracy can be easily improved in the angular domain, especially, when a directional solution is dominant, by applying finer element sizes (*h*-refinement) or increasing the order (*p*-enrichment) in angle.

In this paper, the 2D RTE problems with reflective boundary conditions are solved by the iterative saDG solver in parallel. The formulations of the DG method for the steady RTE with specularly and diffusely reflective boundary conditions are presented in §6.3. The implementations of the saDG solver for angular integration and reflective boundary conditions are described in §6.4. Next, several numerical examples of a square box and a parabolic reflector are presented in §6.5 with reflective boundary conditions. Final conclusions are drawn in §6.6.

## 6.3 Formulation

### 6.3.1 2D RTE & its boundary conditions

For a monochromatic wavelength, the steady radiative transfer equation (RTE) is written as,

$$\hat{\mathbf{s}} \cdot \nabla I(\mathbf{x}, \hat{\mathbf{s}}) + \beta I(\mathbf{x}, \hat{\mathbf{s}}) = \kappa I_b(\mathbf{x}) + \frac{\sigma_s}{4\pi} \oint_{4\pi} I(\mathbf{x}, \hat{\mathbf{s}}') \Phi(\hat{\mathbf{s}}, \hat{\mathbf{s}}') ds' + S(\mathbf{x}, \hat{\mathbf{s}}), \quad (6.1)$$

where  $I$  is the radiative intensity in the spatial domain  $\Omega_{\mathbf{x}}$  along the solid angle direction  $\hat{\mathbf{s}}$ . The extinction coefficient  $\beta = \kappa + \sigma_s$  is the sum of the absorption

coefficient  $\kappa$  and the scattering coefficient  $\sigma_s$ .  $\Phi(\hat{\mathbf{s}}, \hat{\mathbf{s}}')$  is the scattering phase function. The spatial-dependent black-body radiative intensity is  $I_b$ . All quantities are also a function of the wavelength, which is omitted for brevity.

The intensity, leaving a wall into a specified direction, is determined by its surface properties. In applications considered here, both “ideal” and “nonideal” opaque surfaces are taken into account. The ideal surface is assumed to be diffusely emitting and diffusely and/or specularly reflecting (with the magnitude of reflectance independent of the incoming direction). The nonideal surface, on the other hand, is when arbitrary directional reflection behavior is encountered. In this case, the reflectance is determined by an integral equation over all the incoming directions.

For the ideal surface, the boundary condition is [88],

$$I(\mathbf{x}_w, \hat{\mathbf{s}}) = \bar{I}(\mathbf{x}_w, \hat{\mathbf{s}}) + \frac{\rho_d(\mathbf{x}_w)}{\pi} \int_{\hat{\mathbf{s}}' \cdot \mathbf{n} > 0} I(\mathbf{x}_w, \hat{\mathbf{s}}') \hat{\mathbf{s}}' \cdot \mathbf{n} \, ds' + \rho_s(\mathbf{x}_w) I(\mathbf{x}_w, \hat{\mathbf{s}}_s), \quad (6.2)$$

where the subscript  $w$  refers to wall and indicates the spatial boundary of the domain,  $\rho_d$  and  $\rho_s$  are the diffuse and specular reflectance, respectively. The first term on the RHS of Eqn. 6.2 is the diffuse emission. The second RHS term is the *uniform diffuse reflection* component, where  $\rho_d$  is the diffuse reflectance,  $\mathbf{n}$  is the local outward surface normal and  $\hat{\mathbf{s}}' \cdot \mathbf{n} = \cos \gamma'$  is the minus cosine of the angle between any incoming direction  $\hat{\mathbf{s}}'$  and the surface normal, as depicted in Fig. 61. The third term is the specularly reflective component, where  $\hat{\mathbf{s}}_s$  is the specular direction, defined as the direction from which a light beam must hit the surface in order to travel into the direction of  $\hat{\mathbf{s}}$  after a specular reflection. From Fig. 61, this direction is,

$$\hat{\mathbf{s}}_s = \hat{\mathbf{s}} - 2(\hat{\mathbf{s}} \cdot \mathbf{n})\mathbf{n}. \quad (6.3)$$

As a result, the outgoing intensity is not explicitly known, but is related to the incoming intensity.

Reflection from a surface with nonideal radiative properties is governed by the bidirectional function,  $\rho''(\mathbf{x}, \hat{\mathbf{s}}, \hat{\mathbf{s}}')$ , so that

$$I(\mathbf{x}_w, \hat{\mathbf{s}}) = \bar{I}(\mathbf{x}_w, \hat{\mathbf{s}}) + \int_{\hat{\mathbf{s}}' \cdot \mathbf{n} > 0} \rho''(\mathbf{x}_w, \hat{\mathbf{s}}, \hat{\mathbf{s}}') I(\mathbf{x}_w, \hat{\mathbf{s}}') \hat{\mathbf{s}}' \cdot \mathbf{n} ds'. \quad (6.4)$$

The second term on the RHS is called the *directional diffuse reflection*. If the surface reflects uniformly diffusely,  $\rho'' = \rho_d/\pi$ . For specular reflection, the bidirectional function becomes a delta function, so that the above equation is reduced to Eqn. 6.2. In most cases when the bidirectional function is introduced, the field is diffused to the hemisphere but may have a directional and nonuniform character, which is called the directional diffuse.

### 6.3.2 Space-angle DG discretization

The governing radiative transfer equations Eqn. 6.1 and reflective boundary conditions Eqn. 6.2 or Eqn. 6.3 in semi-transparent media cannot be solved analytically in most situations. The DG method is used to get a space-angle approximation of the radiative intensity.

The element extrusion technique is utilized to define the space-angle mesh  $\Omega$ . In this technique, the spatial mesh  $\Omega_{\mathbf{x}}$  is first discretized by simplicial elements. The angular mesh is extruded from the spatial mesh  $\Omega_{\mathbf{x}}$ . Normally, the solid angle direction has two independent angle variables  $\mu$  and  $\varphi$ , where  $\mu$  is the cosine of the polar angle  $\theta$ , and  $\varphi$  is the azimuthal angle. The extrusion for the solid angle, thus, needs to be done twice. For example, Fig. 62 shows the extrusion process of a space-angle mesh extruded from a 2D spatial mesh in Cartesian coordinates. The element  $\mathcal{Q}$  is first extruded in  $\mu$  from the spatial element  $\mathcal{Q}_{xy}$ , and then, extruded in  $\varphi$  from the former extrusion to achieve the space-angle element. Since the four-dimensional element cannot be illustrated, in the last subfigure, the  $x$  axis represents the 2D geometry of the element in space.

In a DG formulation, residuals (errors) must be specified both in the interior and on the boundary of elements. The weighted residual statement (WRS) is formed by multiplying the residuals inside and on the boundary of elements by the weight function  $\hat{I}$ . For an arbitrary space-angle element  $\mathcal{Q} \in \Omega$ , the WRS is,

$$\int_{\mathcal{Q}^l} \hat{I} \mathcal{R}_{\mathcal{Q}^l} dV + \int_{\partial \mathcal{Q}^l} \hat{I} \mathcal{R}_{\partial \mathcal{Q}^l} dA = 0, \quad (6.5)$$

where  $\mathcal{Q}$  is the element and  $\partial \mathcal{Q}$  is the element boundary. The interior residual  $\mathcal{R}_{\mathcal{Q}^l}$  corresponding to Eqn. 6.1 is,

$$\begin{aligned} \mathcal{R}_{\mathcal{Q}^l} = & \hat{\mathbf{s}} \cdot \nabla I^h(\mathbf{x}, \hat{\mathbf{s}}) + \beta I^h(\mathbf{x}, \hat{\mathbf{s}}) - \kappa I_b(\mathbf{x}) \\ & - \frac{\sigma_s}{4\pi} \oint_{4\pi} I^h(\mathbf{x}, \hat{\mathbf{s}}') \Phi(\hat{\mathbf{s}}, \hat{\mathbf{s}}') (\hat{\mathbf{s}}, \hat{\mathbf{s}}') ds' - S(\mathbf{x}, \hat{\mathbf{s}}). \end{aligned} \quad (6.6)$$

For DG methods, the continuity of solutions across element boundaries is satisfied by weakly satisfying the jump between the interior trace of intensity,  $I^h$ , and its target flux  $I^*$ ; this relaxes the continuity constraints of continuous finite element methods. Correspondingly, for the RTE, the residual on the element boundary  $\partial \mathcal{Q}^l$  is expressed as,

$$\mathcal{R}_{\partial \mathcal{Q}^l} = \hat{\mathbf{s}} \cdot \mathbf{n} (I^* - I^h), \quad (6.7)$$

The weight function  $\hat{I}$  and discrete solution  $I^h$  are polynomials of order  $p$  in both space and angle, interpolated with respect to a local coordinate system. The target value  $I^*$  corresponds to the upstream value along the direction of wave propagation where  $\hat{\mathbf{s}} \cdot \mathbf{n} < 0$  is the inflow direction and  $\hat{\mathbf{s}} \cdot \mathbf{n} > 0$  is the outflow direction. The reader is referred to [119] for more details on the definition of the target value and saDG formulation for RTEs.

The diffuse and specular reflection boundary conditions are implemented differently. For the diffuse reflection boundary condition, the integral term in Eqn. 6.2 is calculated using Gauss quadrature. For the specular reflection boundary condition,

the first step is to find the corresponding element of the specular direction. By interpolating the solution within the element in the specular direction, the reflective intensity is then obtained.

## 6.4 Implementation

Direct assembly of the whole system may result in a very large stiffness matrix that is difficult to solve, due to the couplings in the angular domain from the scattering integral and/or reflective boundary conditions (BCs). Specifically, the scattering integral operator in Eqn. 6.5 for element  $\mathcal{Q}$  leads to interacting with all angular elements extruded from the same spatial point. For example, the extrusion of the spatial element  $\mathcal{Q}$  in Fig. 63(a), results in 16 elements in the angular domain. The angular grid corresponding to quadrature point  $\mathcal{Q}_3$  is shown in Fig. 63(b). Similarly, for the reflective BCs, the element inflow boundaries ( $\hat{s} \cdot \mathbf{n} < 0$ ) are coupled with element outflow boundaries that contain the incidence angle. This can be seen in Fig. 64. For the diffusely reflective BC, the elements containing red solid circles are coupled with the elements containing blue hollow circles, depicted in Fig. 64(b). For the specular reflective BC, the element containing the pointed red solid circle is coupled with the element containing the pointed red dash-dot circle in Fig. 64(c). Because of the couplings in angle, forming and storing the entire stiffness can be computationally expensive and require extensive memory resources as the system size increases.

To overcome the issue, we have developed an angular decomposition (AD) method to decouple the angular domain. We refer the reader to our previous paper [124] for the details of the AD method. In short, decoupling of the angular elements replaces the current discrete solutions  $I^h$  in angle coupling terms (scattering in the domain and reflection on the reflective boundaries) with their corresponding values from the previous iteration. Thus, the coupling terms are considered as source terms and each angular domain is solved with a much smaller and local stiffness matrix. The iterative

method continues until the change in the solution between two successive iterations is sufficiently small. The AD method results in small matrix solves. Moreover, it is highly parallelizable, since the slab calculations are independent. Fig. 63 and 64 show examples of coupling in 16 extruded elements (square regions) in angles  $\varphi$  and  $\mu$  at a spatial point. The angular domain is divided into 4 slabs (larger red and blue boxes) so that each slab contains 4 elements. The red and blue dots inside the elements are the quadrature points. Using this example, the following subsections describe the implementation of the decoupled scattering integral term and reflective BCs, as well as the iterative parallel algorithm. Due to the similarities of the solution procedure for the other three slabs, only the solution process for slab 1 (in red) is provided in detail.

### 6.4.1 Decoupling of scattering integral terms

The calculations of the scattering integral term in slab 1 and other slabs by the AD method can be broken into the following steps (see Fig. 63),

1. Initialize the intensity at all quadrature points (in red and blue quadrature points).
2. For all the quadrature points in slab 1, the integration is performed over the solid red quadrature points. These values contribute to the local stiffness matrix since the angles in slab 1 are still coupled. A similar process is repeated for other slabs.
3. For all the quadrature points in slab 1, the integration is performed over the hollow blue quadrature points in other slabs. In this case, the integration is treated as the source term because the intensity at hollow blue points is known, which is initialized in step (1) or updated in step (4). Hence, the hollow blue points contribute to the right-hand side (RHS), *i.e.*, the force vector, for the

equation of slab 1. A similar process for updating the RHS is performed for the other slabs.

4. The solution of each slab is calculated after the assembly stage. The intensity is then updated at all the quadrature points (in red points after the solution of slab 1, and blue points after the solution of each corresponding slab).
5. Repeat steps (3) and (4), until the solutions are converged.

### 6.4.2 Reflective boundary conditions

The procedure of calculations of reflective BCs is similar to that of the scattering integral operator, with the difference that now the sample spatial quadrature point  $\partial\mathcal{Q}_2$  resides on the boundary of element  $\mathcal{Q}$  in Fig. 64(a). The spatial normal  $\mathbf{n}$ , the slant line in Fig. 64(b) and (c), divides the angular domain into reflected and incident angles.

The angular coupling of the diffusely reflective BC corresponds to the second RHS term in Eqn. 6.2 (uniform diffuse reflection) or the second RHS term in Eqn. 6.4 (directional diffuse reflection). The procedure is discussed below for all slabs and is depicted for slab 1 in Fig. 64(b)

1. For each slab, loop over all the quadrature points that are in the incidence angle ( $\mathbf{s} \cdot \mathbf{n} > 0$ ) and initialize their intensity. These points are shown by blue hollow dots in Fig. 64(b).
2. For all quadrature points in reflected angle in slab 1, the integration is performed over the blue dots. The calculation refers to Eqn. 6.2 or 6.4 based on whether uniform or directional diffuse reflection is considered.
3. Update the solutions at the incidence angle points after the assembly stage.
4. Repeat steps (2) and (3), until the solution is converged.

The steps for the specular reflection condition (the third RHS term in Eqn. 6.2) are discussed below and depicted for slab 1 in Fig. 64(c),

1. For any reflection point in a slab, the corresponding incident point is determined using Eqn. 6.3. This is shown for a quadrature point in slab 1 (pointed to solid red circle) in Fig. 64(c), where the incident point (pointed to dash-dot red circle) and its corresponding slab are determined.
2. The reflected intensity is calculated by the intensity at the incidence angle and the specular reflectance.
3. Update solutions at the incident angle (red dash-dot circle).
4. Repeat steps (2) and (3), until the solution is converged.

### 6.4.3 Summary of parallel process

The steps taken in the iterative parallel process can be summarized as follows,

1. Divide the angular domain into  $m$  slabs and assign to  $n$  processors. In our implementation,  $m$  is an integer multiple of  $n$ .
2. Initialize all the quadrature points in the domain and on the reflective boundaries.
3. Assemble the slab level stiffness matrix and the RHS, except for the across slabs coupling (reflective BCs and scattering) terms. The assembled stiffness matrix is stored in its allocated processor.
4. Solve the system of the linear equations with the computed stiffness and the current RHS. Then, update the solutions at all quadrature points.
5. Assemble the inter-slab and inter-processor coupling (reflective BCs and scattering) terms and update the local RHS.

6. Repeat steps (4) and (5), until the solution is converged by measuring the relative error,

$$e_{\text{rel}}^k = \left\| \frac{I^k - I^{k-1}}{I^k} \right\|_{\infty} = \max_j \left| \frac{I_j^k - I_j^{k-1}}{I_j^k} \right|, \quad (6.8)$$

where  $j$  is the index of the quadrature point over the whole domain. The process stops at iteration  $k$ , when the error  $e_{\text{rel}}^k$  is less than a convergence tolerance,  $\epsilon = 1 \times 10^{-10}$ .

## 6.5 Numerical examples

In this section, the examples of 2D RTE in participating media with reflective boundary conditions are presented in a square domain and a parabolic reflector. For the square geometry, first the reflections inside the domain from an incident wave entering the domain on the right edge are considered. This aims to compare different types of reflective BCs, specular, uniform diffuse, and directional diffuse. The effect of the number of reflective faces on the solution and convergence properties of the iterative method are also studied in this example. Second, an internal source term is considered for the square geometry. The last example shows the focusing effect in a parabolic reflector.

### 6.5.1 Square box

Consider the radiative problems in a  $1 \times 1$  square box with the following boundary conditions, as depicted in Fig. 65. The red lines represent reflective boundaries and the other boundaries represent vacuum, *i.e.*,  $I_w = 0$ . We followed the naming convention for the 6 cases from [9]. For the cases in the first row in Fig. 65, the wave inside the domain can escape, and thus they are “open” systems. The cases in the second row are “closed” systems, as the wave can get trapped either in vertical or all directions.

## Prescribed incidence on the left boundary

Fig. 66 shows the problem set-up for this example. A prescribed beam is entering through the left boundary of the box, with an incidence angle of  $\theta_{\text{inc}} = -\frac{\pi}{4}$ , such that its radiance is,

$$I_{\text{inc}}(x, y, \varphi, \mu) \Big|_{x=0, y \in [0.4, 0.6], \varphi = -\frac{\pi}{4}} = 1.$$

In the following sections, specular, uniform diffuse, and directional diffuse reflection examples are considered for this problem.

**Specular reflection** The purpose of this example is to investigate how the number of reflective boundaries, *i.e.*, form of domain enclosure, affects the solution and efficiency of the iterative method. Four of six cases of boundary conditions listed in Fig. 65 are considered: (1) free box, (2) three free side, (3) corner, (5) single free side. These cases correspond to the number of reflective boundaries of 0, 1, 2, and 3, respectively. All the reflective boundaries are specularly reflective, *i.e.*,  $\rho_s = 1$  in Eqn. 6.2. Each case is investigated for five single-scattering albedos  $\omega_s = 0, 0.25, 0.5, 0.75, 1$ , where  $\omega_s$  is defined as,

$$\omega_s = \frac{\sigma_s}{\beta}. \quad (6.9)$$

Since the extinction coefficient inside the medium is  $\beta = 1$ , the corresponding scattering coefficient is  $\sigma_s = \omega_s$ . The Rayleigh phase function is adopted for the scattering media, expressed as [88],

$$\Phi(\mu, \varphi, \mu', \varphi') = \frac{3}{4} \left\{ 1 + \left[ \sqrt{(1 - \mu^2)(1 - \mu'^2)} \cos(\varphi - \varphi') + \mu\mu' \right]^2 \right\}. \quad (6.10)$$

Fig. 67 shows the adaptive mesh with 3730 triangles. A uniform  $12 \times 6$  extruded mesh is used for angles  $\varphi$  and  $\mu$ . The polynomial order for the discrete solution is  $p = 1$  in both space and angle directions.

The results are presented for the space-dependent angular integrated density function,

$$D(\mathbf{x}) = \int_{4\pi} I(\mathbf{x}, \hat{\mathbf{s}}) ds. \quad (6.11)$$

Fig. 68 shows the results for the four boundary condition cases (in rows) and albedo values,  $\omega_s = 0, 0.5$  and  $1$  (in columns), respectively. In the zero scattering medium ( $\omega_s = 0$ ), the overall density  $D$  of the beam decreases along the path line, and  $D$  remains zero elsewhere in the box. In contrast, for the scattering media, the density  $D$  decreases less along the path line than the zero scattering media. As more reflective boundaries are used, the density  $D$  further increases in the domain and outside of the ray paths.

The number of iterations for these cases are listed in Table 9. For zero scattering cases, the number of iterations grows only 1 step for an additional specular reflection boundary. However, for  $\omega_s = 1$  case, the number of iterations is almost doubling with any additional reflective boundary. The evolution of the iteration error  $e^n(I)$  for the scattering cases is presented in Fig. 69 in the log-log scale. To get the average rate of convergence  $\alpha$ , the slope of the curves in this figure are computed after the stage that the asymptotic rate is attained, *i.e.*, past the first few iterations. Fig. 70 shows the number of specularly reflective boundaries with respect to the average convergence rate  $\alpha$  in  $\log_2$  scale. Interestingly, the slope of the convergence rate is close to its scattering albedo when the scattering is strong ( $\omega_s \geq 0.5$ ), while for small scattering albedo, the slope remains at 0.5.

**Uniform diffuse reflection** The uniform diffuse reflection case is investigated for three albedos  $\omega_s = 0, 0.5$ , and  $1$ . Only case (2), the three free side case, in Fig. 65 is considered for this problem, where the bottom boundary is uniformly diffuse reflective, and the right and top boundaries are vacuum. Other properties and spatial mesh remain the same as in the specular reflection example, but the angular mesh is

further refined to the resolution  $50 \times 10$ . The contour plots of the intensity density  $D$  for  $\omega_s = 0, 0.5, 1$  are shown in Fig. 71, from left to right, respectively. As the albedo increases, the overall values of the intensity field also increase.

**Directional diffuse reflection** The directional diffuse reflection case is investigated for the albedo  $\omega_s = 0$ . The bottom boundary is considered as the directional diffuse and similar to the previous example, the right and top boundaries are vacuum (case (2) in Fig. 65). The difference between uniform and directional diffuse is that the latter is governed by the bidirectional function in the angular integration. In this case, the bidirectional reflection function of the Phong mode [95] is adopted,

$$\rho''(\hat{\mathbf{s}}, \hat{\mathbf{s}}') = \frac{a_p + 2}{2\pi} \cos^{a_p} \Theta, \quad (6.12)$$

where the coefficient  $a_p = 2a_b^{-2} - 2$  is related to the mean value of the microfacets slope  $a_b \in (0, 1]$ ,  $\Theta$  is the angle between  $\mathbf{n}$  and  $1/2(\hat{\mathbf{s}} + \hat{\mathbf{s}}')$ , as shown in Fig. 61. When  $a_b \rightarrow 0$ , the surface is smooth so that the specular reflection is dominant. As  $a_b$  grows, the surface becomes rougher. When  $a_b = 1$ , the mean microfacets slope is  $45^\circ$ . The bidirectional diffuse function is a constant, which indicates the uniform diffuse condition. Fig. 72 shows the contour plots of the radiative density for the three mean values of the microfacets, corresponding to  $a_b = 0.1, 0.2, 0.3$ . As can be seen, the rougher the surface (the larger  $a_b$ ), the more diffusive the reflection.

### Gaussian point source

A Gaussian point source is applied in a  $1 \times 1$  square box that shines towards all angle directions,

$$S(x, y) = 10e^{-1000[(x-0.55)^2 + (y-0.6)^2]}.$$

The medium is cold and non-scattering. The extinction coefficient is  $\beta = 1.0$ . All the six boundary cases in Fig. 65 are considered. The free box, three free side, and corner cases can be categorized as the open system, where the propagating wave

eventually goes out through the vacuum boundaries. These three cases correspond to open space, half space, and quarter of space setups, respectively. The waveguide, single free side, and closed box cases are close systems, in which some fraction or all the intensity bounces between the boundaries.

The spatial mesh contains 11138 triangles, refined around the location of the point source is shown in Fig. 73. A uniform  $32 \times 16$  extruded mesh is used for angles  $\varphi$  and  $\mu$ . The polynomial order for the discrete solution is  $p = 1$ . The RTE solver is the same as the previous example. However, the iteration error is relaxed due to the slow convergence rates for the closed systems. Similar to the definition in Eqn. 6.8, the error indicator measures the error between prior and current solution. However, we used an absolute value to relax the convergence condition; the absolute error is given by,

$$e_{\text{abs}}^k = \left\| \frac{I^k - I^{k-1}}{\bar{I}} \right\|_{\infty} = \max_j \left| \frac{I_j^k - I_j^{k-1}}{\bar{I}} \right|,$$

where  $j$  is the index of the quadrature point, and  $\bar{I}$  a scale number for the intensity. For this problem,  $\bar{I} = \max S(x, y) = 10$ .

The results are shown in Fig. 74 in the first and third rows. To better observe the reflected waves, the free box solution is subtracted from all the other solutions, as shown in the second and fourth rows. Because the point source is off-center, the reflected intensity is stronger at the top right corner in the closed box. The subtracted solutions show the “ray effects”. These ray effects can be mitigated by increasing the solution resolution in angle.

The number of iterations for the six cases is listed in the second row of Table 10. For the open systems, the number of iterations is equal to the number of reflective boundaries. Each iteration calculates the next reflected propagation of intensity. For the close systems, the number of iterations is positively correlated to the number of reflective boundaries. The average convergence rates for the close systems are measured and listed in the third row of Table 10. The convergence rate for the waveguide is more than twice higher as for the closed box. The single free side

converges slower than the waveguide, but still, faster than the closed box. This is because the internal source gets reflected in the box and can not escape for the all-reflection case. For the close system, the number of iterations is also related to the extinction along the geometry path,  $s$ , through which the beam has traveled, given by [88],

$$\int_0^s \beta ds = \ln \frac{I_0}{I(s)},$$

where  $I_0$  is measured at the initial point. In this case, the initial point is at the center of the source point, so that  $I_0 = S(0.55, 0.6) = \bar{I}$ . The intensity energy travels to the boundary and gets reflected between mirrors and eventually dies out along the shortest path, where  $I(s) \approx \epsilon = 1 \times 10^{-10}$ . So that the approximated travel distance is  $s \approx 23$ , which implies that the bouncing intensity gets reflected at most 23 times. This number have the same order of magnitude of the number of iterations for the closed systems. To better demonstrate this relation, the closed box case is solved for  $\kappa = 2$  and 3. The corresponding number of iterations are 17 and 11, indicating that the number of iterations is inversely proportional to the extinction coefficient for the close systems.

### 6.5.2 Parabolic reflector

A parabolic reflector opening with a length between the focus and the vertex equal to  $1/3$  is considered. The height and width are 2 and 0.75, respectively. The incidence entering perpendicularly from the top boundary is,

$$I_{\text{inc}}(x, y, \varphi, \mu) \Big|_{y=0.75, \varphi=-\frac{\pi}{2}} = 1.$$

The curved boundary is specularly reflective, where  $\rho_s = 1$ . The spatial mesh contains 9110 triangles, refined around the focal point as shown in Fig. 75. A uniform  $10 \times 10$  extruded mesh is used for angles  $\varphi$  and  $\mu$ . The polynomial order for the discrete solution is  $p_{\mathbf{x}} = 1$  in space and  $p_{\mathbf{s}} = 2$  in angle. The medium inside the reflector is

cold and non-scattering. The extinction coefficient is  $\beta = 1.0$ . The contour plot for the radiative density is shown in Fig. 76. The correct position for the highest value of the radiative density at the focal point of the parabolic reflector is obtained. The radius of the localization is about 0.1.

## 6.6 Conclusions

We presented a space-angle discontinuous Galerkin (saDG) method for the solution of the RTE with specularly and diffusely reflective boundary conditions. In our weighted residual statement, the element continuity constraint is weakly enforced using the target value  $I^*$ . Consistent with the form of the solution for the RTE, this approach supports discontinuity in both space and angle. For the scattering media, the elements are coupled in angle directions. To avoid large computational costs and memory usage, an iterative method is used to reduce the global stiffness matrix size. The interpolation of the solution in angle by the saDG method simplifies the formulating and greatly improves the accuracy of the diffuse and specular reflections with fine mesh and high-order polynomials in angle. Finally, in addition to the uniformly diffuse reflection, the bidirectional reflection function is introduced to simulate the surface roughness by evaluating the mean value of the slope of the microfacets.

There are some key findings of the specularly reflective boundary condition investigated in Section 6.5.1,

1. For *non-scattering* media in *open systems*, the number of iterations is proportional to the number of reflected rays.
2. Otherwise, the solution is an iterative process where the convergence rate gets worse as the reflective surfaces or albedo increases, as explained through 2 examples,

- (a) In *scattering* media, it is shown that the convergence rate reduces by a factor from about 0.5 to 1 (depending on albedo) with every one increase to the number of reflective boundaries.
- (b) In closed systems, The convergence rate drops from 1.6 to 0.72 as the system gets more closed from bottom-top to all cases. Besides, the number of iterations is inversely proportional to the extinction coefficient.

These findings are similar to [9] for an iterative solver for the Helmholtz equation. Therein, the convergence rate of closed and open systems was very different [9] too. Moreover, the results of the point source example reveal the “ray effect”, which is a non-physical phenomenon, especially prevalent for the discrete ordinate method.

# Chapter 7

## Summary and Conclusions

We presented a space-angle discontinuous Galerkin (saDG) method for solving the radiative transfer equation (RTE). The objective-oriented design of the software allowed us to apply the saDG approach to a variety of RTEs with considerable ease, including 1x1s, 1x2s, and 2x2s. For low-dimensional problems, the direct solver can be competent in getting high-order accuracy solutions. However, for high-dimensional problems, the direct solver is slow in solution time and takes high memory usage that may not fit in the computer RAM memory. Therefore, we applied the angular decomposition (AD) method to the iterative solver to increase the run-time efficiency and reduce memory usage. For large-scale problems, the parallel solver was developed based on AD and domain decomposition (DD) methods. Finally, the reflective boundary conditions were applied to 2-D Cartesian radiative transfer problems.

Our work results in new design methods of solving the steady-state radiative transfer equation in multi-dimensions by spatial and angular discontinuous Galerkin finite element method. Besides, it is expected to be applied to all kinds of numerical applications of transport equations, including neutron transport, Boltzmann radiative transfer, *etc.* In addition, our multi-dimensional meshing tool is able to create elements in many other problems involving high dimensionality, e.g., transport equations, electromagnetics, and space-time methods. Meanwhile, our work presents a parallel framework for mesh-based methods, such as finite element methods and finite volume methods, to improve computational efficiency.

The research work presented in this thesis is a collaborative effort, and my individual contributions to each chapter are outlined below:

- **Chapter 2:** The development of the 1D saDG RTE solver was a joint effort by Dr. Reza Abedi, Dr. Philip Clarke, and myself. I was responsible for conducting the numerical examples and documenting them in the chapter.
- **Chapter 3:** I led the expansion of the saDG RTE solver to address 1D spatial and 2D angular RTE problems, and I was the primary author of this chapter, ensuring the content was thoroughly explained and well-structured.

- **Chapter 4:** I conceived the idea of enhancing the solver’s efficiency and memory usage through the implementation of an iterative method, and I was the main writer for this chapter. I focused on providing a clear and detailed explanation of the method and its benefits.
- **Chapter 5:** I devised the angular and domain decomposition methods and carried out their implementation. My writing responsibilities included the Formulation and Implementation sections, and I also contributed to the editing process, refining the text for clarity and coherence.
- **Chapter 6:** I took the lead in implementing the reflective boundary condition and served as the primary author for this chapter, ensuring a comprehensive presentation of the concept and its application.

We will focus on three objectives in our future work. First, piece-wise constant and variable refractive indices in the media will be considered. This will allow us to study more complex media and metamaterials. Next, we will further improve the efficiency and accuracy of the solver. In this case, the adaptive mesh generation technique will be applied to the parallel saDG solver. The compact stencil size makes the resulting method simple to parallelize while the local nature of the discontinuous Galerkin approximation makes  $hp$ -adaptive refinement natural to implement. Last but not least, we will mitigate the “ray effect” observed in the study when the mesh in the angular domain is coarse. The multigrid method will be adopted in the angular domain to eliminate the “ray effect”.

# Bibliography

- [1] Abdel Krim, M. S., Attia, M. T., and Madkour, M. A. (1991). Application of the superconvergence properties of the Galerkin approximation to radiative transfer. *Astrophysics and Space Science*, 186(1):89–99. [11](#), [34](#), [55](#)
- [2] Abedi, R., Chung, S.-H., Erickson, J., Fan, Y., Garland, M., Guoy, D., Haber, R., Sullivan, J. M., Thite, S., and Zhou, Y. (2004). Spacetime meshing with adaptive refinement and coarsening. In *Twentieth Annual Symposium on Computational Geometry (SCG '04)*, Brooklyn, New York, USA. [76](#)
- [3] Abedi, R. and Haber, R. B. (2014). Riemann solutions and spacetime discontinuous Galerkin method for linear elastodynamic contact. *Computer Methods in Applied Mechanics and Engineering*, 270:150–77. [44](#)
- [4] Abedi, R. and Haber, R. B. (2018). Spacetime simulation of dynamic fracture with crack closure and frictional sliding. *Advanced Modeling and Simulation in Engineering Sciences*, 5(1):22. Equal contribution authorship. [44](#)
- [5] Abedi, R., Haber, R. B., and Petracovici, B. (2006a). A spacetime discontinuous Galerkin method for elastodynamics with element-level balance of linear momentum. *Computer Methods in Applied Mechanics and Engineering*, 195:3247–73. [3](#), [44](#)
- [6] Abedi, R., Haber, R. B., Thite, S., and Erickson, J. (2006b). An  $h$ -adaptive spacetime-discontinuous Galerkin method for linearized elastodynamics.

*Revue Européenne de Mécanique Numérique (European Journal of Computational Mechanics)*, 15(6):619–42. [30](#), [56](#), [76](#)

- [7] Abedi, R. and Mudaliar, S. (2017). An asynchronous spacetime discontinuous Galerkin finite element method for time domain electromagnetics. *Journal of Computational Physics*, 351(Supplement C):121–144. [3](#), [44](#)
- [8] Amestoy, P., Duff, I. S., Koster, J., and L’Excellent, J.-Y. (2001). A fully asynchronous multifrontal solver using distributed dynamic scheduling. *SIAM Journal on Matrix Analysis and Applications*, 23(1):15–41. [6](#), [74](#), [88](#), [94](#)
- [9] Appelö, D., Garcia, F., and Runborg, O. (2019). Waveholtz: Iterative solution of the helmholtz equation via the wave equation. [111](#), [118](#)
- [10] Asllanaj, F., Contassot-Vivier, S., Botella, O., and França, F. H. (2021). Numerical solutions of radiative heat transfer in combustion systems using a parallel modified discrete ordinates method and several recent formulations of wsgg model. *Journal of Quantitative Spectroscopy and Radiative Transfer*, 274:107863. [78](#)
- [11] Avila, M., Codina, R., and Principe, R. (2009). Spatial approximation of the radiation transport equation using a two-scale finite element method. Technical report. . [11](#)
- [12] Badri, M., Jolivet, P., Rousseau, B., and Favennec, Y. (2018a). High performance computation of radiative transfer equation using the finite element method. *Journal of Computational Physics*, 360:74–92. [76](#)
- [13] Badri, M., Jolivet, P., Rousseau, B., and Favennec, Y. (2018b). High performance computation of radiative transfer equation using the finite element method. *Journal of Computational Physics*, 360:74–92. [81](#)
- [14] Bai, W., Zhang, P., Zhang, W., Ma, G., Qi, C., and Liu, H. (2020). A fast and accurate vector radiative transfer model for simulating the near-infrared

- hyperspectral scattering processes in clear atmospheric conditions. *Journal of Quantitative Spectroscopy and Radiative Transfer*, 242:106736. [78](#)
- [15] Benassi, M., Garcia, R., Karp, A., and Siewert, C. (1984). A high-order spherical harmonics solution to the standard problem in radiative transfer. *The Astrophysical Journal*, 280:853–864. [33](#), [100](#)
- [16] Blank, D. A. and Mishra, S. C. (1995). Use of the 2-d collapsed dimension method in absorbing-emitting media with isotropic scattering. In *Radiative Transfer I. Proceedings of the First International Symposium on Radiation Transfer*. Begel House Inc. [35](#)
- [17] Briggs, L., Miller Jr, W., and Lewis, E. (1975). Ray-effect mitigation in discrete ordinate-like angular finite element approximations in neutron transport. *Nuclear Science and Engineering*, 57(3):205–217. [33](#), [60](#)
- [18] Bublitz, C., Lorensi, G. A., de Azevedo, F. S., and Sauter, E. (2022). Numerical results for radiative heat transfer in finite cylindrical medium with isotropic scattering. *Journal of Quantitative Spectroscopy and Radiative Transfer*, 280:108087. [79](#)
- [19] Byun, D. Y., Baek, S. W., and Kim, M. Y. (2003). Investigation of radiative heat transfer in complex geometries using blocked-off, multiblock, and embedded boundary treatments. *Numerical Heat Transfer, Part A: Applications*, 43(8):807–825. [90](#)
- [20] Cannon, C. (1970). Line transfer in two dimensions. *The Astrophysical Journal*, 161:255. [38](#)
- [21] Castro, R. O. and Trelles, J. P. (2015). Spatial and angular finite element method for radiative transfer in participating media. *Journal of Quantitative Spectroscopy and Radiative Transfer*, 157:81–105. [34](#), [102](#)

- [22] Cengel, Y. and Özişik, M. (1985). Radiation transfer in an anisotropically scattering plane-parallel medium with space-dependent albedo  $\omega(x)$ . *Journal of Quantitative Spectroscopy and Radiative Transfer*, 34(3):263–270. [13](#), [21](#), [22](#)
- [23] Chai, J. C., Lee, H. S., and Patankar, S. V. (1993). Ray effect and false scattering in the discrete ordinates method. *Numerical Heat Transfer, Part B Fundamentals*, 24(4):373–389. [33](#), [60](#)
- [24] Chandrasekhar, S. (2013). *Radiative transfer*. Courier Corporation. [33](#)
- [25] Charest, M. R., Groth, C. P., and ömer L. Gülder (2012). Solution of the equation of radiative transfer using a newton-krylov approach and adaptive mesh refinement. *Journal of Computational Physics*, 231(8):3023–3040. [80](#)
- [26] Clarke, P., Wang, H., Garrard, J., Abedi, R., and Mudaliar, S. (2019a). Space-angle discontinuous Galerkin method for plane-parallel radiative transfer equation. *Journal of Quantitative Spectroscopy and Radiative Transfer*, 233:87–98. [61](#)
- [27] Clarke, P., Wang, H., Garrard, J., Abedi, R., and Mudaliar, S. (2019b). Space-angle discontinuous Galerkin method for plane-parallel radiative transfer equation. *Journal of Quantitative Spectroscopy and Radiative Transfer*, 233:87–98. [35](#), [55](#), [56](#), [102](#)
- [28] Clarke, P., Wang, H., Garrard, J., Abedi, R., and Mudaliar, S. (2019c). Space-angle discontinuous galerkin method for plane-parallel radiative transfer equation. *Journal of Quantitative Spectroscopy and Radiative Transfer*, 233:87–98. [79](#)
- [29] Clarke, P. L., Wang, H., Garrard, J. M., Abedi, R., and Mudaliar, S. (July 8-13, 2018). A discontinuous Galerkin method for the solution of one dimensional radiative transfer equation. In *2018 USNC-URSI Radio Science Meeting (Joint with AP-S Symposium)*, pages 71–72, Boston, Massachusetts, USA. [35](#)

- [30] Coelho, P. (2004). A hybrid finite volume/finite element discretization method for the solution of the radiative heat transfer equation. In *ICHMT DIGITAL LIBRARY ONLINE*. Begel House Inc. [12](#)
- [31] Coelho, P. J. (2014). Advances in the discrete ordinates and finite volume methods for the solution of radiative heat transfer problems in participating media. *Journal of Quantitative spectroscopy and Radiative transfer*, 145:121–146. [33](#), [100](#)
- [32] Colomer Rey, G. (2006). *Numerical methods for radiative heat transfer*. Universitat Politècnica de Catalunya. [2](#)
- [33] Crockatt, M. M., Christlieb, A. J., Garrett, C. K., and Hauck, C. D. (2017). An arbitrary-order, fully implicit, hybrid kinetic solver for linear radiative transport using integral deferred correction. *Journal of Computational Physics*, 346:212 – 241. [12](#), [34](#), [55](#), [61](#)
- [34] Cui, X. and Li, B. Q. (2004). A discontinuous finite-element formulation for internal radiation problems. *Numerical Heat Transfer, Part B: Fundamentals*, 46(3):223–242. [12](#), [55](#)
- [35] Cui, X. and Li, B. Q. (2005). Discontinuous finite element solution of 2-d radiative transfer with and without axisymmetry. *Journal of Quantitative Spectroscopy and Radiative Transfer*, 96(3-4):383–407. [12](#), [55](#)
- [36] Cui, Z., Bai, H., Jiang, H., Lu, Y., Chen, J., and Zhang, G. (2020). Changes of the abundances of fe, ni, zr isotopes due to neutron radiative capture reactions in heavy water reactors. *Radiation Physics and Chemistry*, 171:108757. [78](#)
- [37] D. Kitzmann, J. Bolte, and A. B. C. Patzer (2016). Discontinuous Galerkin finite element methods for radiative transfer in spherical symmetry. *A&A*, 595:A90. [12](#), [35](#), [101](#)

- [38] Dahmen, W., Gruber, F., and Mula, O. (2020). An adaptive nested source term iteration for radiative transfer equations. *Mathematics of Computation*, 89(324):1605–1646. [62](#)
- [39] Dehesa, J., Zarzo, A., Yañez, R., Germano, B., and Ricci, P. (1994). Orthogonal polynomials and differential equations in neutron-transport and radiative-transfer theories. *Journal of Computational and Applied Mathematics*, 50(1):197–206. [78](#)
- [40] Doktorwurde, E. D. (1996). *Parallel and Adaptive Galerkin Methods for Radiative Transfer Problems*. PhD thesis, Institut für Angewandte Mathematik, Universität Heidelberg. [61](#)
- [41] Drumm, C. and Lorenz, J. (2000). Parallel fe approximation of the even/odd-parity form of the linear boltzmann equation. *Mathematical and Computer Modelling*, 31(2):55–71. [80](#)
- [42] Duderstadt, J. J. and Martin, W. R. (1979). *Transport theory*. [xiii](#), [2](#), [145](#)
- [43] Duderstadt, J. J. and Martin, W. R. (1979). *Transport theory*. John Wiley & Sons, New York, United States. [33](#), [56](#)
- [44] Egger, H. and Schlottbom, M. (2016). A class of Galerkin schemes for time-dependent radiative transfer. *SIAM Journal on Numerical Analysis*, 54(6):3577–3599. [11](#), [34](#)
- [45] Eichholz, J. (2011). *Discontinuous Galerkin Methods for the radiative transfer equation and its approximations*. Dissertation, University of Iowa. [12](#), [34](#), [55](#)
- [46] Evans, K. F. (1998). The spherical harmonics discrete ordinate method for three-dimensional atmospheric radiative transfer. *Journal of the Atmospheric Sciences*, 55(3):429–446. [33](#), [100](#)

- [47] Farooq, A. S., Zhang, P., Gao, Y., and Gulfam, R. (2021). Emerging radiative materials and prospective applications of radiative sky cooling - a review. *Renewable and Sustainable Energy Reviews*, 144:110910. [78](#)
- [48] Fischer, J. W. and Azmy, Y. (2007). Comparison via parallel performance models of angular and spatial domain decompositions for solving neutral particle transport problems. *Progress in Nuclear Energy*, 49(1):37–60. [80](#)
- [49] Fiveland, W. (1984). Discrete-ordinates solutions of the radiative transport equation for rectangular enclosures. *Journal of heat transfer*, 106(4):699–706. [33](#), [100](#)
- [50] Gao, H. and Zhao, H. (2009). A fast-forward solver of radiative transfer equation. *Transport Theory and Statistical Physics*, 38(3):149–192. [12](#), [34](#), [55](#), [101](#)
- [51] Gao, H. and Zhao, H. (2013). Analysis of a numerical solver for radiative transport equation. *Mathematics of Computation*, 82(5):153–172. [12](#), [34](#), [55](#), [101](#)
- [52] Ge, W., Modest, M. F., and Marquez, R. (2015). Two-dimensional axisymmetric formulation of high order spherical harmonics methods for radiative heat transfer. *Journal of Quantitative Spectroscopy and Radiative Transfer*, 156:58–66. [79](#)
- [53] Gonçalves, J. and Coelho, P. J. (1997). Parallelization of the discrete ordinates method. *Numerical Heat Transfer, Part B: Fundamentals*, 32(2):151–173. [80](#)
- [54] Goody, R., West, R., Chen, L., and Crisp, D. (1989). The correlated-k method for radiation calculations in nonhomogeneous atmospheres. *Journal of Quantitative Spectroscopy and Radiative Transfer*, 42(6):539–550. [36](#)
- [55] Grella, K. (2013). Sparse tensor phase space Galerkin approximation for radiative transport. *SpringerPlus*, 3(230). [11](#)

- [56] Grella, K. and Schwab, C. (2011a). Sparse tensor spherical harmonics approximation in radiative transfer. *Journal of Computational Physics*, 230(23):8452 – 8473. [11](#)
- [57] Grella, K. and Schwab, C. (2011b). Sparse tensor spherical harmonics approximation in radiative transfer. *Journal of Computational Physics*, 230(23):8452–8473. [61](#)
- [58] Han, W., Huang, J., and Eichholz, J. A. (2010). Discrete-ordinate discontinuous Galerkin methods for solving the radiative transfer equation. *SIAM Journal on Scientific Computing*, 32(2):477–497. [12](#), [34](#), [55](#)
- [59] Haque, M. E., Wang, H., Abedi, R., and Mudaliar, S. (2023). A discontinuous galerkin method for solving radiative transfer equation with semitransparent boundary conditions. In *2023 United States National Committee of URSI National Radio Science Meeting (USNC-URSI NRSM)*, pages 42–43. [79](#)
- [60] Howell, J. R., Menguc, M. P., and Siegel, R. (2010a). *Thermal radiation heat transfer*. CRC press. [2](#)
- [61] Howell, J. R., Menguc, M. P., and Siegel, R. (2010b). *Thermal radiation heat transfer*. CRC press. [36](#)
- [62] Howell, J. R. and Perlmutter, M. (1964). Radiant transfer through a gray gas between concentric cylinders using Monte Carlo. *ASME Journal of Heat Transfer*, 86(2):169–179. [35](#)
- [63] Howell, L. H. (2005). A parallel amr implementation of the discrete ordinates method for radiation transport. In Plewa, T., Linde, T., and Gregory Weirs, V., editors, *Adaptive Mesh Refinement - Theory and Applications*, pages 255–270, Berlin, Heidelberg. Springer Berlin Heidelberg. [80](#)

- [64] Hu, M., Zhao, B., Ao, X., Suhendri, Cao, J., Wang, Q., Riffat, S., Su, Y., and Pei, G. (2020). An analytical study of the nocturnal radiative cooling potential of typical photovoltaic/thermal module. *Applied Energy*, 277:115625. [78](#)
- [65] Hu, M., Zhao, B., Suhendri, Ao, X., Cao, J., Wang, Q., Riffat, S., Su, Y., and Pei, G. (2022). Applications of radiative sky cooling in solar energy systems: Progress, challenges, and prospects. *Renewable and Sustainable Energy Reviews*, 160:112304. [78](#)
- [66] Ito, G., Kolokolova, L., Petrov, D., and Pitman, K. M. (2022). Packed media radiative-transfer modeling with gaussian particles: Application to spectra of icy regolith of saturnian satellites. *Journal of Quantitative Spectroscopy and Radiative Transfer*, 291:108320. [78](#)
- [67] Jin, S. and Lu, H. (2017). An asymptotic-preserving stochastic Galerkin method for the radiative heat transfer equations with random inputs and diffusive scalings. *Journal of Computational Physics*, 334:182 – 206. [11](#)
- [68] Kanschat, G. (2000). Solution of multi-dimensional radiative transfer problems on parallel computers. In Bjørstad, P. and Luskin, M., editors, *Parallel Solution of Partial Differential Equations*, pages 85–96, New York, NY. Springer New York. [81](#)
- [69] Kesten, A. S. (1968). Radiant heat flux distribution in a cylindrically-symmetric nonisothermal gas with temperature-dependent absorption coefficient. In *Radiative Energy Transfer*, pages 419–434. Elsevier. [35](#)
- [70] Kim, H. K. and Charette, A. (2007). Frequency domain optical tomography using a conjugate gradient method without line search. *Journal of Quantitative Spectroscopy and Radiative Transfer*, 104(2):248–256. [61](#)

- [71] Klose, A. D., Ntziachristos, V., and Hielscher, A. H. (2005). The inverse source problem based on the radiative transfer equation in optical molecular imaging. *Journal of Computational Physics*, 202(1):323–345. [78](#)
- [72] Kópházi, J. and Lathouwers, D. (2015). A space–angle dgfem approach for the boltzmann radiation transport equation with local angular refinement. *Journal of Computational Physics*, 297:637–668. [61](#)
- [73] Kophazi, J. and Lathouwers, D. (2015). A space angle DGFEM approach for the boltzmann radiation transport equation with local angular refinement. *Journal of Computational Physics*, 297:637 – 668. [12](#), [35](#), [101](#)
- [74] Krishnamoorthy, G., Rawat, R., and Smith, P. J. (2004). Parallel computations of radiative heat transfer using the discrete ordinates method. *Numerical Heat Transfer, Part B: Fundamentals*, 47(1):19–38. [80](#)
- [75] Laboure, V. M., McClarren, R. G., and Hauck, C. D. (2016). Implicit filtered  $P_N$  for high-energy density thermal radiation transport using discontinuous Galerkin finite elements. *Journal of Computational Physics*, 321:624 – 643. [12](#), [34](#), [61](#)
- [76] Le Hardy, D., Favennec, Y., and Rousseau, B. (2016a). Solution of the 2-D steady-state radiative transfer equation in participating media with specular reflections using SUPG and DG finite elements. *Journal of Quantitative Spectroscopy and Radiative Transfer*, 179:149–164. [62](#), [76](#)
- [77] Le Hardy, D., Favennec, Y., and Rousseau, B. (2016b). Solution of the 2-D steady-state radiative transfer equation in participating media with specular reflections using SUPG and DG finite elements. *Journal of Quantitative Spectroscopy and Radiative Transfer*, 179:149–164. [102](#)
- [78] Le Hardy, D., Favennec, Y., Rousseau, B., and Hecht, F. (2017a). Specular reflection treatment for the 3d radiative transfer equation solved with the discrete ordinates method. *Journal of Computational Physics*, 334:541–572. [79](#)

- [79] Le Hardy, D., Favennec, Y., Rousseau, B., and Hecht, F. (2017b). Specular reflection treatment for the 3D radiative transfer equation solved with the discrete ordinates method. *Journal of Computational Physics*, 334:541–572. [102](#)
- [80] Léger, L., Chevallier, L., and Paletou, F. (2007). Fast 2d non-LTE radiative modelling of prominences-numerical methods and benchmark results. *Astronomy & Astrophysics*, 470(1):1–9. [61](#)
- [81] Lewis, E. E. and Miller, W. F. (1984). *Computational methods of neutron transport*. John Wiley and Sons, Inc, United States. [33](#), [60](#)
- [82] Liu, F., Smallwood, G. J., and Gülder, Ö. L. (2000). Application of the statistical narrow-band correlated-k method to low-resolution spectral intensity and radiative heat transfer calculations - effects of the quadrature scheme. *International Journal of Heat and Mass Transfer*, 43(17):3119–3135. [36](#)
- [83] Liu, L. (2005). Finite element solution of radiative transfer across a slab with variable spatial refractive index. *International Journal of Heat and Mass Transfer*, 48(11):2260–2265. [12](#), [34](#)
- [84] Liu, L. H. and Liu, L. J. (2007). Discontinuous finite element method for radiative heat transfer in semitransparent graded index medium. *Journal of Quantitative Spectroscopy and Radiative Transfer*, 105(3):377–387. [12](#), [34](#), [55](#)
- [85] Lou, C. and Zhang, Z. (2019). Experimental and numerical analysis of radiative entropy generation in industrial and boiler furnaces. *Journal of Quantitative Spectroscopy and Radiative Transfer*, 232:27–34. [78](#)
- [86] Loyalka, S. K. (1969). Radiative heat transfer between parallel plates and concentric cylinders. *International Journal of Heat and Mass Transfer*, 12(11):1513–1517. [xvi](#), [35](#), [36](#), [52](#), [53](#), [56](#), [164](#)
- [87] Mary, T. (2017). *Block Low-Rank multifrontal solvers: complexity, performance, and scalability*. PhD thesis, Université Paul Sabatier-Toulouse III. [94](#)

- [88] Modest, M. F. (2013). *Radiative heat transfer*. Academic press. [33](#), [37](#), [38](#), [52](#), [60](#), [100](#), [104](#), [112](#), [116](#)
- [89] Modest, M. F., Cai, J., Ge, W., and Lee, E. (2014). Elliptic formulation of the simplified spherical harmonics method in radiative heat transfer. *International Journal of Heat and Mass Transfer*, 76:459–466. [33](#), [100](#)
- [90] Modest, M. F. and Mazumder, S. (2022). Chapter 24 - nanoscale radiative transfer. In Modest, M. F. and Mazumder, S., editors, *Radiative Heat Transfer (Fourth Edition)*, pages 887–903. Academic Press, fourth edition edition. [78](#)
- [91] Olbrant, E., Hauck, C. D., and Frank, M. (2012). A realizability-preserving discontinuous Galerkin method for the m1 model of radiative transfer. *Journal of Computational Physics*, 231(17):5612 – 5639. [12](#), [101](#)
- [92] Ouchtout, S., Rousseau, B., and Favennec, Y. (2022). Finite element framework for modeling conducto-radiative transfers within heterogeneous media at both discrete and continuous scales. *International Journal of Heat and Mass Transfer*, 197:123274. [79](#)
- [93] Pal, R. K., Abedi, R., Madhukar, A., and Haber, R. B. (2016). Adaptive spacetime discontinuous Galerkin method for hyperbolic advection-diffusion with a non-negativity constraint. *International Journal for Numerical Methods in Engineering*, 105(13):963–89. [3](#), [44](#)
- [94] Pandey, D. and Cogley, A. (1983). An integral solution procedure for radiative transfer in concentric cylindrical media. *American Society of Mechanical Engineers*. [35](#)
- [95] Phong, B. T. (1975). Illumination for computer generated pictures. *Communications of the ACM*, 18(6):311–317. [114](#)

- [96] Pontaza, J. and Reddy, J. (2005). Least-squares finite element formulations for one-dimensional radiative transfer. *Journal of Quantitative Spectroscopy and Radiative Transfer*, 95(3):387–406. [13](#), [20](#), [21](#), [22](#), [23](#), [29](#), [34](#), [153](#), [154](#)
- [97] Ragusa, J. C., Guermond, J.-L., and Kanschat, G. (2012). A robust sn-dg-approximation for radiation transport in optically thick and diffusive regimes. *Journal of Computational Physics*, 231(4):1947–1962. [61](#)
- [98] Razzaghi, M., Oppenheimer, S., and Ahmad, F. (2001). Numerical solution of radiative transfer problems in a slab medium by Galerkin-type approximation techniques. *Physica Scripta*, 64(2):97. [11](#), [34](#), [55](#)
- [99] Reddy, J. and Murty, V. (1978). Finite-element solution of integral equations arising in radiative heat transfer and laminar boundary-layer theory. *Numerical Heat Transfer, Part B: Fundamentals*, 1(3):389–401. [33](#), [100](#)
- [100] Reed, W. H. and Hill, T. (1973). Triangular mesh methods for the neutron transport equation. Technical report, Los Alamos Scientific Lab., N. Mex.(USA). [60](#)
- [101] Reed, William H and Hill, T. (1973). Triangular mesh methods for the neutron transport equation. Technical Report LA-UR-73-479; CONF-730414-2, Los Alamos Scientific Lab., N.Mex. (USA), Ann Arbor, Michigan, USA. [34](#)
- [102] Rukolaine, S., Vasilyev, M., Yuferev, V., and Galyukov, A. (2002). Numerical solution of axisymmetric radiative transfer problems in arbitrary domains using the characteristic method. *Journal of Quantitative Spectroscopy and Radiative Transfer*, 73(2-5):205–217. [33](#), [38](#), [60](#), [102](#)
- [103] Safronova, A., Stafford, A., Gill, A., and Childers, R. (2021). Polarization of hard x-ray dielectronic satellite lines from na-like w ions. *Journal of Quantitative Spectroscopy and Radiative Transfer*, 272:107788. [78](#)

- [104] Salah, M. B., Askri, F., Slimi, K., and Nasrallah, S. B. (2004). Numerical resolution of the radiative transfer equation in a cylindrical enclosure with the finite-volume method. *International Journal of Heat and Mass Transfer*, 47(10-11):2501–2509. [33](#), [60](#)
- [105] Sallah, M. and Attia, M. T. (2009). On Galerkin technique for transient radiative heat transfer in finite thin media. *Numerical Heat Transfer, Part B: Fundamentals*, 56(4):323–334. [11](#), [34](#), [55](#)
- [106] Sans, M., Farges, O., Schick, V., and Parent, G. (2022). Solving transient coupled conductive and radiative transfers in porous media with a monte carlo method: Characterization of thermal conductivity of foams using a numerical flash method. *International Journal of Thermal Sciences*, 179:107656. [79](#)
- [107] Seaïd, M., Frank, M., Klar, A., Pinnau, R., and Thömmes, G. (2004). Efficient numerical methods for radiation in gas turbines. *Journal of Computational and Applied Mathematics*, 170(1):217–239. [80](#)
- [108] Shmyglevskii, Y. (1973). Calculation of radiative transfer by Galerkin’s method. *USSR Computational Mathematics and Mathematical Physics*, 13(2):157 – 168. [11](#), [34](#), [55](#)
- [109] Siegel, R. and Howell, J. (2002). *Thermal Radiation Heat Transfer*. Taylor and Francis, 4th edition. [2](#), [11](#), [33](#), [59](#), [60](#)
- [110] Solovjov, V. P. and Webb, B. W. (2008). Multilayer modeling of radiative transfer by slw and cw methods in non-isothermal gaseous medium. *Journal of Quantitative Spectroscopy and Radiative Transfer*, 109(2):245–257. [36](#)
- [111] Sun, Y., Li, S., Zhou, R., Guo, Z., and Ma, J. (2022a). Spatial-angular spectral element method with discontinuous galerkin schemes for radiative transfer in 2d irregular enclosures with obstacles based on unstructured spatial elements. *Journal of Quantitative Spectroscopy and Radiative Transfer*, 280:108082. [61](#)

- [112] Sun, Y., Li, S., Zhou, R., Guo, Z., and Ma, J. (2022b). Spatial-angular spectral element method with discontinuous Galerkin schemes for radiative transfer in 2D irregular enclosures with obstacles based on unstructured spatial elements. *Journal of Quantitative Spectroscopy and Radiative Transfer*, 280:108082. [101](#)
- [113] Tang, K. C. and Brewster, M. Q. (1994). K-distribution analysis of gas radiation with nongray, emitting, absorbing, and anisotropic scattering particles. *Journal of Heat Transfer*, 116(4):980–985. [36](#)
- [114] Thynell, S. T. (1998). Discrete-ordinates method in radiative heat transfer. *International journal of engineering science*, 36(12-14):1651–1675. [33](#), [100](#)
- [115] Verhoef, W. and Bach, H. (2012). Simulation of sentinel-3 images by four-stream surface-atmosphere radiative transfer modeling in the optical and thermal domains. *Remote Sensing of Environment*, 120:197–207. The Sentinel Missions - New Opportunities for Science. [78](#)
- [116] Viskanta, R. and Mengüç, M. (1987). Radiation heat transfer in combustion systems. *Progress in Energy and Combustion Science*, 13(2):97–160. [35](#)
- [117] Wang, H., Abedi, R., and Mudaliar, S. (2019). A discontinuous Galerkin method for the solution of two dimensional axisymmetric radiative transfer problem. In *2019 USNC-URSI Radio Science Meeting (Joint with AP-S Symposium)*, Atlanta, Georgia, USA. In press.
- [118] Wang, H., Abedi, R., and Mudaliar, S. (2020a). A parallel space-angle discontinuous galerkin method for radiative transfer in two-dimensional rectangular enclosures. In *2020 IEEE USNC-CNC-URSI North American Radio Science Meeting (Joint with AP-S Symposium)*, pages 1–2. [102](#)
- [119] Wang, H., Abedi, R., and Mudaliar, S. (2020c). Space-angle discontinuous Galerkin method for radiative transfer between concentric cylinders. *Journal of*

*Quantitative Spectroscopy and Radiative Transfer*, 257:107281. [5](#), [61](#), [63](#), [64](#), [70](#), [102](#), [106](#)

- [120] Wang, H., Abedi, R., and Mudaliar, S. (2020d). Space-angle discontinuous galerkin method for radiative transfer between concentric cylinders. *Journal of Quantitative Spectroscopy and Radiative Transfer*, 257:107281. [79](#)
- [121] Wang, H., Abedi, R., and Mudaliar, S. (2021a). Iterative space-angle discontinuous galerkin method for radiative transfer problems from 1d to 3d. In *2021 XXXIVth General Assembly and Scientific Symposium of the International Union of Radio Science (URSI GASS)*, pages 1–4.
- [122] Wang, H., Abedi, R., and Mudaliar, S. (2021b). A space-angle discontinuous galerkin method for one-dimensional cylindrical radiative transfer equation with angular decomposition. In *2021 United States National Committee of URSI National Radio Science Meeting (USNC-URSI NRSM)*, pages 107–108.
- [123] Wang, H., Abedi, R., and Mudaliar, S. (2022). A space-angle discontinuous galerkin method for two-dimensional radiative transfer equation with reflective boundary conditions. In *2022 United States National Committee of URSI National Radio Science Meeting (USNC-URSI NRSM)*, pages 326–327.
- [124] Wang, H., Abedi, R., and Mudaliar, S. (forthcoming). Iterative space-angle discontinuous Galerkin method for radiative transfer equation. *Waves in Random and Complex Media*. [102](#), [107](#)
- [125] Wang, H., Abedi, R., and Mudaliar, S. (January 6-9, 2020b). Space-angle discontinuous Galerkin method for one-dimensional cylindrical radiative transfer equation. In *AIAA Science and Technology Forum and Exposition 2020*, Orlando, Florida, USA. In press.

- [126] Warburton, T., Lomtev, I., Du, Y., Sherwin, S., and Karniadakis, G. (1999). Galerkin and discontinuous galerkin spectral/hp methods. *Computer Methods in Applied Mechanics and Engineering*, 175(3):343–359. [79](#)
- [127] Wareing, T. A., McGhee, J. M., Morel, J. E., and Pautz, S. D. (2001). Discontinuous finite element sn methods on three-dimensional unstructured grids. *Nuclear science and engineering*, 138(3):256–268. [61](#)
- [128] Woźniak, M., Paszynski, M., Pardo, D., Dalcin, L., and Calo, V. (2015). Computational cost of isogeometric multi-frontal solvers on parallel distributed memory machines. *Computer Methods in Applied Mechanics and Engineering*, 284:971–987. [94](#)
- [129] Xiong, T., Sun, W., Shi, Y., and Song, P. (2022). High order asymptotic preserving discontinuous galerkin methods for gray radiative transfer equations. *Journal of Computational Physics*, 463:111308. [79](#)
- [130] Xu, X., Jiang, S., and Sun, W. (2021). A positive and asymptotic preserving filtered pn method for the gray radiative transfer equations. *Journal of Computational Physics*, 444:110546. [79](#)
- [131] Yajima, H., Abe, M., Umemura, M., Takamizu, Y., and Hoshi, Y. (2022). Trinity: A three-dimensional time-dependent radiative transfer code for in-vivo near-infrared imaging. *Journal of Quantitative Spectroscopy and Radiative Transfer*, 277:107948. [78](#)
- [132] Yu, M. J., Baek, S. W., and Park, J. H. (2000). An extension of the weighted sum of gray gases non-gray gas radiation model to a two phase mixture of non-gray gas with particles. *International Journal of Heat and Mass Transfer*, 43(10):1699–1713. [36](#)

- [133] Yuan, D., Cheng, J., and Shu, C.-W. (2016). High order positivity-preserving discontinuous Galerkin methods for radiative transfer equations. *SIAM Journal on Scientific Computing*, 38(5):A2987–A3019. [12](#), [34](#), [55](#), [61](#)
- [134] Zhan, Q., Ren, Q., Zhuang, M., Sun, Q., and Liu, Q. H. (2018). An exact riemann solver for wave propagation in arbitrary anisotropic elastic media with fluid coupling. *Computer Methods in Applied Mechanics and Engineering*, 329:24–39. [44](#)
- [135] Zhan, Q., Zhuang, M., Mao, Y., and Liu, Q. H. (2019). Unified riemann solution for multi-physics coupling: Anisotropic poroelastic/elastic/fluid interfaces. *Journal of Computational Physics*, page 108961. [44](#)
- [136] Zhang, H.-C. and Tan, H.-P. (2009). Evaluation of numerical scattering in finite volume method for solving radiative transfer equation by a central laser incidence model. *Journal of Quantitative Spectroscopy and Radiative Transfer*, 110(18):1965–1977. [79](#)
- [137] Zhang, L., Zhao, J., Liu, L., and Wang, S. (2012). Hybrid finite volume/finite element method for radiative heat transfer in graded index media. *Journal of Quantitative Spectroscopy and Radiative Transfer*, 113(14):1826–1835. [12](#)
- [138] Zhang, Y., Yi, H.-L., and Tan, H.-P. (2013). Natural element method for radiative heat transfer in two-dimensional semitransparent medium. *International Journal of Heat and Mass Transfer*, 56(1):411–423. [90](#)
- [139] Zhao, J. and Liu, L. (2007a). Discontinuous spectral element method for solving radiative heat transfer in multidimensional semitransparent media. *Journal of Quantitative Spectroscopy and Radiative Transfer*, 107(1):1–16. [12](#), [28](#), [34](#), [55](#)
- [140] Zhao, J. and Liu, L. (2007b). Discontinuous spectral element method for solving radiative heat transfer in multidimensional semitransparent media. *Journal of Quantitative Spectroscopy and Radiative Transfer*, 107(1):1–16. [79](#)

- [141] Zhou, H.-C., Chen, D.-L., and Cheng, Q. (2004). A new way to calculate radiative intensity and solve radiative transfer equation through using the monte carlo method. *Journal of Quantitative Spectroscopy and Radiative Transfer*, 83(3):459–481. [79](#)

# Appendix

**Table 1:** Hemispherical reflectivity and transmissivity of a slab with unit thickness, transparent boundaries, and isotropic incidence.

	DG	LS	LS-DOM	Analytic
Reflectivity	0.020878	0.020878	0.020639	0.020878
Transmissivity	0.386094	0.386094	0.386612	0.386096

**Table 2:** Hemispherical reflectivity and transmissivity of a slab with unit thickness, transparent boundaries, and isotropic incidence.

	DG	LS
Reflectivity	0.033816	0.033855
Transmissivity	0.205898	0.205899

**Table 3:** Number of iteration for the GS method and different relaxation factors for the SOR method under different mesh resolutions. The optimum values are shown in boldface.

	relaxation factor	$4 \times 4 \times 4$	$8 \times 8 \times 8$	$16 \times 16 \times 16$	$32 \times 32 \times 32$
GS	(1.0)	24	27	28	32
SOR	1.1	<b>16</b>	<b>19</b>	21	24
	1.2	20	<b>19</b>	<b>19</b>	<b>18</b>
	1.3	25	24	25	23
	1.4	33	32	32	30
	1.5	43	42	41	40
	1.6	59	58	57	55

**Table 4:** Weak scaling performance for AD.

$n_p$	Extrusion	$t_p$ (s)	$E_p$
16	$4 \times 4$	425.263	-
32	$8 \times 4$	446.455	0.952
64	$8 \times 8$	449.612	0.946
128	$16 \times 8$	359.590	1.183
256	$16 \times 16$	413.689	1.028

**Table 5:** Strong scaling performance for AD.

$n_p$	$t_p$ (s)	Iterations	$S_p$	$E_p$
16	5178.387	13	-	-
32	2528.959	13	2.048	1.024
64	1633.772	14	3.170	0.792
128	956.109	16	5.416	0.677
256	608.516	19	8.510	0.532

**Table 6:** Weak scaling performance for DD. The matrix solving time is denoted by  $t_p^{\mathbf{K}}$ .

$n_p$	Elements	$t_p^{\mathbf{K}}$ (s)	$t_p$ (s)	$\alpha = t_p^{\mathbf{K}}/t_p$	$E_p$
16	1408	130.779	150.69	0.868	-
64	5632	397.967	416.442	0.956	0.362
256	22528	2417.68	2440.29	0.991	0.062

**Table 7:** Strong scaling performance for DD.

$n_p$	$t_p^{\mathbf{K}}$ (s)	$t_p$ (s)	$\alpha = t_p^{\mathbf{K}}/t_p$	$S_p$	$E_p$
16	686.211	736.173	0.932	-	-
32	345.882	370.962	0.932	1.984	0.992
64	244.573	258.191	0.947	2.851	0.713
128	126.719	133.939	0.946	5.496	0.687
256	131.281	135.364	0.970	5.438	0.340

**Table 8:** Performance test for hybrid AD-DD.

$n_p^{\text{AD}}$	$n_p^{\text{DD}}$	$t_p(\text{s})$	Iterations	$\alpha = t_p^{\text{K}}/t_p$	$S_p$
256	1	608.516	19	0.045	-
64	4	472.747	14	0.177	1.287
32	8	421.405	13	0.219	1.444
16	16	475.142	13	0.212	1.281
8	32	594.871	13	0.404	1.023
4	64	807.505	12	0.438	0.753
1	256	2539.172	12	0.795	0.240

**Table 9:** The number of iterations for the specular reflection problems.

$\omega_s$	Specular reflection			
	free	bottom	bottom-right	bottom-right-top
0	1	2	3	4
0.25	16	24	28	39
0.5	21	32	38	55
0.75	29	37	58	98
1	25	46	81	168

**Table 10:** The number of iterations (second row) and convergence rate (third row) for the point source problem for  $\kappa = 1$ .

	1) free box	2) three free side	3) corner	4) waveguide	5) single free side	6) closed box
no. iterations	1	2	3	18	24	32
$\alpha$	-	-	-	1.60	1.00	0.72

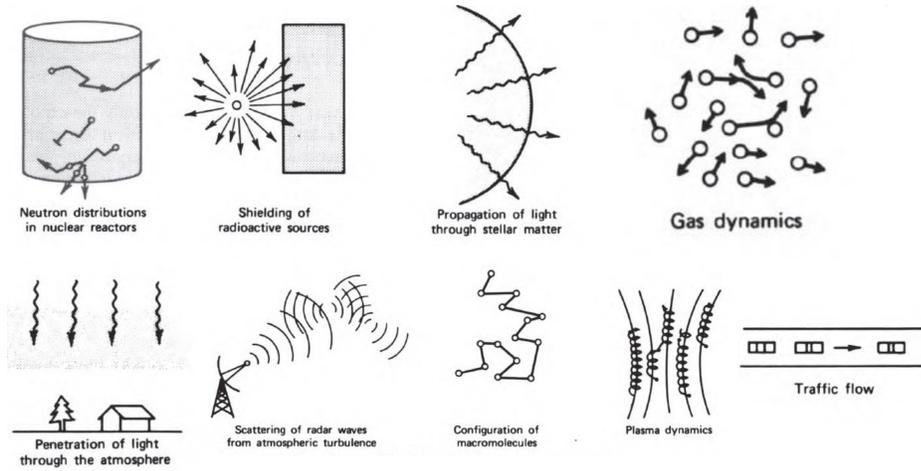


**Figure 1:** The applications of radiation transfer equation [42].

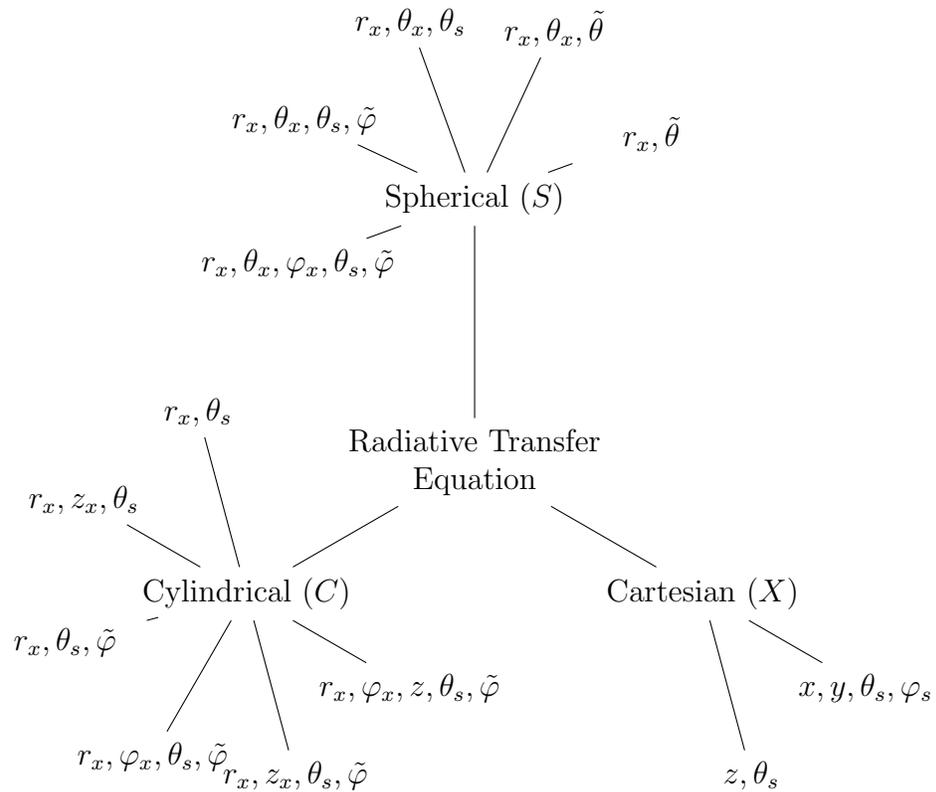


**Figure 2:** This figure shows the variables needed in different versions of RTE in the three coordinate systems, respectively.

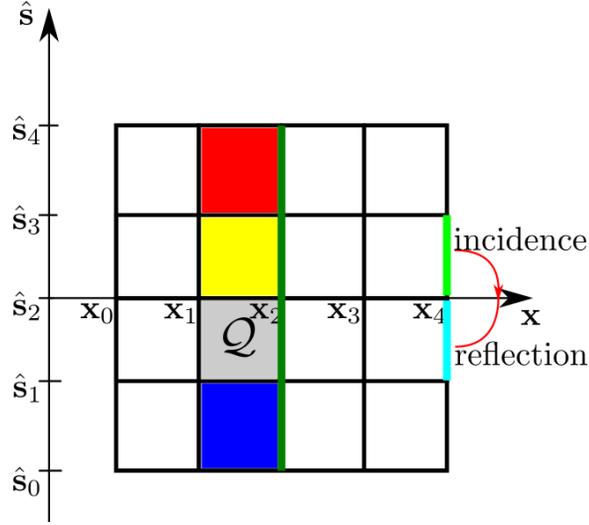


**Figure 3:** A schematic of a space-angle domain. The horizontal axis  $x$  and the vertical axis  $\hat{s}$  represent the space and angle, respectively. The sample element  $Q$  is coupled with the elements in red, yellow, and blue, due to the integral operator. The element boundary in cyan is coupled with the element boundary in blue, since the incidence angle and the reflection angle are located on these element boundaries, respectively. The dark green line separates the domain into two.

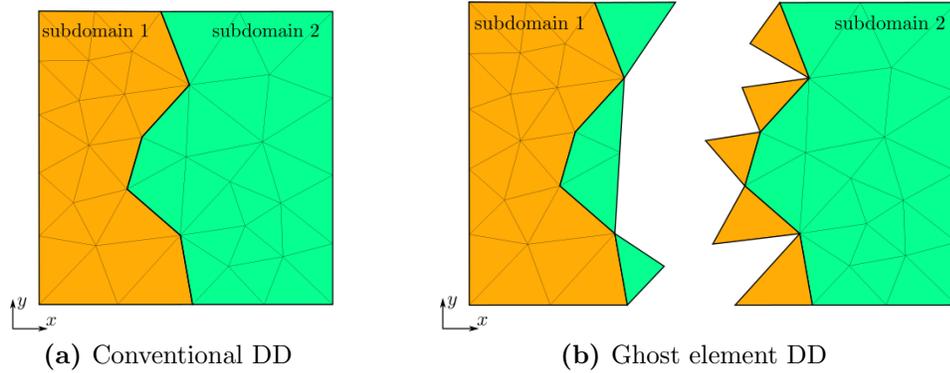


**Figure 4:** Two domain decomposition methods. (a) The spatial domain is partitioned into two non-overlapping subdomains in orange and green. (b) The spatial domain is divided into two subdomains. Each subdomain contains extra elements on the subdomain interface, which are duplicated from its neighbor subdomain.

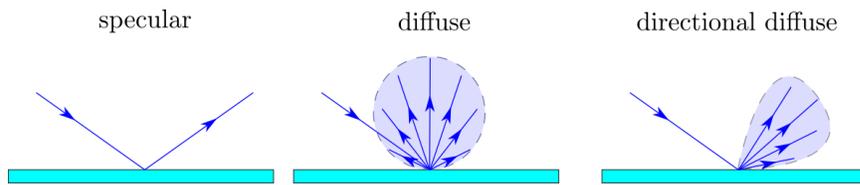


**Figure 5:** Specular, diffuse, and directional diffuse reflection from a surface.

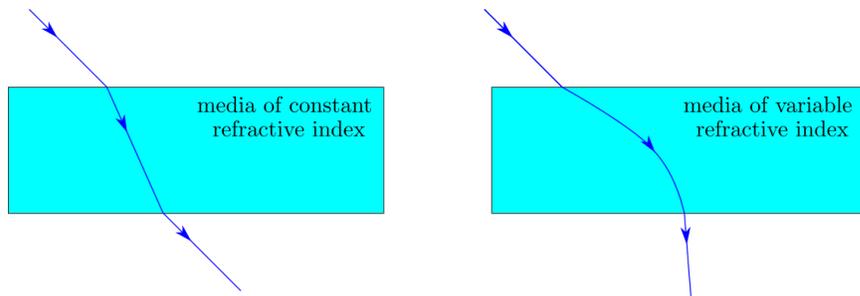


**Figure 6:** Refraction in the media of constant and variable refractive indices.

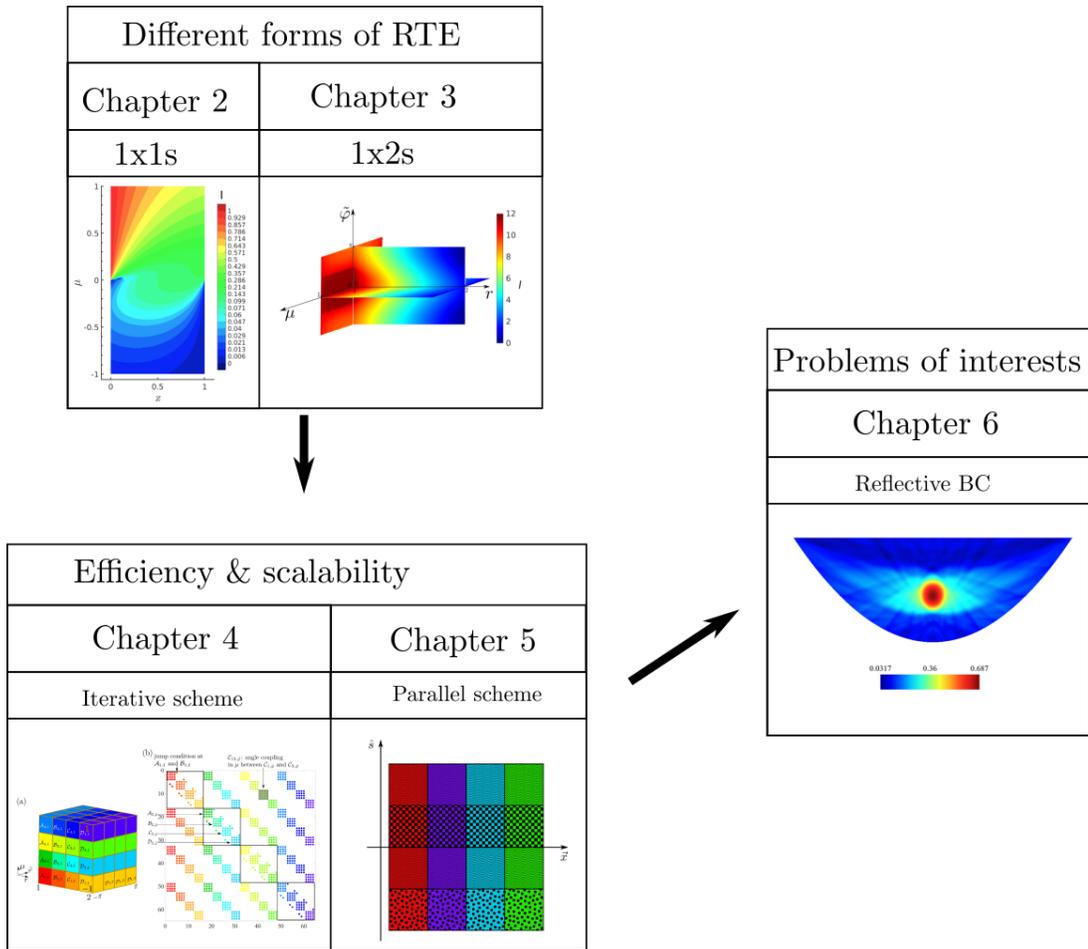


**Figure 7:** Format of the dissertation.

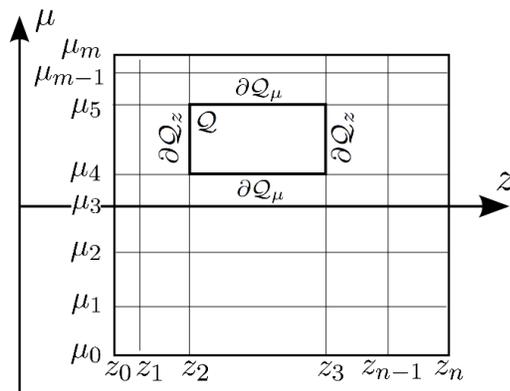


**Figure 8:** Demonstration of region of applicability of residuals in  $(z, \mu)$  domain.

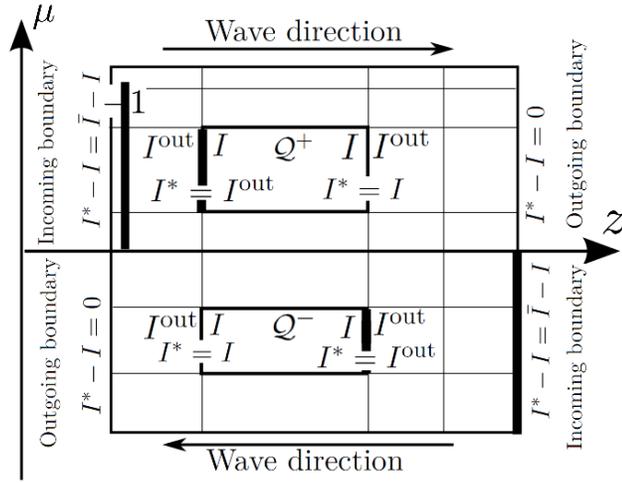


**Figure 9:** The use of wave inflow values for  $I^*$ .

	$p_\mu$	0	1	2	3	...
$p_z$	$\phi_j(\mu')$	1	$\mu'$	$\mu'^2$	$\mu'^3$	...
	$\phi_i(z')$					
0	1	1	$\mu'$	$\mu'^2$	$\mu'^3$	...
1	$z'$	$z'$	$z'\mu'$	$z'\mu'^2$	$z'\mu'^3$	...
2	$z'^2$	$z'^2$	$z'^2\mu'$	$z'^2\mu'^2$	$z'^2\mu'^3$	...
3	$z'^3$	$z'^3$	$z'^3\mu'$	$z'^3\mu'^2$	$z'^3\mu'^3$	...
...	...	...	...	...	...	...

■  $p_z=1, p_\mu=2$  basis

■  $p=p_z=p_\mu=3$  basis

**Figure 10:** The formation of space-angle basis functions by tensor product of space and angle monomial basis functions.

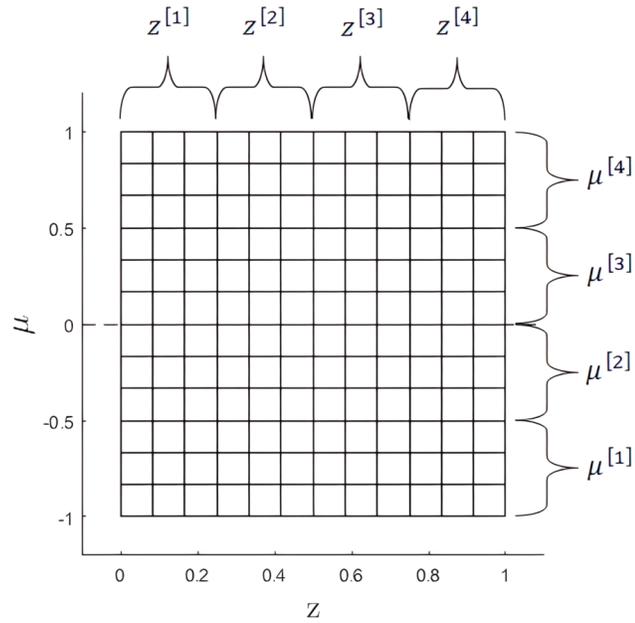


**Figure 11:** SDG Mesh for code verification

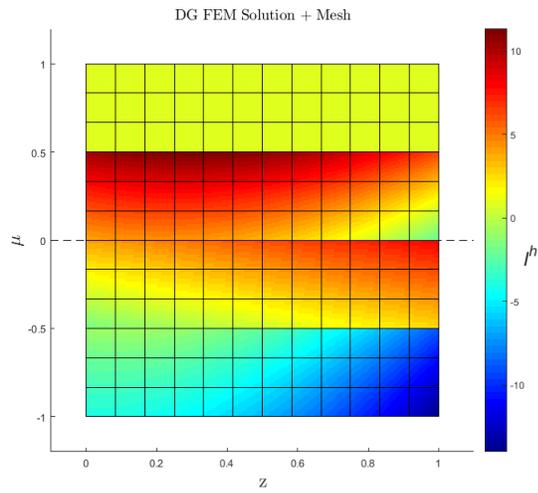


**Figure 12:** Visualization of solution for code verification case of zero phase

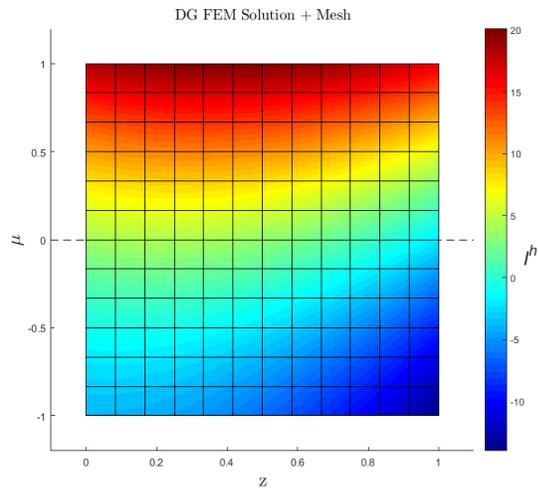


**Figure 13:** Visualization of solution for code verification case of non-zero phase function

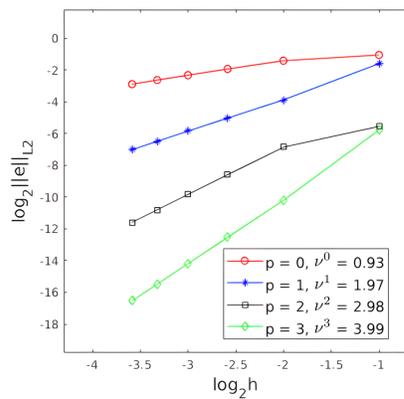


**Figure 14:** Convergence study of the DG RTE solution for a problem with exact harmonic solution. Convergence rate of  $p + 1$  is achieved for the space-angle order of  $p = 0$  to 3.

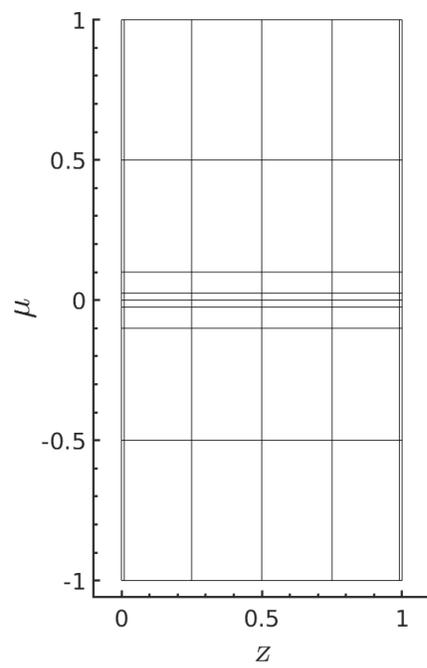


**Figure 15:** Finite element mesh for the DG method in the spatial-angular domain.

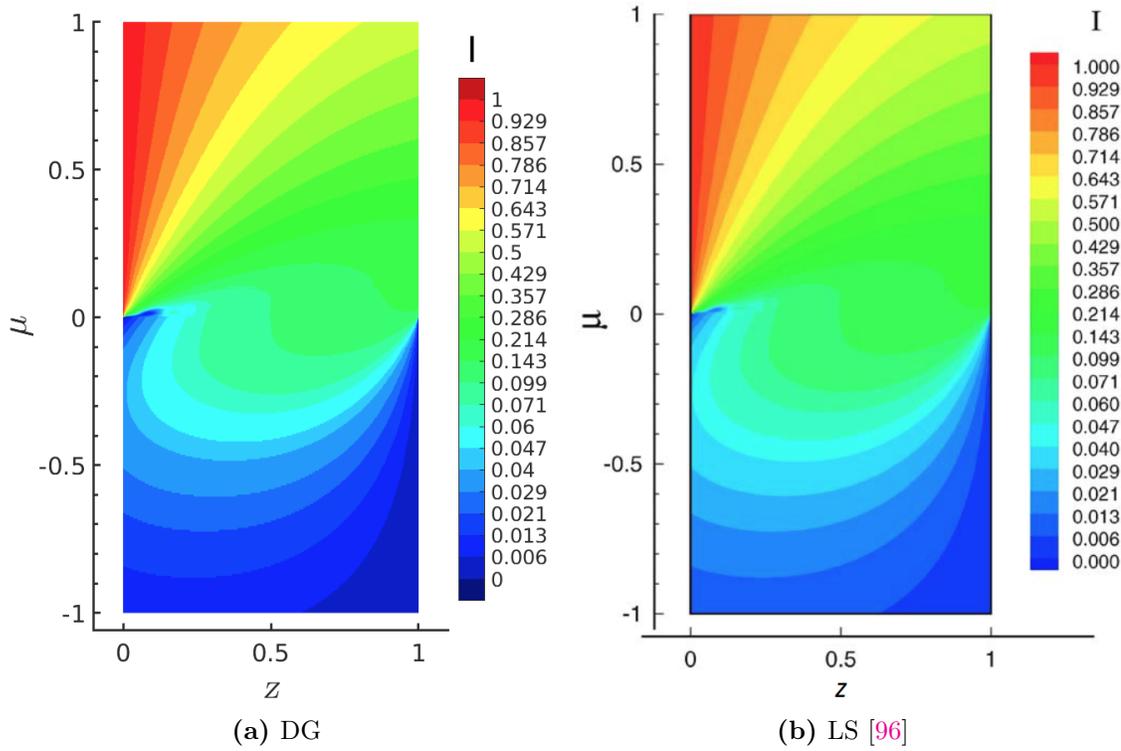


**Figure 16:** Contour plot of radiative intensity,  $I(z, \mu)$ , in space-angle domain.

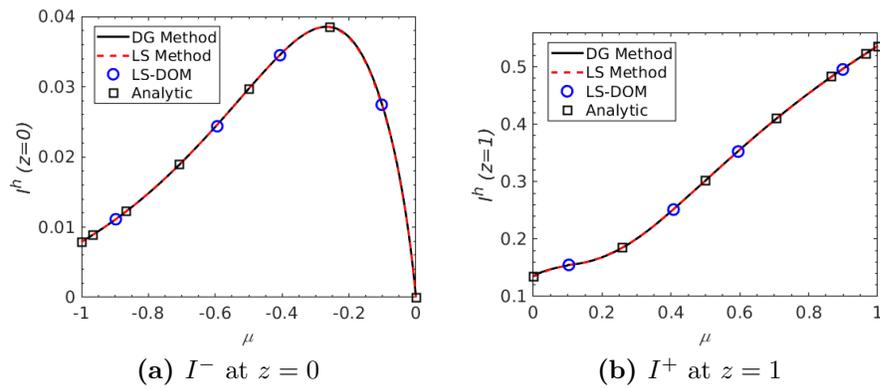


**Figure 17:** Radiative intensity distribution at outflow boundaries.

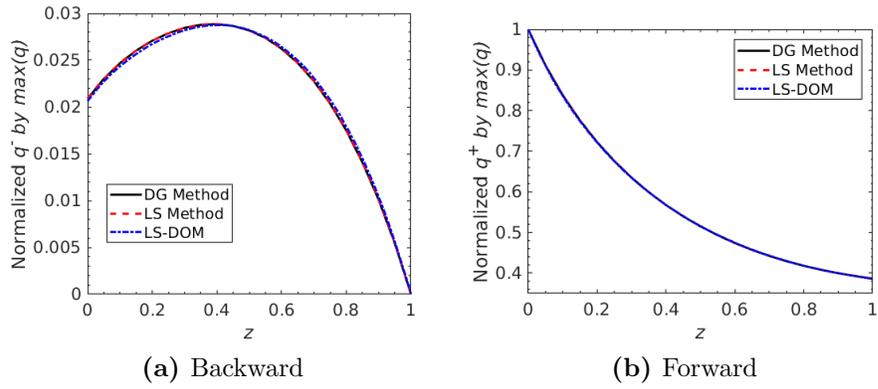


**Figure 18:** Radiation heat flux distribution.

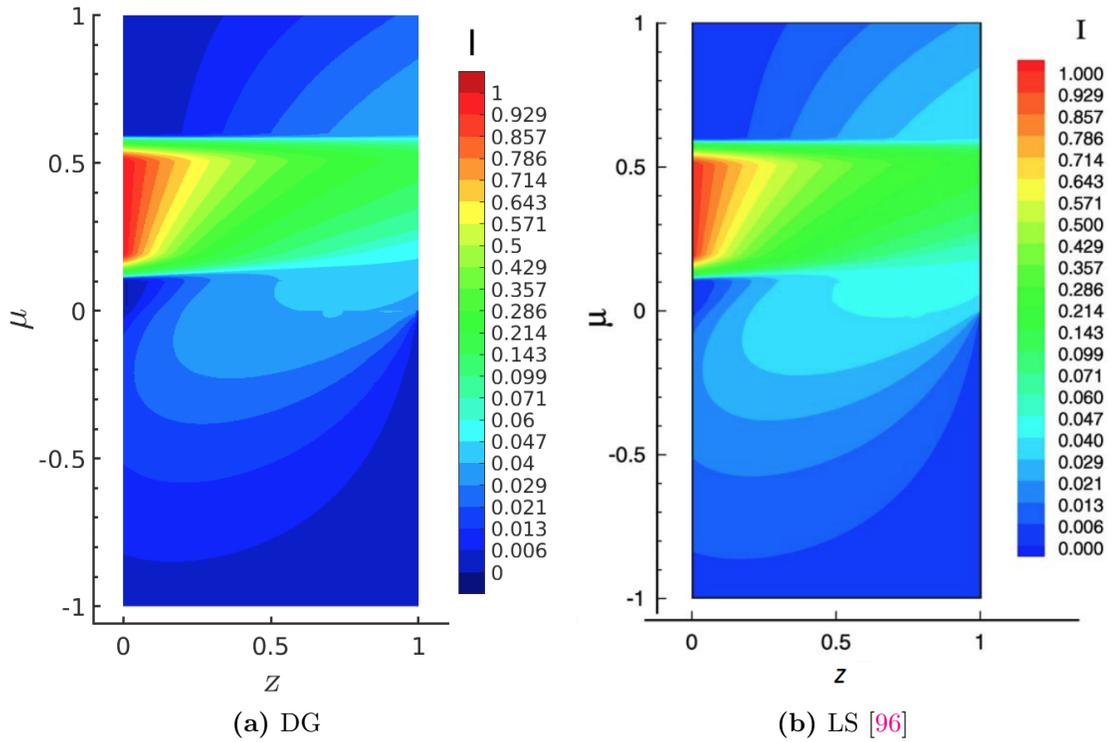


**Figure 19:** Contour plot of radiative intensity,  $I(z, \mu)$ , in space-angle domain.

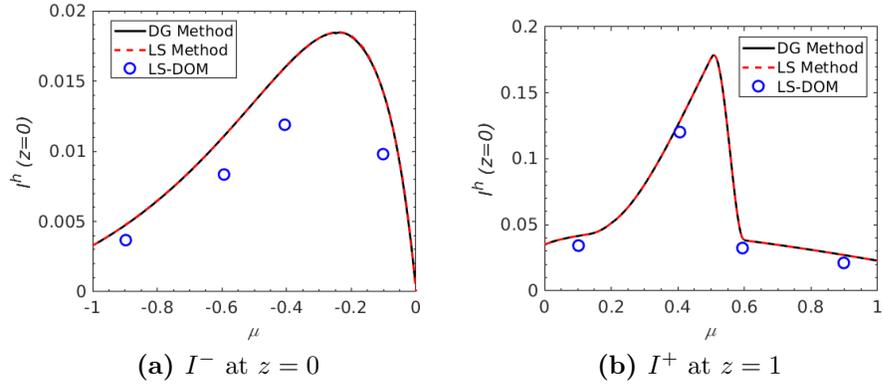


**Figure 20:** Radiative intensity distribution at outflow boundaries.

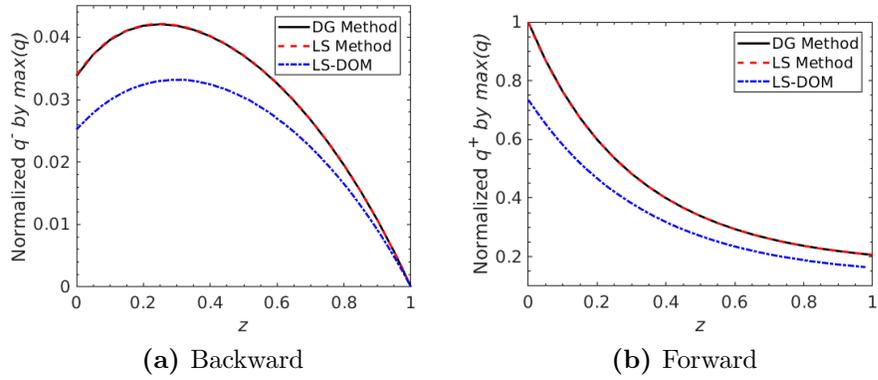
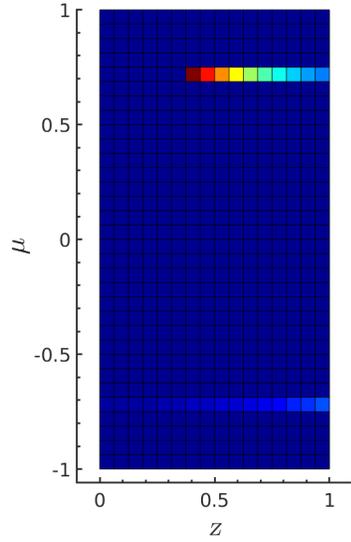
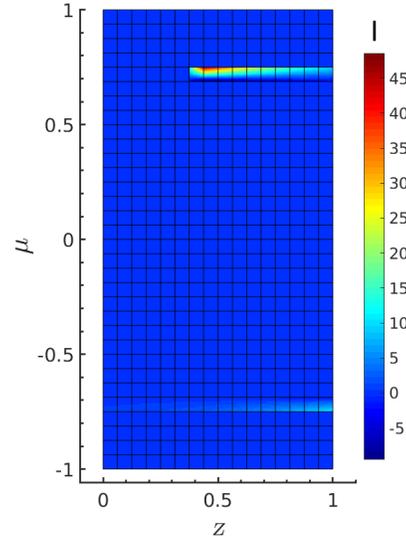


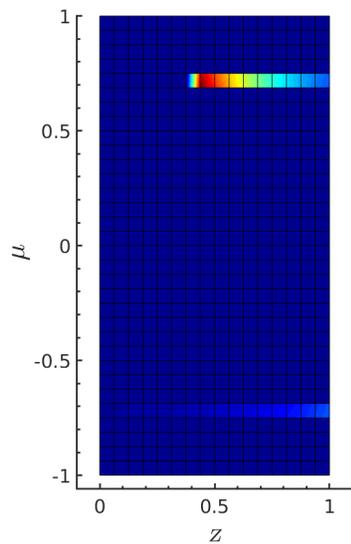
**Figure 21:** Radiation heat flux distribution.



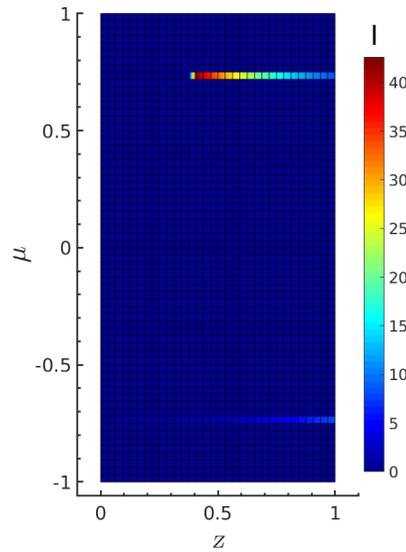
(a)  $16 \times 32$  grid,  $p = 0$ .



(b)  $16 \times 32$  grid,  $p = 1$ .

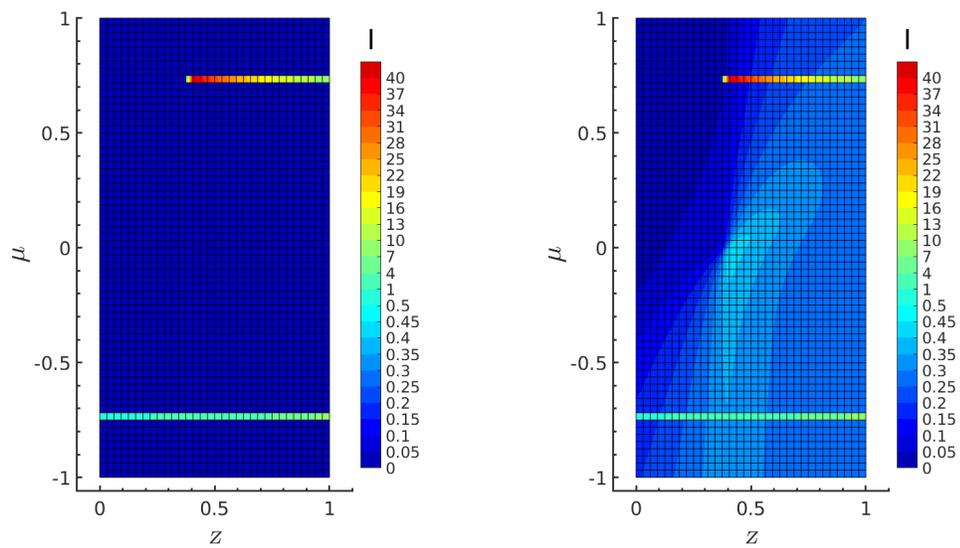


(c)  $16 \times 32$  grid,  $p = 1$ , average source.



(d)  $32 \times 64$  grid,  $p = 1$ , average source.

**Figure 22:** The effect of type of application of point source, element size  $h$ , and order  $p$  on discrete DG solution. In all cases, except f) a zero phase function is used.



(e)  $32 \times 64$  grid,  $p = 3$ , average source. (f)  $32 \times 64$  grid,  $p = 3$ , average source, Rayleigh scattering.

**Figure 22:** (continued) The effect of type of application of point source, element size  $h$ , and order  $p$  on discrete DG solution. In all cases, except f) a zero phase function is used.

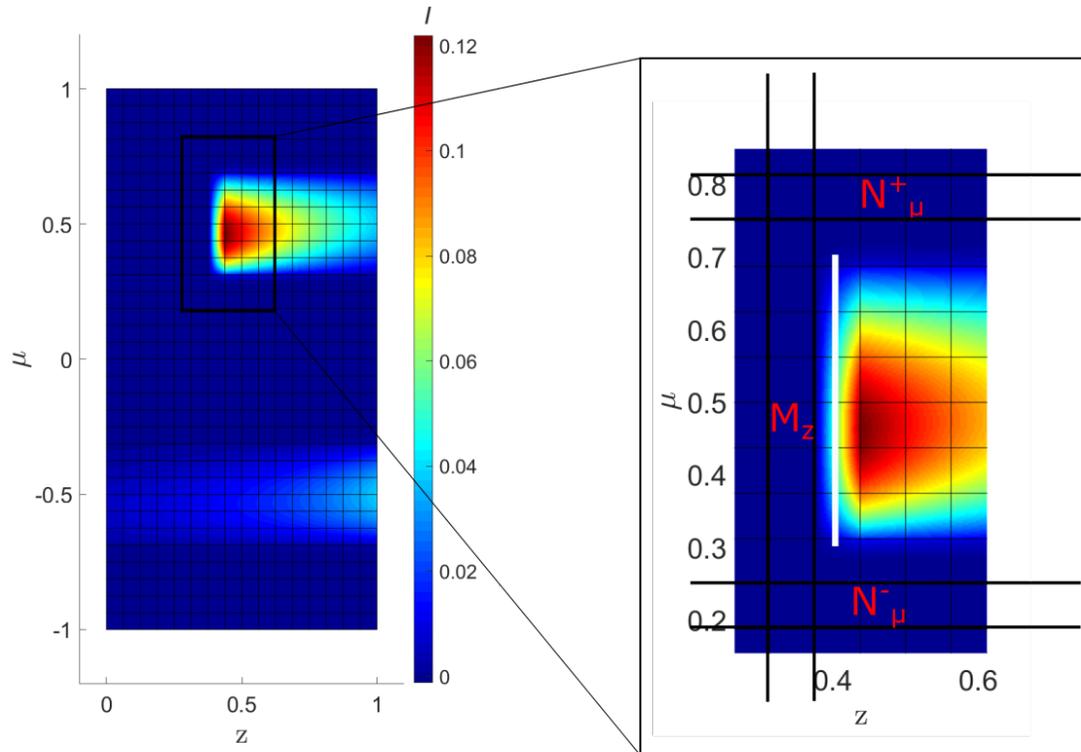


**Figure 23:** Contour plot of radiative intensity for the problem with the line source term. The zoomed view shows the line source by a thick white line and its neighboring elements, where  $M_z$  are the spatial upstream elements of the line source and  $M_\mu^+$  and  $M_\mu^-$  are the upward and downward angular neighboring elements.

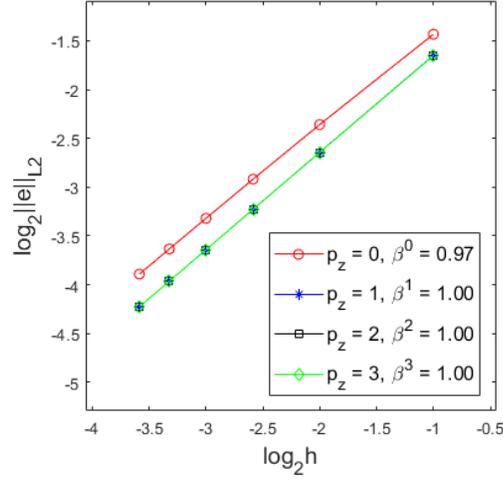


**Figure 24:** Convergence study for the problem in §2.4.1, but with changing only  $p_z$  and fixing  $p_\mu = 0$ .

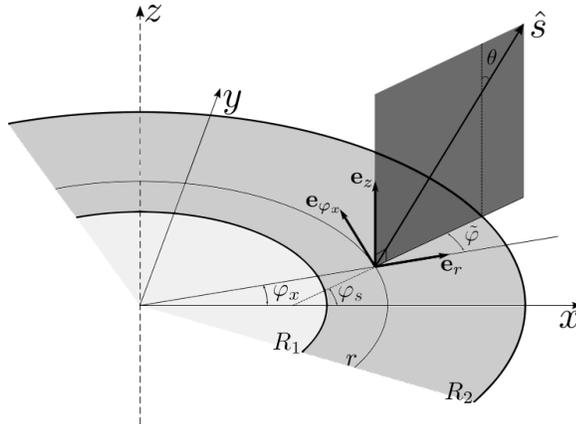


**Figure 25:** Cylindrical coordinates for the one-dimensional RTE.

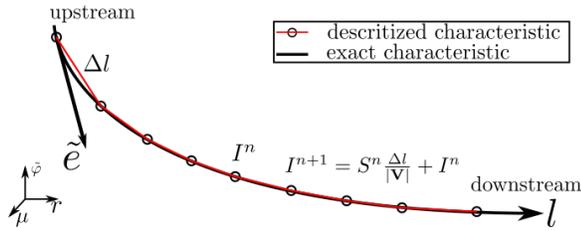


**Figure 26:** Coordinate along a characteristic line.

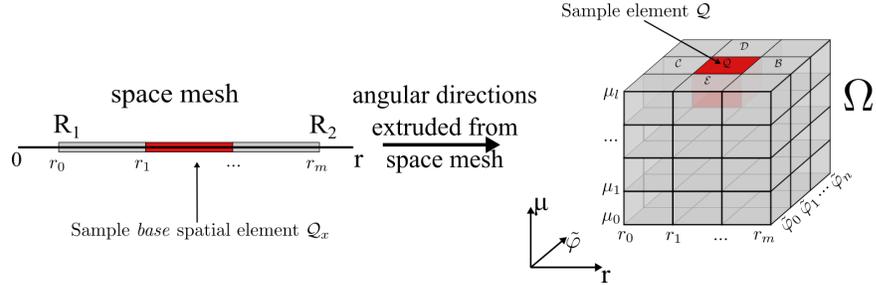


**Figure 27:** The illustration of the extrusion of the spatial domain in angle directions  $\mu$  and  $\tilde{\varphi}$ . The left figure shows the one-dimensional spatial elements and the right shows their extrusion to form the three-dimensional domain  $\Omega$ .

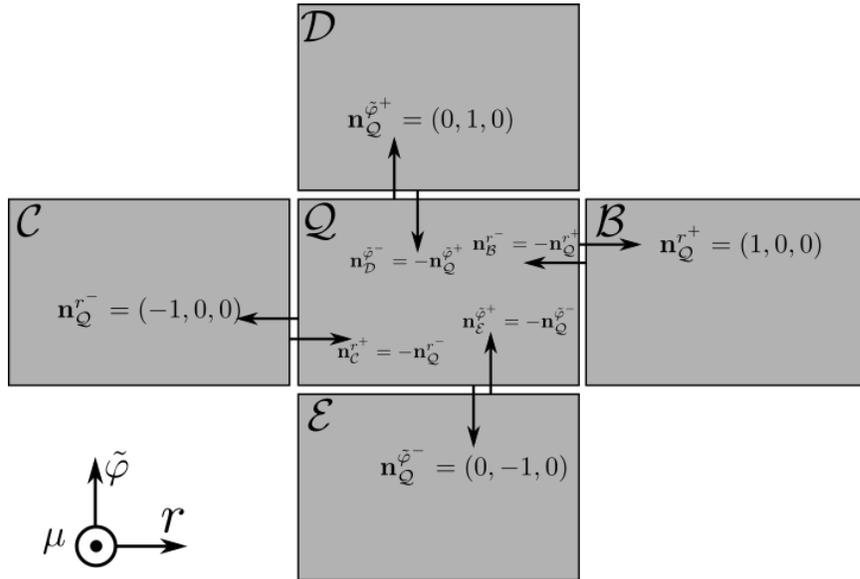


**Figure 28:** The illustration of normal vectors of the element  $Q$  and its neighboring elements on the shared boundaries in  $r$ - $\tilde{\varphi}$  plane. The subscript and superscript of normal vectors correspond to the element with normal vector and its direction, respectively.

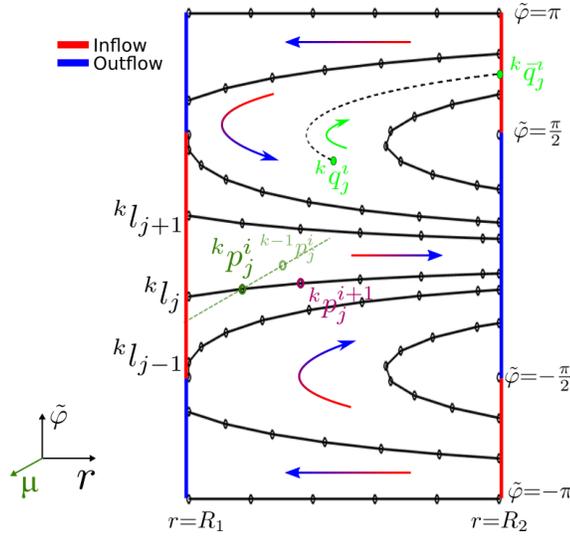


**Figure 29:** Schematic of the discrete set of  $r - \tilde{\varphi}$  planes, characteristic lines, and points for numerical solution of the method of characteristics.

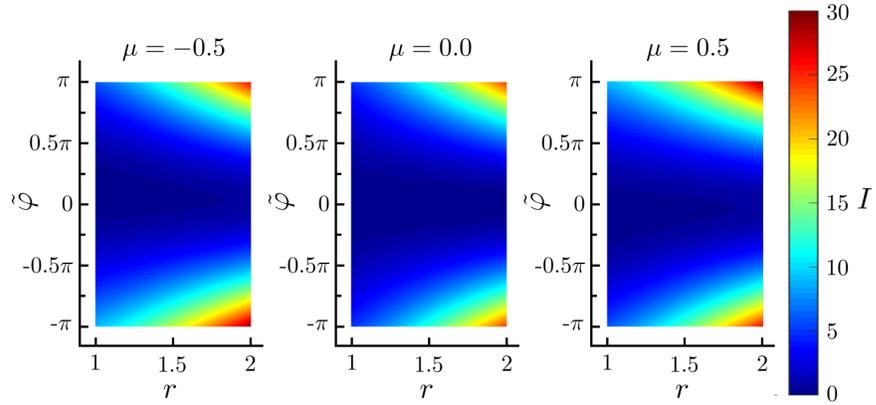


**Figure 30:** Validation of the DG RTE method by the MMS for second order polynomial in space and angle for  $I^M$ . The contour plots in  $r - \tilde{\varphi}$  plane are sliced in  $\mu$  direction at  $\mu = -0.5, 0, 0.5$ .

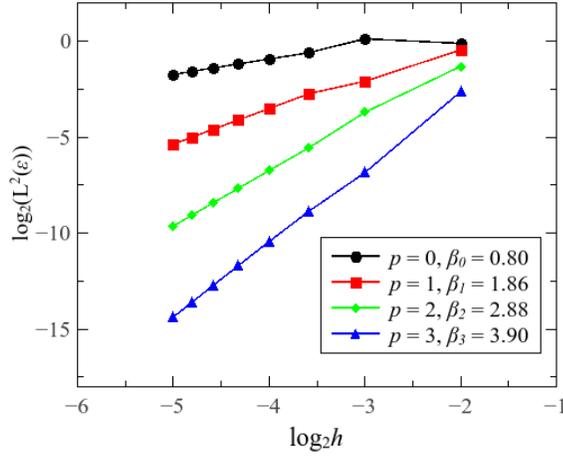


**Figure 31:** Convergence study of the DG RTE solution for the harmonic manufactured solution. The asymptotic convergence rate  $\beta_p = p + 1$  is achieved as  $h \rightarrow 0$  for  $p = 0$  to  $p = 3$ .

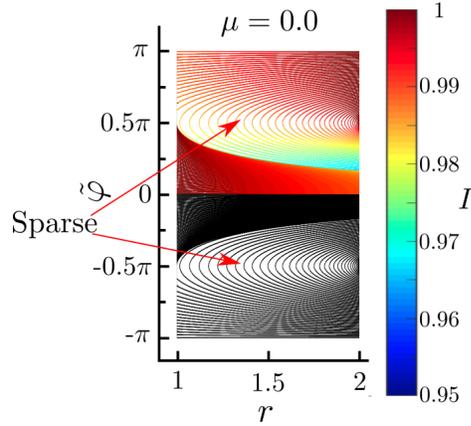
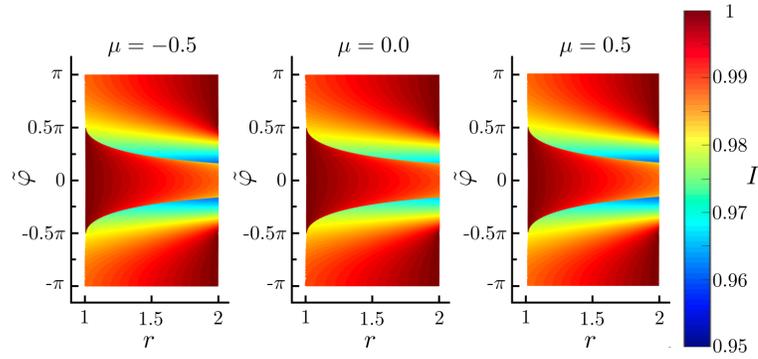
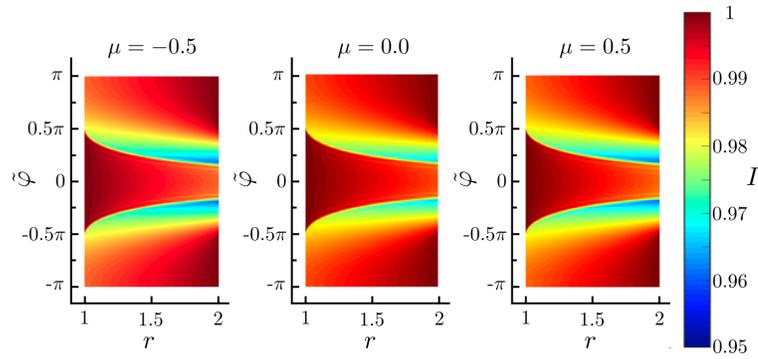


**Figure 32:** The results of the method of characteristic in a  $r - \tilde{\varphi}$  plane, where  $\tilde{\varphi} < 0$  shows the characteristics in black and  $\tilde{\varphi} \geq 0$  shows the characteristics with the intensity field. The red arrows point to regions where characteristic lines are sparse.



(a) Method of characteristics



(b) DG method

**Figure 33:** Contour plots of radiation intensity for the problem in §3.5.2 for two different solution methods.

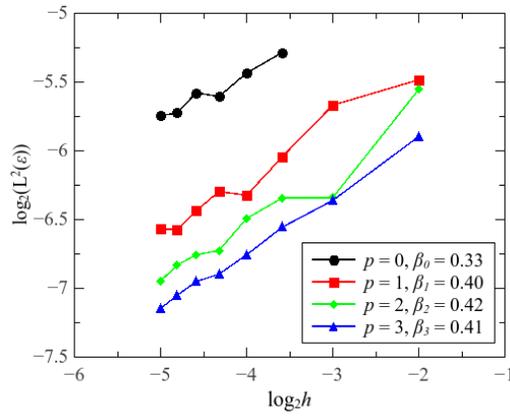


**Figure 34:** Convergence study of the DG RTE solution with respect to a high resolution reference solution obtained by the method of characteristics.

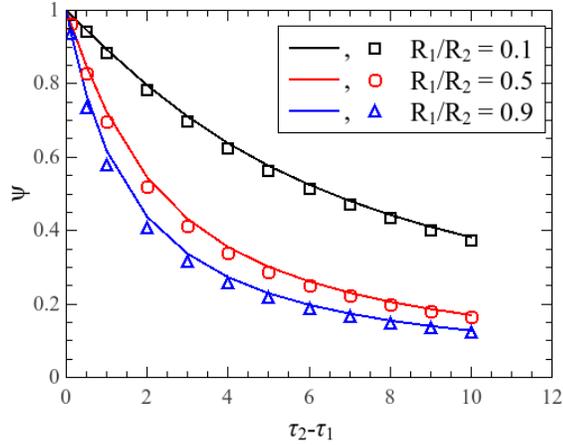


**Figure 35:** Nondimensional radiative heat transfer,  $\Psi$ , between concentric cylinders at radiative equilibrium against the optical thickness,  $\tau_2 - \tau_1$ , at different radius ratio,  $R_2/R_1$ . The solid lines are the numerical solution presented by Loyalka [86]; the hollow shapes (squares, circles and triangles) are the solutions by the DG method.

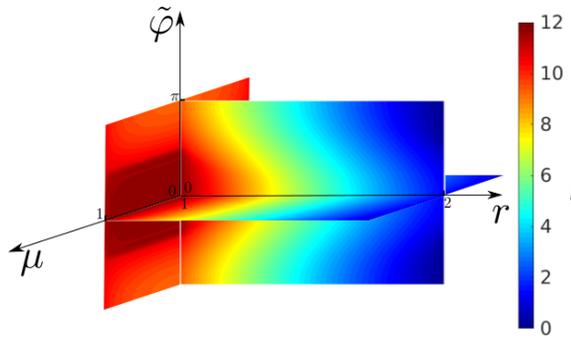


**Figure 36:** Contour plot of radiation intensity of the benchmark problem for  $R_1/R_2 = 0.5$  and  $\tau_2 - \tau_1 = 10$ .

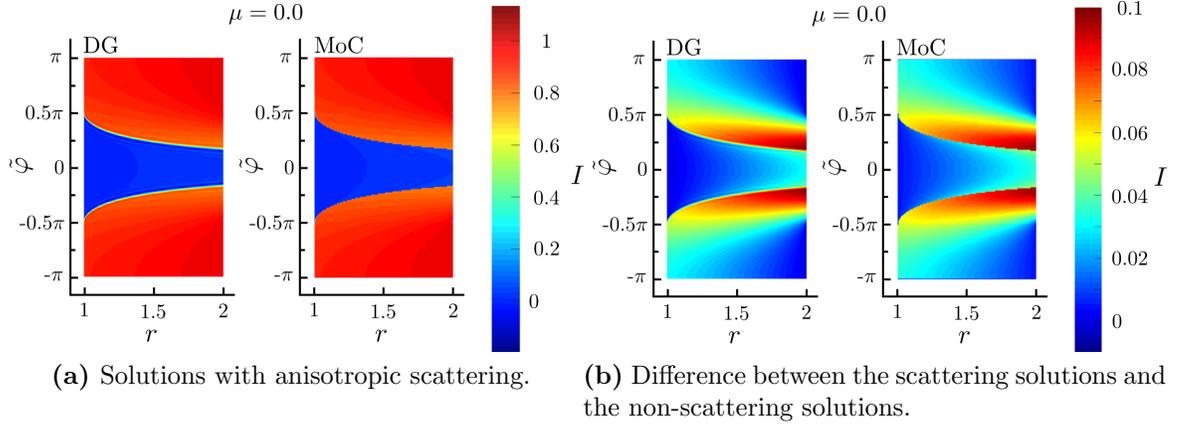


**Figure 37:** Contour plots of radiation intensity for the problem in §3.5.3 for  $\mu = 0$  for two different methods. The left and right figures correspond to the solutions by the DG method and the method of characteristics (MoC), respectively.

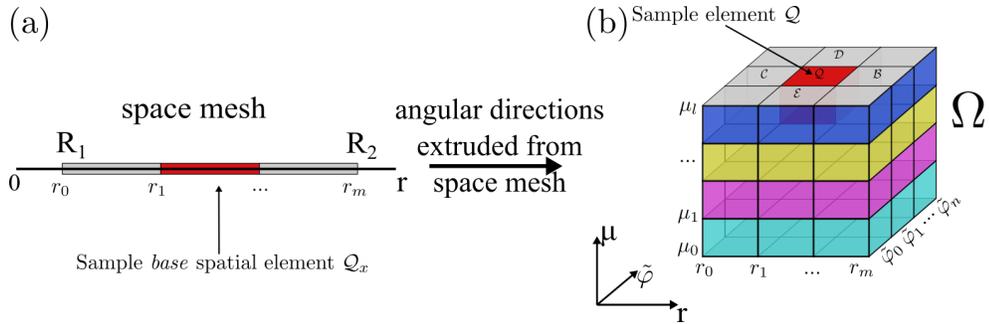


**Figure 38:** The illustration of the extrusion of the spatial domain in angle directions  $\mu$  and  $\tilde{\varphi}$ : a) the one-dimensional spatial elements, b) extrusion of the spatial mesh to form the three-dimensional domain  $\Omega$ .

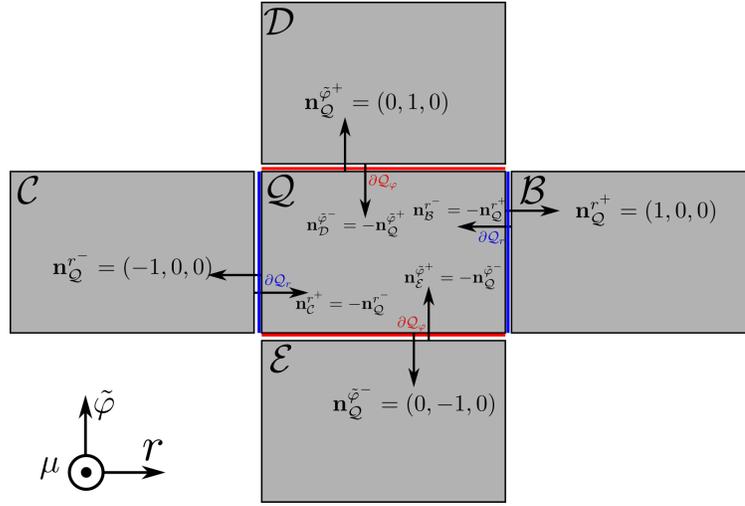


**Figure 39:** Illustrations of normal vectors of the element  $Q$  and its neighboring elements on the shared boundaries in  $r$ - $\tilde{\varphi}$  plane. The blue and lines represent the element boundary in the  $r$  and  $\tilde{\varphi}$  directions, respectively.

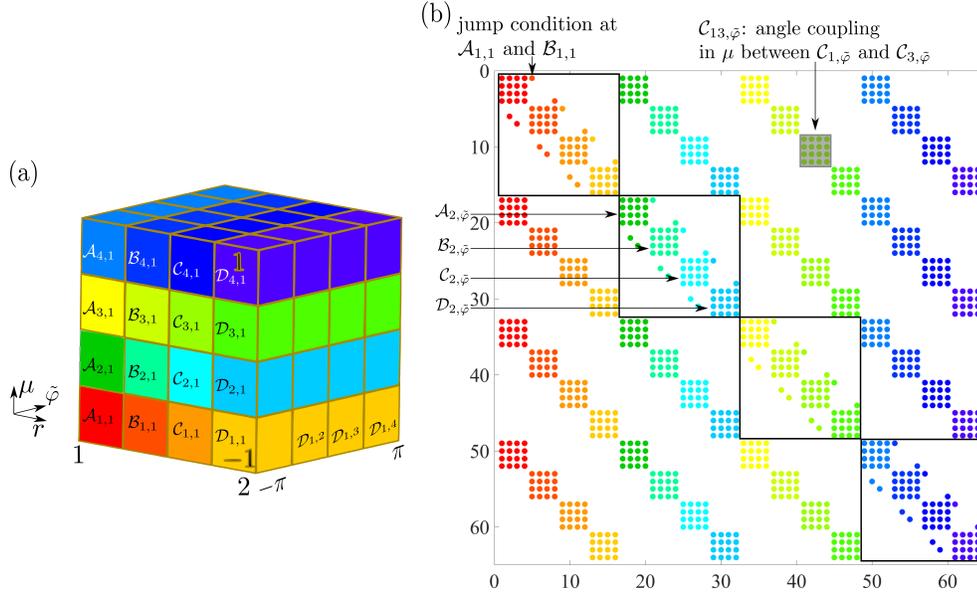


**Figure 40:** The stiffness matrix pattern in a  $4 \times 4 \times 4$  domain: (a) the  $4 \times 4 \times 4$  space-angle mesh; (b) the stiffness matrix pattern of all couplings. The dots represent the matrix block per element. The gray square  $C_{13,\tilde{\varphi}}$  depicts the coupling in  $\mu$  direction between elements  $C_{1,\tilde{\varphi}}$  and  $C_{3,\tilde{\varphi}}$ . The dots in the four larger squares represent in-slab couplings.

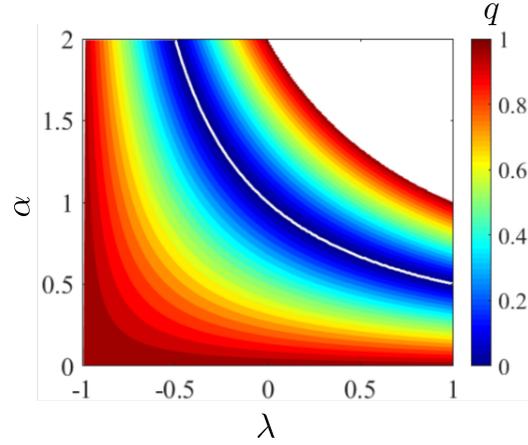


**Figure 41:** Contour plots of the common ratios of the SOR scheme changing with the eigenvalues,  $\lambda$ , and the relaxation factors. The common ratio greater than 1 is not considered (white area). The white curve highlights the optimal relaxation factors for the corresponding eigenvalues.

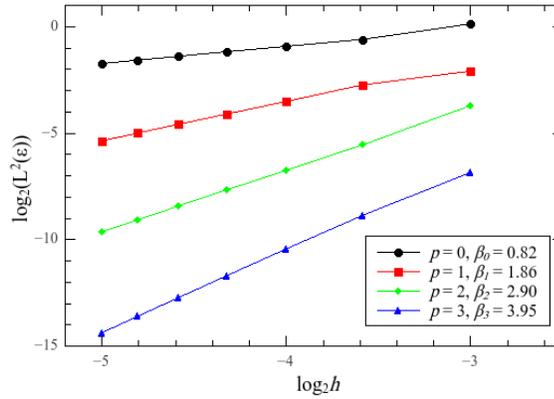


**Figure 42:** Convergence study of the DG RTE solution for the harmonic manufactured solution. The asymptotic convergence rate  $\beta_p = p + 1$  is achieved as  $h \rightarrow 0$  for  $p = 0$  to  $p = 3$ .

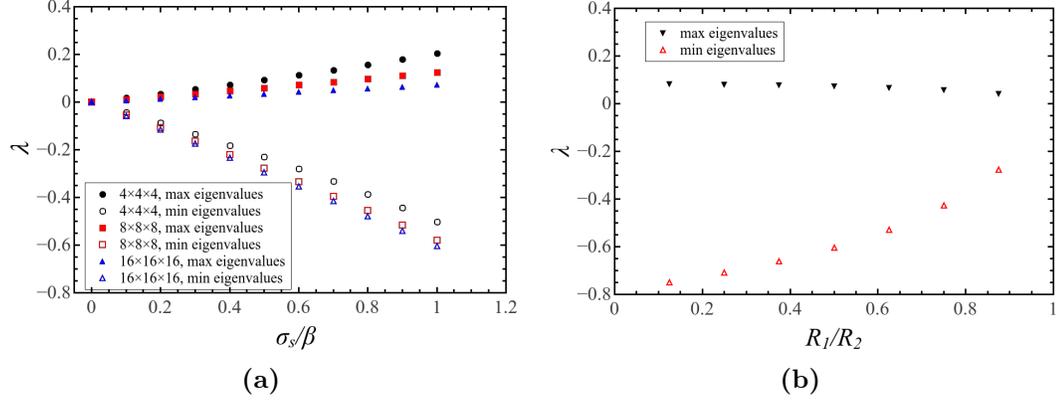


**Figure 43:** The maximum and minimum of  $\lambda$  against (a) the scattering coefficients  $\sigma_s$  of different mesh resolutions (b)  $R_1/R_2$  for the problem described in §4.5.

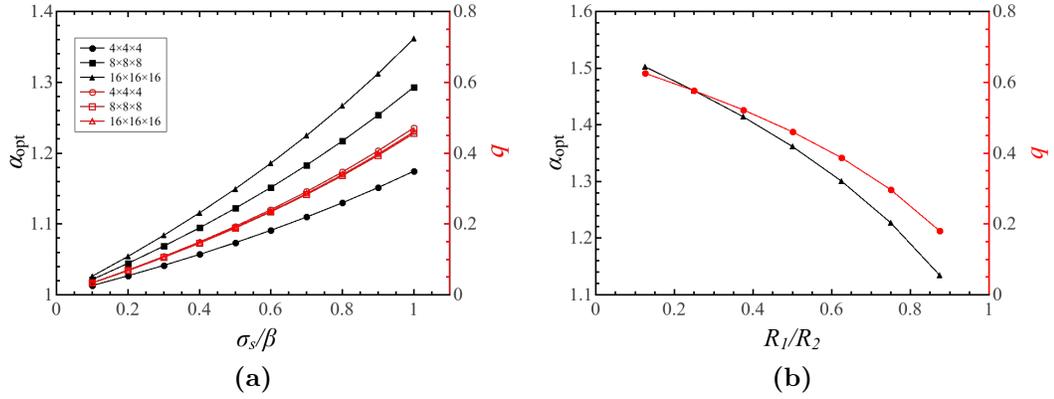


**Figure 44:** The optimal  $\alpha$  (black) and common ratio  $q$  (red) against (a) the scattering coefficients  $\sigma_s$  of different mesh resolutions and (b) the ratio of  $R_1$  and  $R_2$ .

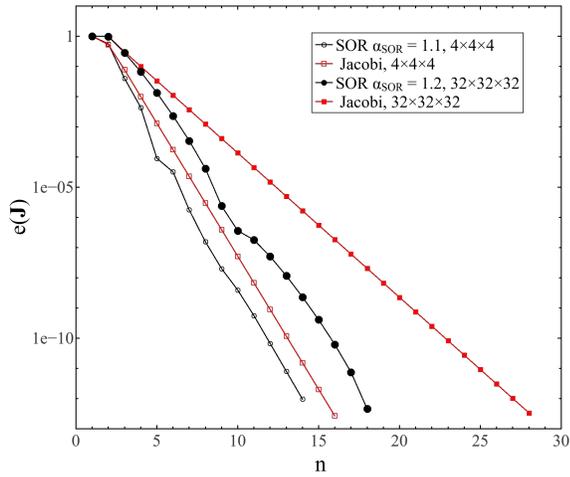


**Figure 45:** Evolution of the error  $e^n(\mathbf{J})$  along iterations. Circle and square markers correspond to the results by the coarse and fine meshes, respectively.

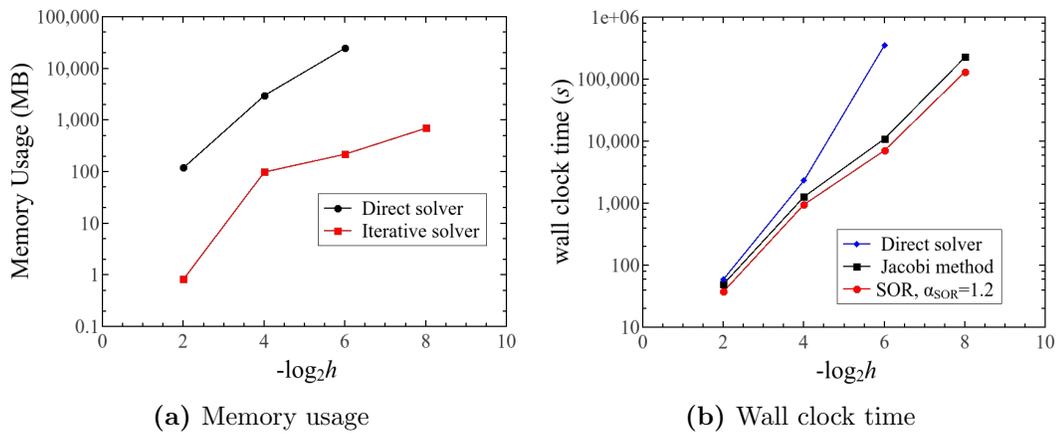


**Figure 46:** Efficiency between direct solver and AD iterative solver.

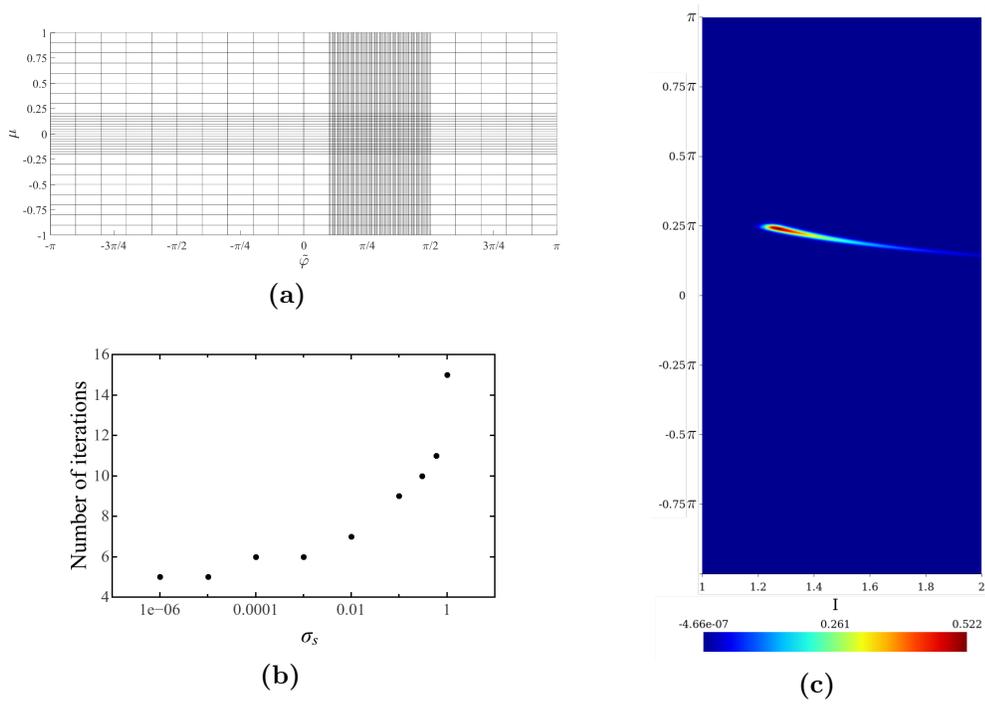


**Figure 47:** (a) The refined angular mesh. (b) The number of iterations for different scattering coefficients. (c) The contour plot of the intensity in the  $r - \tilde{\varphi}$  plane, where  $\mu = 0$ .

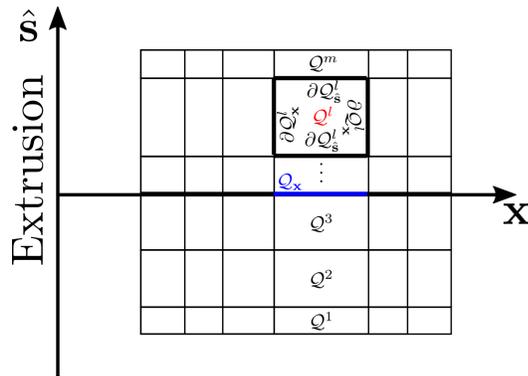


**Figure 48:** Space-angle mesh generated by element extrusion from spatial mesh.

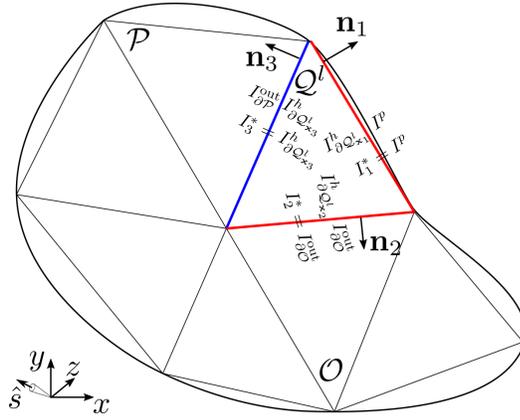


**Figure 49:** An example of jump condition for  $I^*$  in the direction of  $\hat{s}$ .

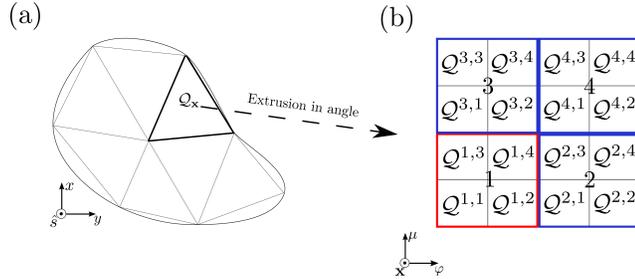


**Figure 50:** An example of angular decomposition for the scattering term. 16 angular elements are divided evenly into four subdomains.

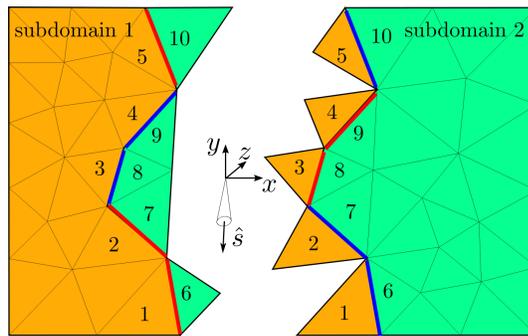


**Figure 51:** The spatial domain is divided into two subdomains. Each subdomain contains extra elements on the subdomain interface, which are duplicated from its neighbor subdomain.

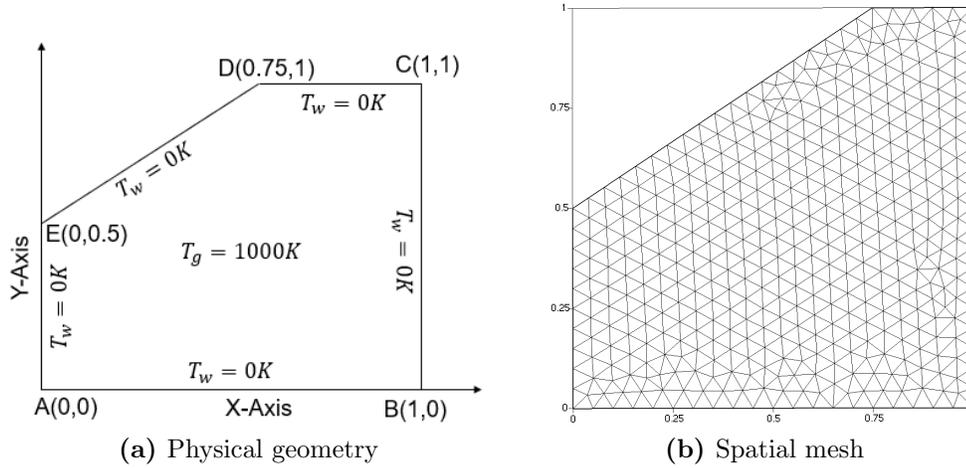


**Figure 52:** Trapezoidal enclosure with boundary conditions and spatial mesh.

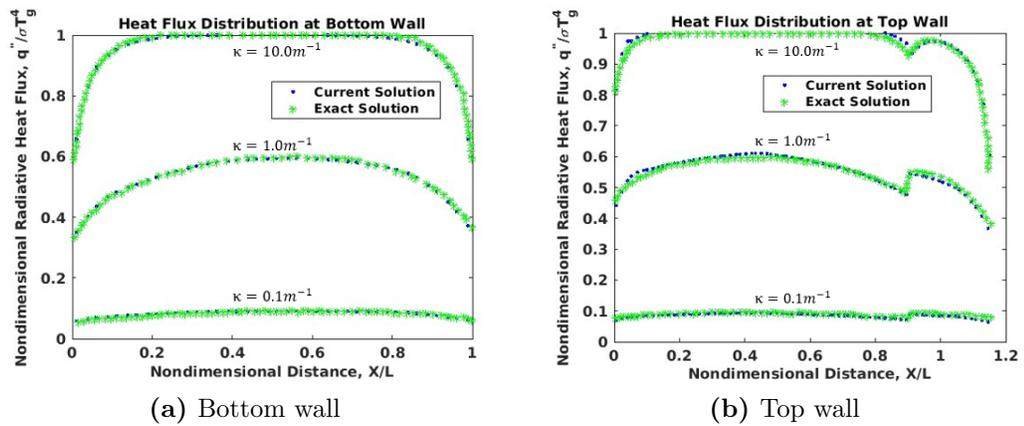


**Figure 53:** Non-dimensional radiative heat flux for  $\kappa = 0.1 \text{ m}^{-1}$ ,  $\kappa = 1.0 \text{ m}^{-1}$ , and  $\kappa = 10 \text{ m}^{-1}$  along the bottom and top walls.

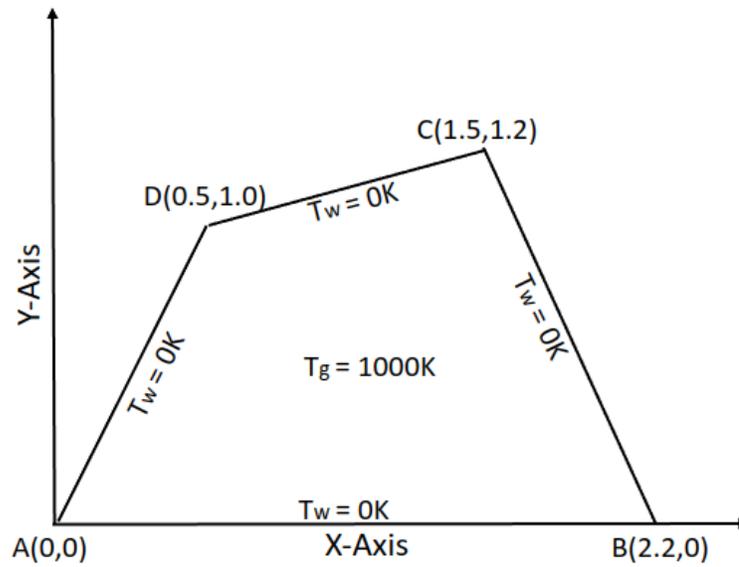


**Figure 54:** Quadrilateral enclosure with boundary conditions.

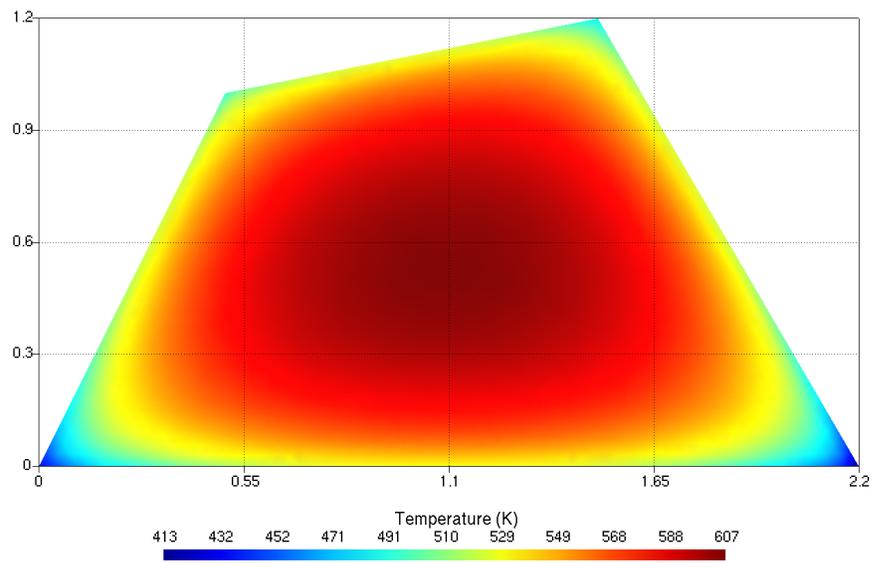
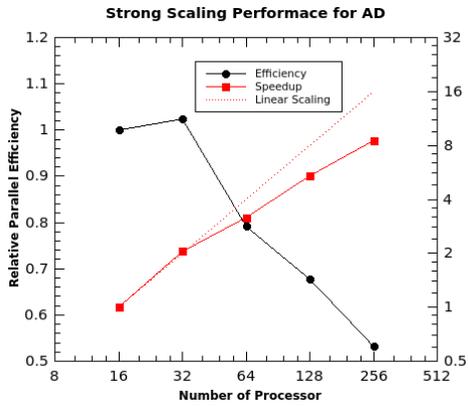
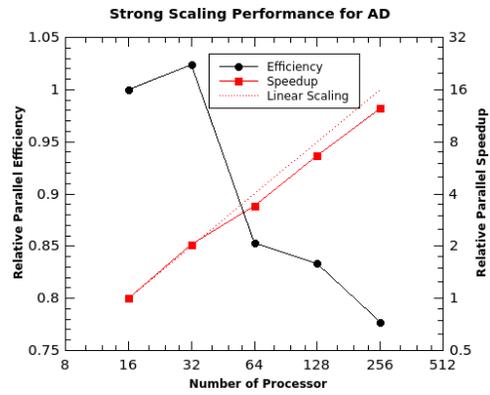


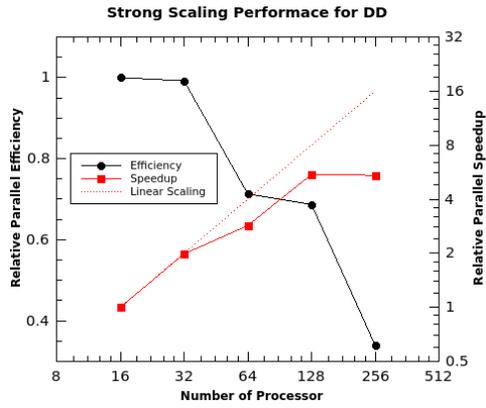
**Figure 55:** Contour temperature plot for a quadrilateral enclosure.



(a) Total run time for AD



(b) Average iteration time for AD



(c) Total run time for DD

**Figure 56:** Strong scaling performance for (a) total run time for AD, (b) average iteration time for AD, and (c) total run time for DD.

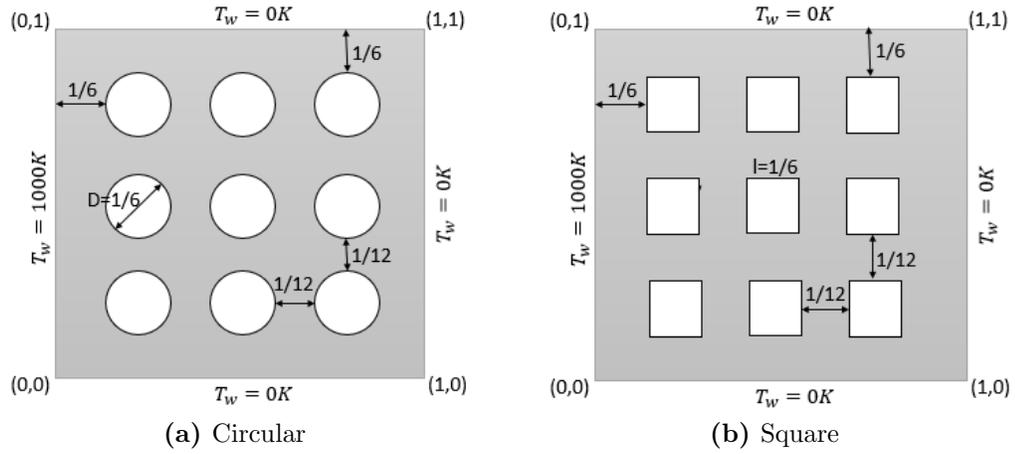


**Figure 57:** A schematic for the square geometry with obstacles (a) Circular, (b) Square.

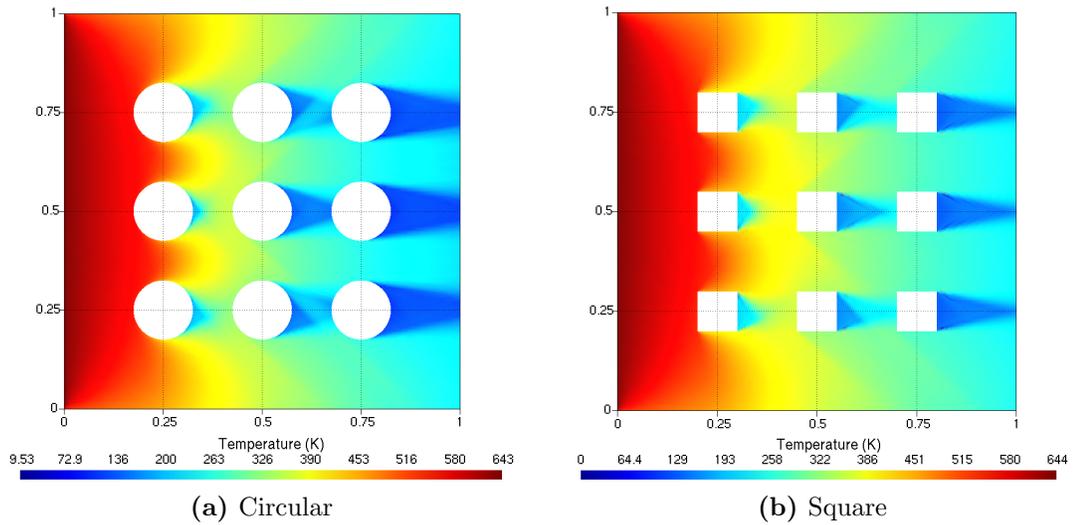


**Figure 58:** A schematic for the contour temperature field with obstacles (a) Circular, (b) Square.



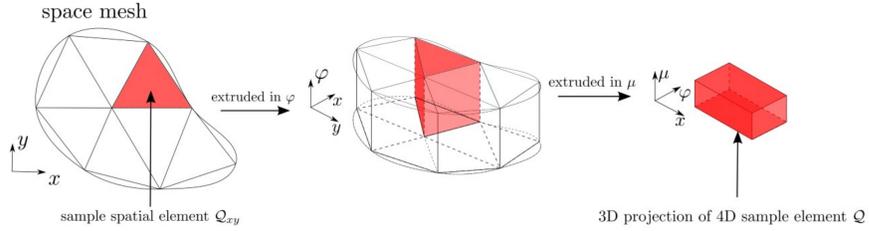


**Figure 62:** Space-angle mesh generated by 2D element extrusion from spatial mesh.

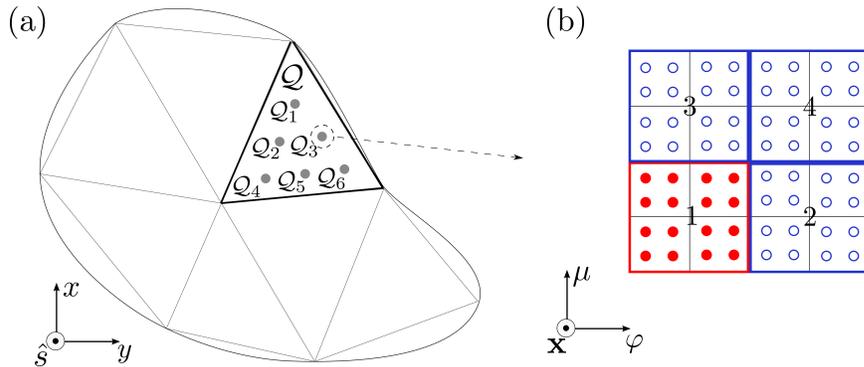


**Figure 63:** An example of angular decomposition for the scattering integral term. (a) Spatial mesh. The sample element  $Q$  contains 6 quad points in space. (b) Angular domain at spatial point  $Q_3$ . 16 angular elements are divided evenly into four slabs. Slab 1 and its quadrature points (solid dots) are in red; the other slabs and quadrature points (hollow dots) are in blue.

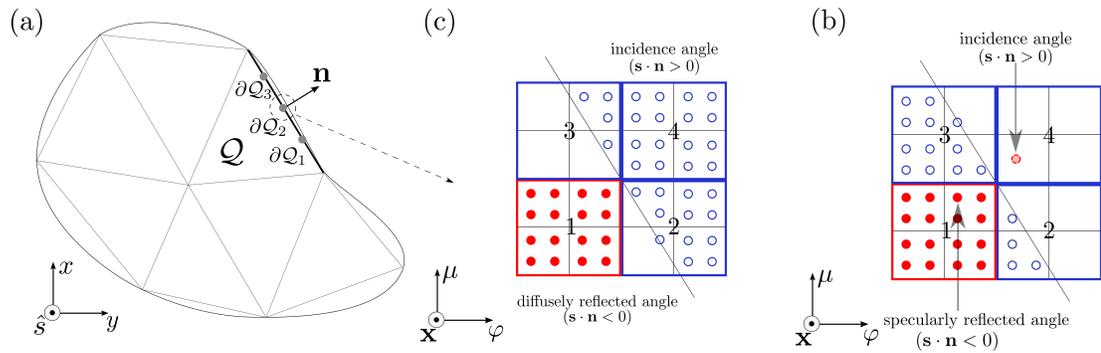


**Figure 64:** Illustrations of the implementation of the reflective BCs. (a) For a given spatial quadrature point  $\partial Q_2$  on the boundary of element  $Q$ , the spatial normal  $\mathbf{n}$  is known and determines the slant line that divides the angular domain into incidence angles and reflected angles in (b) and (c) that correspond to the angular domain of point  $\partial Q_2$ . The red solid dots are the quadrature points in slab 1. (b) The blue hollow dots are the decoupled quadrature points. (c) The blue hollow dots are the quadrature points in the reflected angle. The red dash-dot circle (pointed to with an arrow) is the specular incident angle corresponding to the specularly reflected angle solid red point, pointed to by the other arrow.

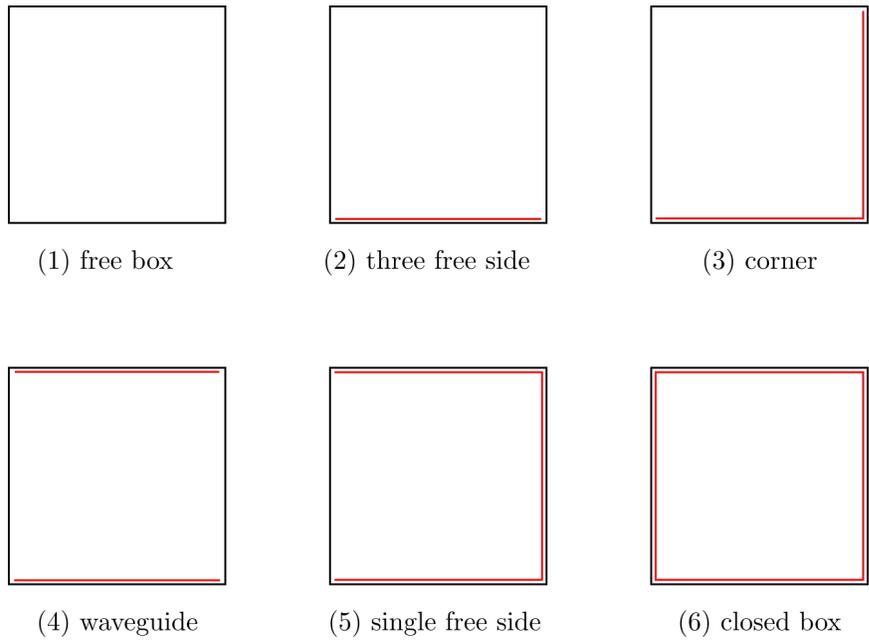


**Figure 65:** Six cases with different reflection boundary conditions. Boundaries in red represent the reflective boundaries.

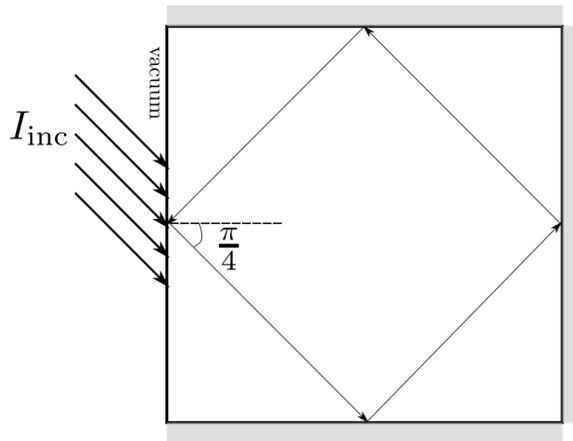


**Figure 66:** Schematic for the problem with a prescribed incident on the left wall. The other three walls are either specularly reflective or vacuum depending on the case described in Fig. 65.

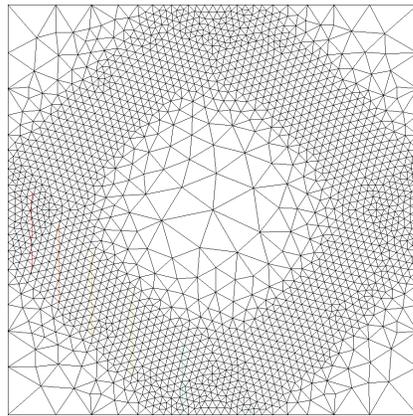


**Figure 67:** Spatial mesh for the specular reflection problem.

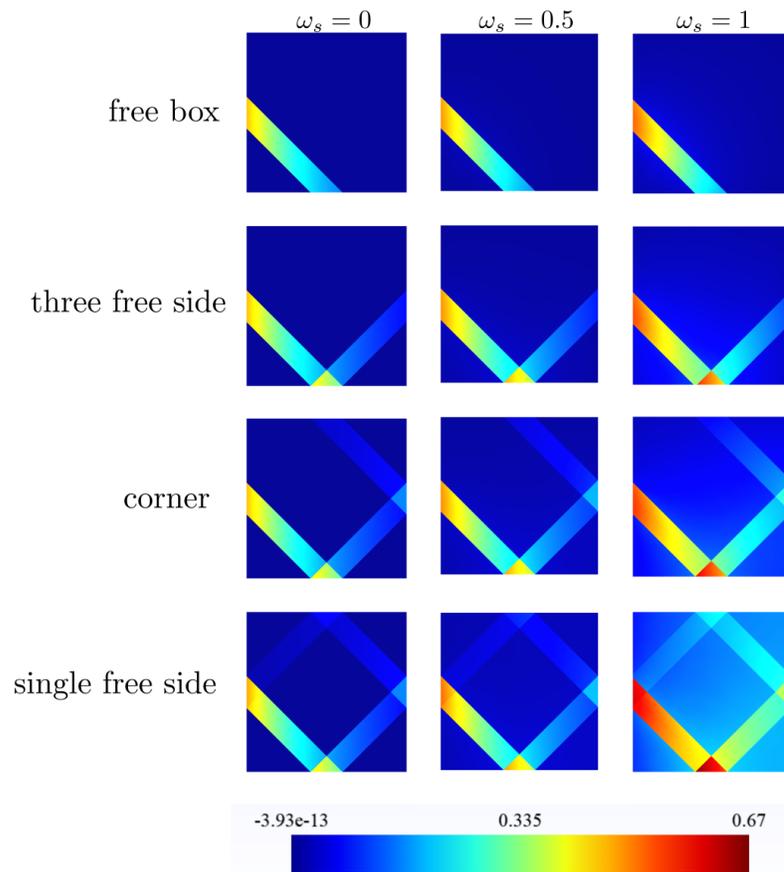


**Figure 68:** Contour plots of radiative density  $D$  for the specular reflection problem with incidence on the left boundary for the cases (1), (2), (3), and (5) listed in Fig. 65 in rows. The columns from left to right correspond to albedo  $\omega_s = 0$  (zero scattering), and  $\omega_s = 0, 5, 1$ , respectively.

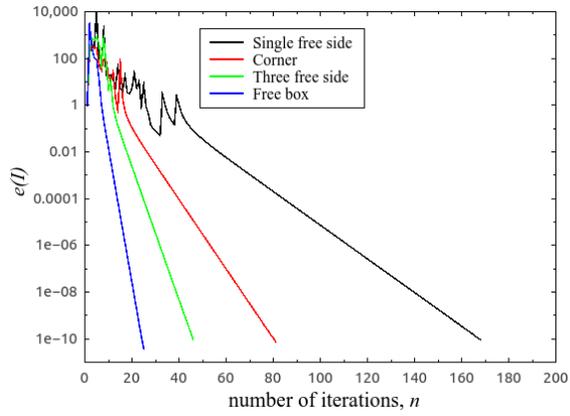


**Figure 69:** Evolution of errors with respect to iterations for  $\omega_s = 1$ .

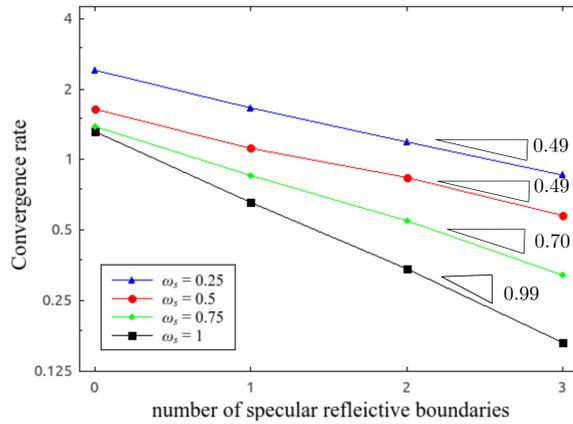


**Figure 70:** Convergence rate with respect to number of specularly reflective boundaries when  $\omega_s = 0, 0.25, 0.5,$  and  $1$ .

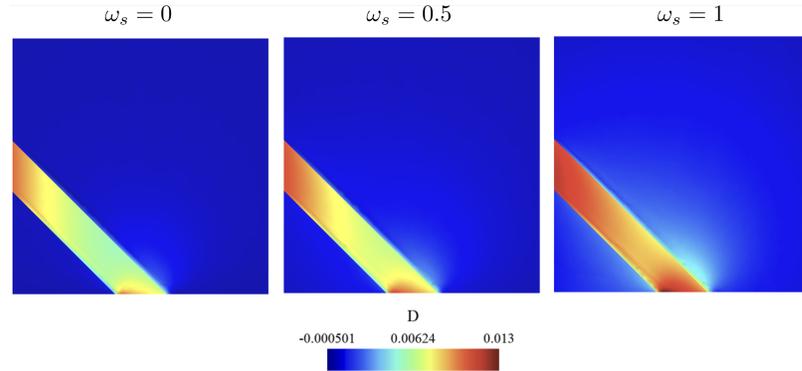


**Figure 71:** Contour plots of radiative density  $D$  for the uniformly diffuse reflection problem with incidence on the left boundary, the diffusely reflective boundary at the bottom, and vacuum boundaries on the right and top (case (2) in Fig. 65).

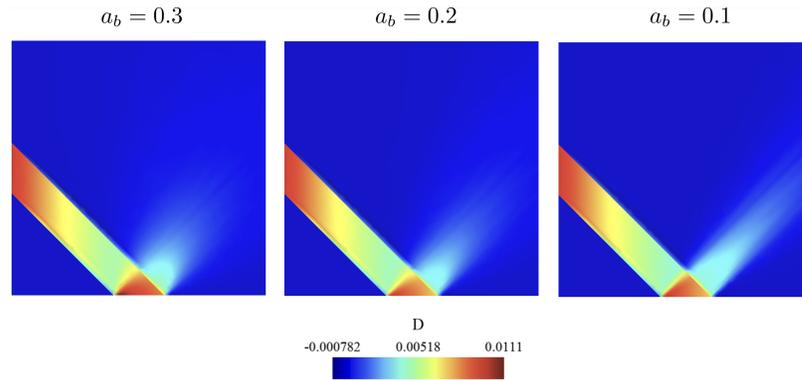


**Figure 72:** Contour plots of radiative density  $D$  for the directional diffuse reflection problem with incidence BC on the left, diffuse reflective BC on the bottom, and vacuum on the right and top boundaries (case (2) in Fig. 65). The solutions correspond to different values of  $a_b$ .

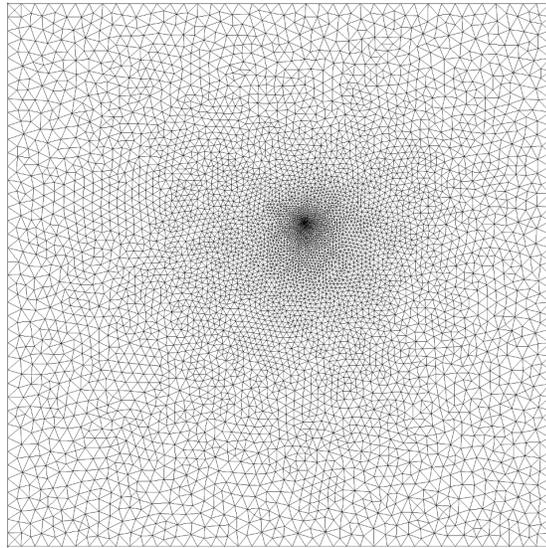


**Figure 73:** Spatial mesh for the point source problem.

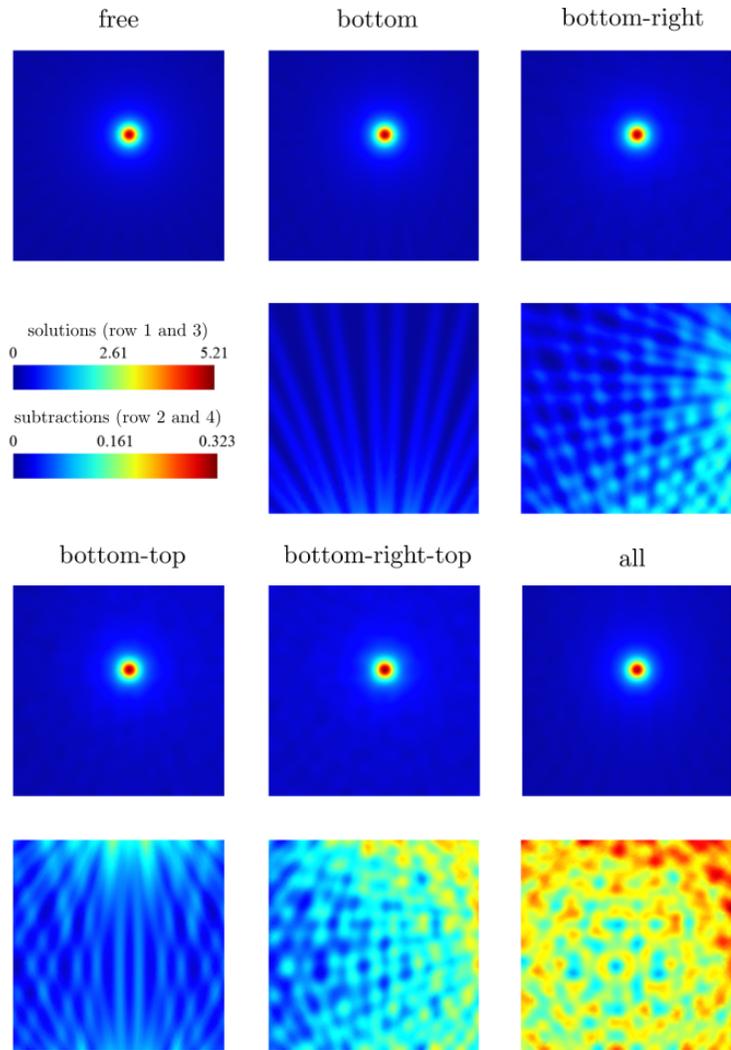


**Figure 74:** Contour plots of radiative density  $D$  for the point source problem in the first and third rows. The second and fourth rows are the subtractions of the solutions from the free box solution. The top colorbar at the second row and first column is for the solutions; and the bottom colorbar is for the subtractions.

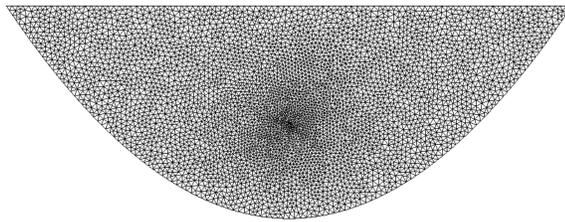


**Figure 75:** Spatial mesh for the parabolic reflector problem.

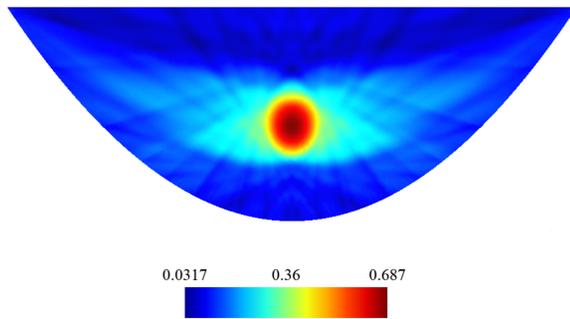


**Figure 76:** Contour plots of Radiative density  $D$  for the parabolic reflector problem.

# Vita

Hang Wang was born in Daqing, Heilongjiang Province, China on November 22, 1990. Hang grew up in Shanghai, China, and graduated from Weiyu High School in May 2010. In September 2010, he entered Shanghai University in Shanghai and subsequently received the degree of Bachelor of Science in Mechanical Engineering in June 2014. He continued his studies at Shanghai Institute of Applied Mathematics and Mechanics, Shanghai University. Hang received a Master of Science degree in Mechanical Engineering in July 2017. He has begun his studies at the University of Tennessee Knoxville/Space Institute pursuing a Ph.D. in Mechanical Engineering with a research concentration in Applied Mechanics and Computational Mechanics under the pupilage of Dr. Reza Abedi, since August 2017.